MODELING AND SIMULATION OF THE PORE-SCALE

MULTIPHASE FLUID TRANSPORT IN SHALE

RESERVOIRS: A MOLECULAR DYNAMICS

SIMULATION APPROACH

by

Gorakh Pawar

A dissertation submitted to the faculty of
The University of Utah
in partial fulfillment of the requirements for the degree of

Doctor of Philosophy

Department of Mining Engineering

The University of Utah

May 2016

The University of Utah Graduate School

STATEMENT OF DISSERTATION APPROVAL

The dissertation of **Gorakh Pawar**

has been approved by the following supervisory committee members:

Ilija Miskovic	, Chair	**12/16/2015**
		Date Approved
Michael G. Nelson	, Member	**12/16/2015**
		Date Approved
Felipe Calizaya	, Member	**12/16/2015**
		Date Approved
John David McLennan	, Member	**12/16/2015**
		Date Approved
Jack Pashin	, Member	**12/16/2015**
		Date Approved

and by **Michael G. Nelson** , Chair/Dean of

the Department/College/School of **Mining Engineering**

and by David B. Kieda, Dean of The Graduate School.

ABSTRACT

Shale resources provide a tremendous opportunity for a long-term viable energy source, but the lower hydrocarbon recovery rates are hindering the economic development of shale reservoirs. One of the main reasons for the lower hydrocarbon recovery rates is the inadequate understanding of the fate of various injected fluids and the recovered hydrocarbons during various stages of exploration and production.

As Darcy's law is limited in describing the multiphase fluid transport in shale, a comprehensive simulation framework is necessary, enabling the replication of the nanometer and subnanometer pores found in organic and inorganic matrices, and the simulation of the multiphase fluid flow in these nanopores, thus improving the comprehension of the pore-scale fluid transport process in shale reservoirs.

A molecular dynamics simulation-based framework is developed in present research to address the above-defined challenges. The applications of various open-source molecular modeling tools are integrated to develop molecular pore structures found in the organic and inorganic matrices. An application of the general-purpose DREIDING force field is extended to simulate the kerogen. A gas-liquid (methane and water) transport is simulated in nanopores confined in the organic and inorganic matrices, and various dynamic transport properties of fluids (subjected to confinement) are determined to gain the qualitative and the quantitative understanding of the fluid flow.

The present research provides a powerful molecular dynamics simulation-based

framework that will enable the development of more complex models of nanoporous shale structures and address numerous challenges encountered in hydrocarbon recovery from shale reservoirs.

TABLE OF CONTENTS

vi

LIST OF TABLES

ACKNOWLEDGEMENTS

First, I would thank my advisor Dr. Ilija Miskovic and the Department of Mining Engineering, University of Utah, for providing me with the William Browning Fellowship and the opportunity to pursue my graduate studies. Further, I would like to thank Dr. Ilija Miskovic for mentoring me in the various academic and nonacademic aspects that were crucial to develop the skills and the expertise required for the successful completion of the present research. I also would like to thank my committee members Dr. Michael Nelson, Dr. Felipe Calizaya, Dr. John McLennan, and Dr. Jack Pashin for their assistance during various stages of my dissertation.

I also wish to thank Dr. Hai Huang and Dr. Earl Mattson from the Idaho National Laboratory (INL) for providing me an internship opportunity and the access to the INL's supercomputer facility, which was the driving force for the successful completion of all simulations studies of the present research. Also, I would like to thank Dr. Paul Meakin from Temple University for some insightful discussions that helped me to sharpen my skills and the critical thinking.

I also wish to thank Pam Hofmann from the Department of Mining Engineering for all administrative work. I also appreciate the love and the patience of my parents and my sisters who stood behind me throughout my graduate studies. Last but not least, I would to thank P. P. Bapu for providing me with the courage and strength required to overcome the challenges, and successfully finishing another chapter of my life.

CHAPTER 1

INTRODUCTION

Shale gas comprises a significant fraction of the total gas production in North America and other parts of the world including the South America, Australia, Africa, and Asia. It is estimated that 16,000 trillion cubic feet (TCF) of shale gas are in place globally (Holditch et al. 2007), which represents a long-term global energy resource. Figures 1.1 and 1.2 show the expected natural gas production from different sources and reservoir formations in the United States.

The successful exploitation of shale resources relies on the numerous techniques, including hydraulic fracturing ands multistage completions. Still, the expected ultimate recovery rates from shale gas reservoirs, which increased from 2 % to 50 %, are believed to be in the range of 15 to 35 % (King 2010), and this is, in large part, due to the limited understanding of the fate of injected fluids and recovered hydrocarbons during different stages of exploration and production.

Reservoir modeling and simulation techniques based on continuum physics (e.g., Darcy's law) have played a significant role in developing a better understanding of the processes that occur during conventional oil and gas recovery. However, an alternative strategy is required to model and simulate the hydrocarbon recovery process in unconventional reservoirs due to the following challenges:

- the complicated pore network that defines the shale fabric

- the pores with a dimension of 50-nm or less where the mean free path of the molecules becomes comparable with the pore size

- the heterogeneous distribution of the kerogen and inorganic matter (e.g., quartz and calcite) throughout the reservoir matrix

- the strong fluid-pore surface interaction at the molecular level, which results in the variety of sorption phenomena and affects the hydrocarbon recovery

A molecular dynamics (MD) simulation-based approach is presented in this thesis to model and simulate the atomistic pore-scale multiphase fluid transport in a realistic unconventional reservoir matrix. To achieve this goal, the present dissertation is organized into chapters and are summarized as follows:

Chapter 1 provides the overview of the dissertation and contains the summary for each chapter. Chapter 2 presents a literature review, which describes the fundamental aspects of unconventional reservoirs, identifies the significant challenges in hydrocarbon production from unconventional reservoirs, and provides the background of the MD simulation method. Further, the applications of the MD simulations are also summarized. In addition, the Coarse-Grained Molecular Dynamics (CGMD) technique is introduced to extend MD simulation capabilities for the longer time and length scales, which are suitable for characterization of the slow-evolving recovery process observed in unconventional reservoirs. Chapter 3 outlines the problem statement of the present research.

Chapter 4 describes the MD simulation-based workflow to develop realistic organic and inorganic pore models and to simulate an atomistic, multiphase fluid transport in these pores. An example of a cocurrent imbibition mechanism in the 5-nm inorganic pore, consisting of an amorphous quartz, is shown to demonstrate the application of the proposed

workflow. Moreover, the important fluid properties including the diffusion coefficient and water and methane distribution inside the nanopore are evaluated.

Chapter 5 includes the parametrization of the general-purpose DREIDING force field to model and simulate a representative kerogen structure, having variable thermal maturities — Type I (immature kerogen), Type II (middle-end oil window kerogen), and Type III (matured kerogen) — and elemental composition. A kerogen density and the carbon-carbon pairwise distribution function are evaluated for each kerogen type and compared with the experimental and simulation results available in the literature. Further, the atomic structure of kerogen is analyzed to characterize the subnanometer scale features (subnanometer size pores) within kerogen matrix — which is difficult with conventional transmission electron microscopy (TEM)/scanning electron microscopy (SEM) techniques.

Chapter 6 includes simulation of pore-scale multiphase flow (water displacing methane) for open and closed pore configurations in Type II kerogen for various reservoir attributes, including the pore diameter, the force applied to water molecules, and the reservoir temperature. The diffusion coefficients of water and methane are compared to analyze various aspects of the methane recovery process in a Type II kerogen.

Further, molecular simulations were optimized to run them on graphics processing units (GPUs) to extend the capability of MD simulation to a longer timescale. Also, the coarse-grained molecular dynamics models for water confined in a quartz nanopore were developed to upscale the molecular models of these systems. Finally, Chapter 7 summarizes the conclusions of the present dissertation, the research contribution and the utility of present study in future research.
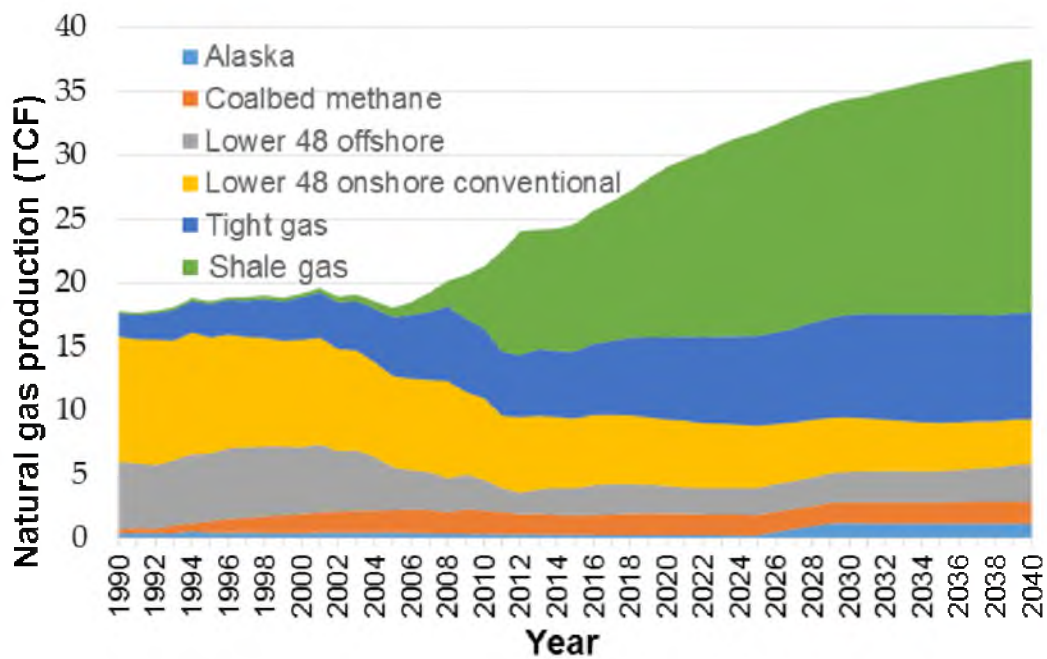
**FIGURE 1.1 Natural gas production in the United States by source
(Source: U.S. Energy Information Administration 2015)**
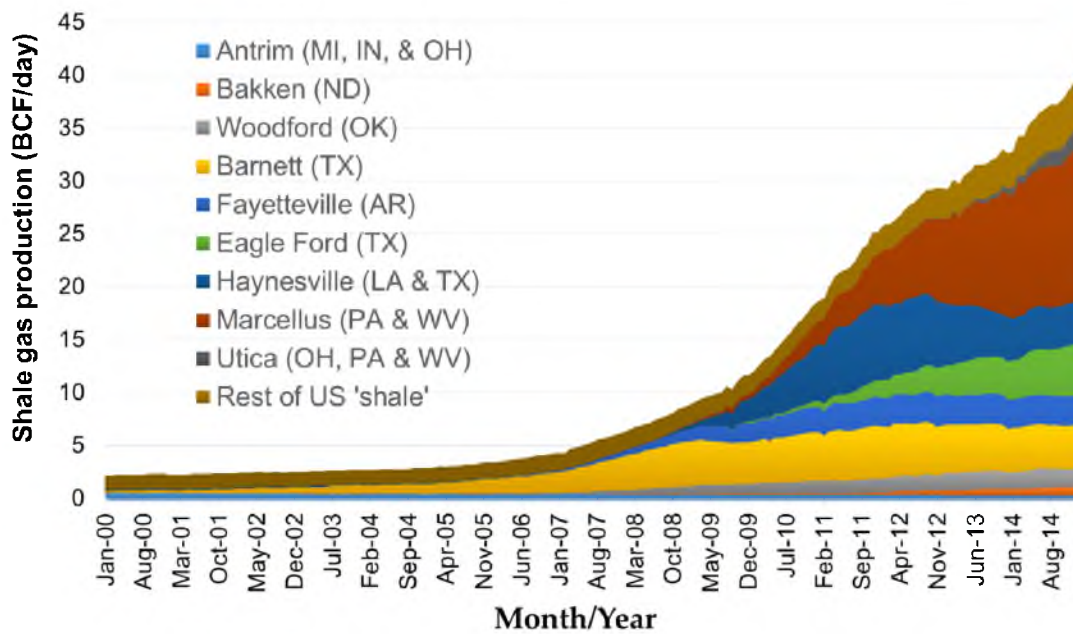
FIGURE 1.2 Natural gas production in the United States by reservoir formation (Source: U.S. Energy Information Administration 2015)

CHAPTER 2

LITERATURE REVIEW

Unconventional reservoirs (shale gas, tight gas, and coal-bed methane) are the types of resources that require additional recovery techniques besides those methods used in conventional reservoirs. The technological advances in horizontal drilling and multistage hydraulic fracturing have changed the landscape of shale gas production in the United States, and shale gas has emerged as one of the crucial and strategic energy sources to offset the declining hydrocarbon production from conventional oil and gas reservoirs. Figure 2.1 depicts the active and prospective shale resources in the United States along with the structure of these shale plays.

A significant effort has been spent to understand shale structures, the shale composition, and the multiphase fluid transport in shales — which is summarized in Table 2.1. These studies were significant in increasing the understanding of various macroscopic and the microscopic aspects of shales, but provided very limited information on nanoscale fluid transport processes in realistic shale nanopores, which is, indeed, the primary mode of fluid transport in shales and the key to understanding various transport processes — adsorption, absorption, and diffusion — in the shale matrix. The main reason for the limited understanding of the fluid transport in shales is the typical shale reservoir structure, which fundamentally differs from the conventional reservoir in many aspects. These differences are summarized in section 2.1.

2.1 Fundamental differences between conventional and unconventional reservoirs

First, the porosity and the permeability of shale reservoirs is significantly lower than in conventional reservoirs. This is in large part due to the nanoporous structure of shales, which consist of poorly connected pore networks. In addition, the hydrocarbons and other reservoir fluids are subjected to confinement effects coupled with the significantly higher surface forces and the thermo-geo-chemical effects of the reservoir matrix. As a result, most of the hydrocarbons remain trapped in shale nanopores and the hydrocarbon migration between disconnected pore networks, which constitutes a significant fraction of shale reservoir, is almost impossible and depends mainly on the size of the migrating hydrocarbon molecules. Small molecules such as methane may diffuse through the reservoir matrix, provided that the conduits of sizes equal or greater than the methane molecules exist within the reservoir matrix. On the other hand, the migration of hydrocarbons containing long molecular chains is extremely difficult in the confined spaces such as nanometer and subnanometer scale pores, due to the size and the structure of hydrocarbon chains. Also, the reservoir structure, which consists of an atomically bonded structure on a molecular scale, may act like a sieve that restricts the migration of long hydrocarbon chains.

Secondly, the shale reservoirs function as a source rock, a reservoir, and trap (Ma and Holditch 2015). Unlike the conventional reservoirs, where hydrocarbons from the source rock (rocks responsible for the hydrocarbon production) migrate through high permeability pathways and accumulate near the impermeable structure (thus forming reservoir) — the hydrocarbons from unconventional source rocks (which is kerogen) do not migrate and accumulate in large quantities, they usually remain trapped in the

nanopores. As a result, a reservoir stimulation method such as hydraulic fracturing that can open existing or new fractures (break the bond between atoms on the molecular scale to create the pathways for the hydrocarbon transport and their accumulation), improve the pore connectivity and release the trapped hydrocarbons is required.

Third, shale reservoir structures are extremely heterogeneous and consist of organic (e.g., kerogen) and inorganic (e.g., quartz, calcite, and clay minerals) matrices, which are dispersed throughout the reservoir matrix. The individual organic/inorganic grain size can vary from few nanometers to micrometers (Bernard et al. 2010). Further, the size of the grain changes significantly for grains separated even by a very small distance (e.g., the separation distance of μm or less), thus resulting in a multiscale mineralogical heterogeneity in shales. Moreover, the fundamental properties of organic and inorganic phases such as structure and elemental composition also vary due to different origins of these phases and the transformation of the phases over the geological time scale. As a consequence, the shale reservoir composition varies from the reservoir to reservoir and is shown in Figure 2.2. Figure 2.2 is also called a ternary diagram that differentiates the shale reservoirs based on their mineralogical composition. Typically, clay minerals, quartz, and calcite are shown on the ternary diagram.

Fourth, the continuum theory, which can be used to simulate the multiphase fluid transport in conventional reservoirs, is not applicable to shale reservoirs, mainly due to the length scales (nanoscale) of the simulation (Falk et al. 2015). Thus, modeling and simulation in shales require an inclusive approach that can accommodate various factors that affect the behavior of reservoir fluids and the reservoir fluid transport in shale nanopores. The important factors are summarized in Figure 2.3 and described in the

following paragraphs.

2.2 The factors affecting the pore-scale multiphase fluid flow modeling in shale reservoirs

First, the underlying pore structure, the pore size distribution, and the pore connectivity are the important factors in the pore-scale modeling of shale reservoirs, as they determine the reservoir quality (i.e., effective porosity and permeability of shales) and affect the fluid flow. Various studies (Kuila and Prasad 2013; Loucks et al. 2009; Nelson 2009) showed that the typical pore size distribution in shales ranges from a few angstroms to micrometers. First, the pore size distribution identifies the most dominant pores (mode of the pores in statistical terms) that are potentially responsible for the storage of a large number of hydrocarbon molecules. Second, the pore size distribution provides an estimate of the fluid flow regime (explained later in the chapter) that exists in the pore system based on pore sizes, and the identification of the pore sizes that are potentially responsible for the hydrocarbon transport, and which can be used for the pore-scale modeling and simulation.

A total number of pores obtained with the pore size distribution can be segregated into two parts: pores that exist in the organic phase, and pores that exist in the inorganic phase. Further, the pores, both in organic and inorganic phases, can be classified into interparticle pores (pores that exist on the boundary of two mineral phases or the boundary of a mineral and organic matter phase) and the intraparticle pores (pores exist exclusively in the mineral phase or the organic phase) (Loucks et al. 2012), and are shown in Figure 2.4. The interparticle pores are generally of a larger size, rare, and hard to detect, whereas intraparticle pores can be identified if they fall within the detection limits of the focused ion beam (FIB)/scanning electron microscopy (SEM).

The pores in the organic phase are of the utmost importance as they store a significant amount of hydrocarbons produced during the thermal maturation of organic matter, and act as a source of hydrocarbon in shales. Further, there may exist subnanometer size pores, which are outside of the detection limit of the focused ion beam (FIB)/scanning electron microscopy (SEM), and their characterization requires an experimental approach such as low-pressure adsorption or high-pressure mercury intrusion (Clarkson et al. 2013).

The second important factor in the pore-scale modeling is the variability of the fluid flow regime, which is mainly dependent on the pore size. As the pore size decreases, the mean free path of fluid molecules becomes comparable or even greater than the characteristic length of the pore (pore diameter is taken as the characteristic dimension in most of the cases) and results in various fluid flow regimes (Civan 2010). The Knudsen number (Kn), which is given by Equation 2.1, is defined as the ratio of the mean free path (λ) of the fluid molecules and the characteristic dimension of the pore and is used to determine the fluid flow regime. Further, the pore sizes and shapes are irregular due to the fusion of different pores into a single pore during the pore formation process, thus potentially resulting in the simultaneous existence of multiple fluid flow regimes, such as molecular flow, slip flow, and continuum flow. Table 2.2 summarizes various fluid flow regimes based on the range of Knudsen number.

$$Kn = \frac{\lambda}{d} \hspace{8cm} (2.1)$$

The third important factor in the pore-scale modeling is the pore composition. As described earlier, the shale consists of a mixture of organic and inorganic phases (e.g.,

laminated siliceous mudstone, laminated argillaceous lime mudstone, etc.). Thus, the accurate modeling and simulation of the pore-scale transport phenomena in shales requires a precise description of the phases that hosts the pore structure — as the structural properties of various phases along with the material properties (on atomic scale) such as van der Waals forces of atoms and the electrostatic interactions between charged atoms affect the underlying fluid transport.

The fourth important factor in the pore-scale modeling is the confinement effects. The fluid properties subjected to confinement vary significantly from the bulk properties of the fluid (Firincioglu et al. 2012). The main reason for the difference is the restricted movement of the fluid molecules within the confined space, which results in the deviation of confined reservoir fluid properties from bulk fluid properties. A few examples have been shown in Table 2.1 that show the difference between bulk and confined reservoir fluid properties.

The fifth important factor in pore-scale modeling is the pore anisotropy. The pore anisotropy refers the pore structure where pore surface exhibits the irregular shape and size and composed of various types of atoms/chemical functional groups. In the scientific literature, perfectly cylindrical pores have been extensively used to model pores (Chen et al. 2008; Sokhan et al. 2002). However, realistic pore structure deviate from the ideal (cylindrical) structure and consists of a variable sizes and shapes. The main reason for this deviation can be explained as follows. The atomic structure of shales nanopores undergoes geo-thermo-transformation over the geological scale and results in a pore structure where atoms are not perfectly arranged (pores do not result in a perfectly cylindrical shapes), thus resulting in irregular pores. Figure 2.5 shows the difference between the ideal pore, which

is of a cylindrical shape and consists of pure carbon that are mostly used to simulate the pore scale flow; and the representative (realistic) pore, which is not perfectly cylindrical, as imagined, and that consists of various atoms/functional groups. Thus, the structural differences between ideal and real pore will result in differences in the fluid transport properties.

Finally, the sixth important factor in the pore-scale modeling is the reservoir temperature. At the pore level it is challenging to integrate all reservoir attributes in the modeling and simulation — e.g., the impact of the effective geomechanical stresses can be incorporated in the pore model, but the stresses generated as a result of thermal fluctuation (at an atomic scale), sometimes are high (depending on the size of the pore) and become comparable with the effective geomechanical stresses, thus making it difficult to differentiate the contribution of each stress component on the behavior of the underlying system.

The experimental-based techniques can provide some insight into the fluid flow in shale reservoirs, but the challenge with the experimental studies is that they lacked the ability to show the *in-situ* pore-scale fluid flow transport details maintaining the prevalent pore-scale conditions, e.g., the confinement effect. The limitations in the experimental pore-scale characterization, in large part, are due to the following factors.

2.2.1 Physical isolation of organic/inorganic nanopores and the pore networks

A physical separation of mineral and organic phases in shales, particularly kerogen, from the source rock is a complex process, thus the isolation of the pore network found in these phases is an even more complex task. Also, during the physical separation of minerals and organics from source rock, the organic and inorganic phases may undergo a structural

transformation, thus resulting in a structure that may not necessarily resemble the original structure.

2.2.2 Limitations in the visualization of the *in-situ* pore-scale transport process

The visualization of the in-situ transport processes in shale nanopores is extremely difficult while simultaneously maintaining the pore-scale thermodynamic conditions and the confinement effects. A few visualization techniques, such as radiotracers and chemical tracers can provide some insight into the processes, but they cannot reveal the fine details of fluid flow in the nanopores (e.g., adsorption and diffusion processes which are the main characteristics of the fluid transport in shale reservoirs).

2.2.3 Requirement of sophisticated instrumentation and the skilled personnel to perform the experimental studies

A sophisticated instrumentation is required that can capture the multiphase pore-scale fluid flow details on the atomic scale. The main challenge with such instrumentation setup is the resolution of the length scale. Further, skilled personnel is required who have had prior experience building and operating such complex systems.

2.2.4 The time needed to set up the experimental studies

Even if it is possible to build the experimental setup for the pore-scale flow analysis, a significant amount of time is required to design, develop, and integrate individual components and ensure the accurate functioning of experimental setups for the intended use.

2.2.5 The reliability of experimental studies

At the molecular scale, the fluctuation of properties, (e.g., the atomic displacements) is very high, and it is difficult to isolate the noise in data collection. Thus, the accuracy of the collected data may be questionable.

The limitations of the pore-scale experimental studies can be mitigated to some extent by the various reservoir modeling and simulation techniques, such as numerical reservoir modeling, the lattice Boltzmann method, and the discrete element method. However, the main challenge with these techniques is the simultaneous integration of all of the pore-scale factors (e.g., the pore composition, the pore anisotropy) in modeling.

Considering the challenges in pore-scale fluid flow modeling, the molecular dynamics (MD) simulation appears to be a better alternative, since the MD simulations have shown the capability to model such complex processes in the fields of biological science, material sciences, and provide a detailed understanding of the underlying transport processes (summarized in Table 2.3). The next section provides a brief discussion of the MD simulation method, the capabilities of MD simulations, some important applications of MD simulations, and the limitations of MD simulations. The detailed description of the MD workflow that will demonstrate the modeling and simulation of the pore-scale multiphase fluid transport phenomena in shales is provided in Chapter 4.

2.3 Molecular dynamics simulation method

The MD simulation solves the equations of motion to evaluate the temporal position of atoms, velocities of atoms, and the intermolecular forces between atoms. This information is used to determine the key fluid transport properties. The important attributes of MD simulations are listed below, which extends the capability of the MD simulation

method to model the multiphase transport phenomena in shale nanopores. MD simulations have the ability to:

- provide the most detailed representation of the complex multiphase fluid transport in nanopores

- provide access to the length scale (nanometers) and time scale (femtosecond), which are physically impossible

- model various transport processes simultaneously e.g., diffusion and adsorption of molecules in shale nanopores

- model various inorganic and organic phases explicitly with found pores/pore networks, irrespective of the origin and the geological transformation of organic and inorganic phases

Hence, considering the potential of the MD simulations, they have been widely used in many fields. Only the selected studies are summarized in Table 2.3. From Table 2.3, it can be seen that MD simulations are mostly used to model a single phase fluid transport in a nanotube (nanopores) which consists of carbon, but these studies provide the information necessary to model and optimize the simulation parameters of the multiphase fluid flow in shale nanopores.

The following paragraph summarizes a few important aspects/definitions, which are important to comprehend the MD simulation workflow presented in Chapter 4. Additional MD aspects/definitions will be explained wherever necessary.

2.3.1 Fundamental aspects of MD simulations

2.3.1.1 The simulation domain

This is the box size that encloses the system being simulated. The system domain may be open or closed. In a open domain, the atoms are allowed to leave/reenter the simulation box, whereas the closed simulation box does not allow atoms to leave or enter into the system.

2.3.1.2 The boundary conditions

There are various types of boundary conditions that can be used in MD simulations to describe the fluid transport in nanopores. Primarily, two boundary conditions, periodic boundary condition, and fixed boundary condition are widely used. The periodic boundary condition assumes the three-dimensional (3D) replica of the system as shown in Figure 2.6 (showing a two-dimensional (2D) slice of the 3D replica), where atoms leave the system from one side and enter from another side.

In addition, the atoms near the simulation domain edge interact with the atoms in the 3D replica that falls within the specified cut-off distance in the interatomic potential calculations. Contrarily, in the *fixed boundary conditions*, the atoms do not escape and reenter through the boundaries; they accumulate near the wall of the simulation box and affect the overall simulation results.

2.3.1.3 Ensemble

In MD simulations, different types of ensembles can be used. The ensemble is the representative state of the system where all simulations are carried out. There are different types of ensembles depending on the properties of the system held constant and explained

as follows.

In NPT ensemble, the number of molecules (N), the system pressure (P), and the system temperature (T) are constant (shown in Figure 2.7). Energy can flow in and out in this ensemble. The volume and resulting density of the system can change.

In NVT ensemble, the total number of molecules (N), the system volume (V), and the system temperature (T) remain constant (shown in Figure 2.8). In addition, the energy can flow in and out of the system. Since the volume and the number of molecules (thus, total mass of the system) are constant, the density does not change. Usually, either NVT or NPT ensembles can be used if experimental verification is sought.

In NVE ensemble, the total number of atoms (N), the total system volume (V), and the energy of the system (E) remain constant. Energy cannot flow in and out in this ensemble. This type of ensemble is not practically feasible as it is difficult to maintain a constant energy state of a system.

2.4 Limitations of MD simulations

One of the major limitations of the MD simulations is the requirement for significant computational resources, depending on the number of atoms/molecules being simulated. Also, the parameters used for MD simulation (e.g., the timestep used, and the cut-off distance to calculate the electrostatic interaction between two charged atoms) affects the total computational time and requires optimization. However, due to the advent of modern, massively-parallel computational techniques, the computational power can be leveraged to enhance the capability of the MD simulations for the longer simulation times. Further, the capability of MD simulations can be upscaled for the larger length scales that can enable the simulation of larger systems (pore networks) with the coarse-grained

molecular dynamics (CGMD) technique. The following section provides a brief discussion on the massively-parallel computing and the CMGD technique that will permit upscaling the MD models and simulate them for a longer period.

2.5 Enhancing the capabilities of MD simulations for longer time and length scales

With the traditional serial computing, where only one set of instructions is executed at a time, performing computationally demanding simulations is a cumbersome task. Thus, the CPU-based and the GPU-based high-performance computing (HPC) has become an indispensable tool and integral part for applications that requires a multidisciplinary approach. Hence, the HPC offers cost-effective tools that allow the simulation of the computationally demanding MD simulation of the pore-scale multiphase fluid transport in shale reservoirs. Before summarizing the applications of HPC in MD simulations and possible speedups that can be achieved, the key concepts are summarized in the following paragraph.

First, it is necessary to identify various computational tasks (e.g., the electrostatic interactions calculation between charged atoms, the building of neighbor list, the evaluation and storage of atomic positions, velocities and forces) that require parallelization. This helps to allocate the available computational resources to maximize the computational performance by optimizing various aspects of parallelization such as the interprocessor communication and the simultaneous access of the memory by the multiple processors.

Two different mechanisms can be used for the parallelization including the data parallelism and the functional parallelism. In data parallelism, multiple processors work on

various parts of the same data. On the other hand, larger numerical problems are broken into subtasks and executed on various processors in functional parallelism, where different processors work together by data exchange and synchronization. The functional parallelism requires optimization as the various subtasks may have different computational times and hardware requirements, and may result in wastage of computational resources if not properly parallelized.

Further, the computational processors can be classified as single instruction single data (SISD), single instruction multiple data (SIMD), multiple instructions single data (MISD), and multiple instructions multiple data (MIMD) based on the how processors handle the data and instructions during the computational task. The most of the modern parallel computers falls in the MIMD category, where every processor executes different instruction streams on its own data stream (Wolf 2010).

The typical example of the MIMD is the modern parallel computer architecture (as shown in Figure 2.9) that uses the shared-memory and distributed-memory. In parallel computer architecture, a network is required to enable the data transfer between shared memory processors. Further, the total computational job is broken into subparts and executed on the available processors.

Typically, the parallel computer architecture uses symmetric multiprocessors made of identical processing elements and uniform memory, which help to simplify the computational task executed on different processors (Wolf 2010). In addition, the shared memory computers used in the parallel computer architecture are the systems where a number of processors work on a common physical address space whereas the distributed memory computers are the systems where each processor has its own local memory. The

architectures of shared and distributed memory systems are shown in Figures 2.10 and 2.11. For the shared-memory architecture, an additional mechanism is required to ensure the content of the given location and this is what the user intends. Another challenge with the shared memory is the difficulty in understanding how the memory access patterns (by different processors) affect the computational performance.

2.5.1 Porting in parallel computing applications

Porting refers to the conversion of the existing application code to the parallel architecture. Based on the efforts and modifications required in the existing code, the porting can be categorized into different strategies is shown in Figure 2.12 (Morse 2014). The first strategy consists of automatic parallelization, which requires minimum efforts and existing code and it can be ported with minimum modifications. On the other hand, the major recoding strategy requires significant changes and development code from scratch.

After optimization of parallelization parameters, the MD simulations can be performed efficiently, minimizing the total computational time of simulations. The performance of parallel computing is highly dependent on the architecture. Table 2.4 summarizes selected GPU architecture and their applications in the MD and CGMD simulations that emphasize the possible speed-up.

The coarse-grained molecular dynamics (CGMD) is a powerful mesoscale simulation tool that enables access to the longer length and time scales that are beyond the reach of traditional all-atom MD simulations. The coarse-grained molecular dynamics, as the name suggests in which the group of atoms is represented by a bead (particle), is extensively used in slow-process-evolving applications, such as protein folding mechanisms, where the typical protein folding time is on the order of μs or more and the

use of the all-atom MD simulations in such scenarios is not practically feasible. Table 2.5 summarizes the applications of the CGMD simulation technique.

While defining the CGMD model from the atomistic model (also called as all-atom model where molecules are used for the simulation instead of beads), two distinct steps are used and are represented in Figure 2.13. First, the mapping of atoms is done (as shown in Figure 2.14) that combines a certain number of atoms to form a bead. As there is no standard procedure for defining the level of coarse-graining, it solely depends on the application.

The next step in the coarse-graining model is an accurate definition of the interaction potential between CG beads, as it has profound effects on the accuracy of the CGMD simulations. Once the atomic mapping and the interatomic potential parameters between beads are determined, these parameters require further calibration. All-atom molecular dynamics simulations of an equivalent system can be performed to evaluate the static (e.g., atomic pairwise distribution function) and the dynamic (e.g., the mean square displacement) properties, which can be compared with the CGMD results. This process continues until the reasonable agreement between all-atom simulation results, and CGMD simulation results are found. Once the calibration process is complete, the atomic mapping information and the interatomic potential parameters are used to define the larger and more complex system.

In summary, the present chapter provides the overview of the shale reservoirs, the challenges in shale gas reservoir recovery, the limitations of experimental methods, and various simulation methods simulating the multiphase fluid transport in shale reservoirs. Further, various factors affecting the pore-scale fluid modeling are discussed. In addition,

the fundamentals of the MD simulation, the capability of MD simulations, the applications, and the limitations of the MD simulations are also provided. Finally, the high-performance computing and the coarse-grained molecular dynamics methods are introduced to extend the capability of the MD simulations for the longer length and time scales.
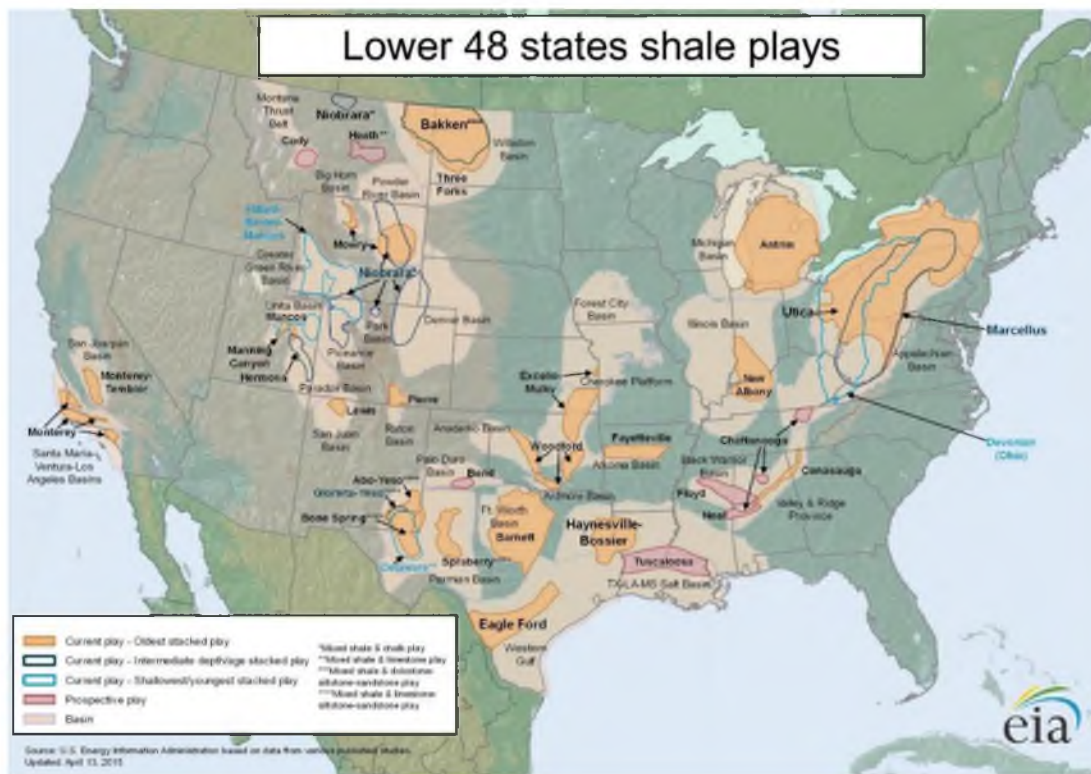
FIGURE 2.1 Shale gas plays in the United States (Source: U.S. Energy Information Administration 2015)
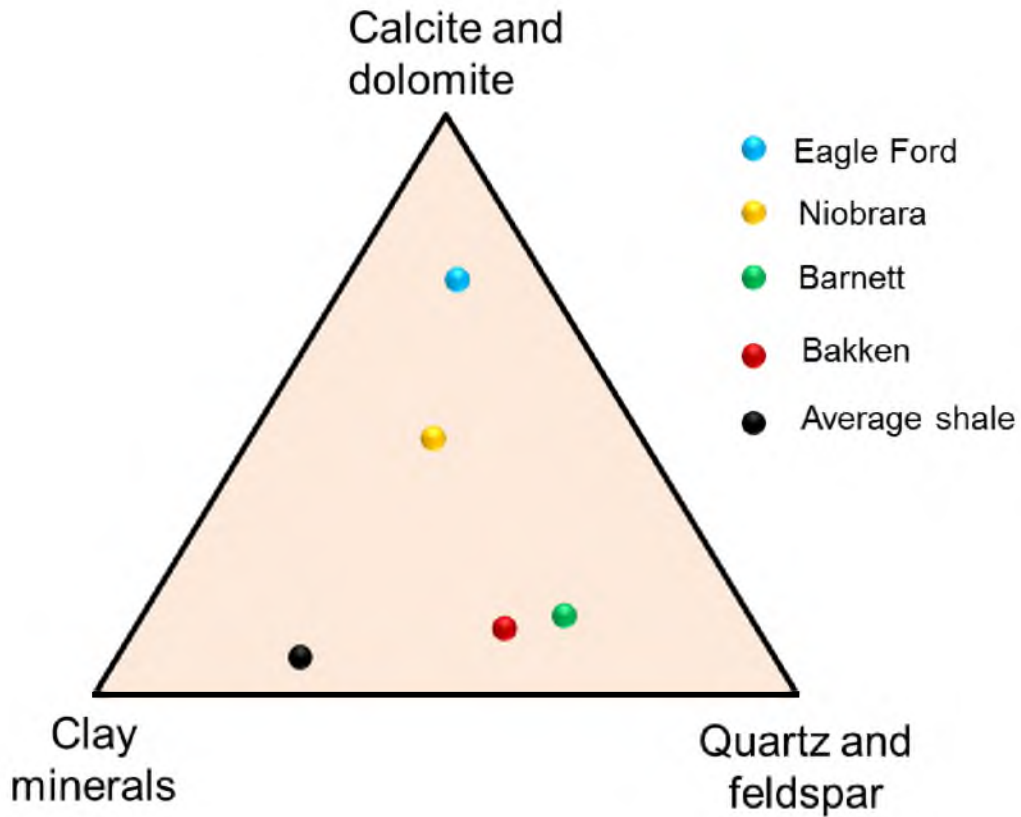
FIGURE 2.2 Ternary diagram showing shale composition (Adapted from Ma and Holditch 2015 with permission from Elsevier)
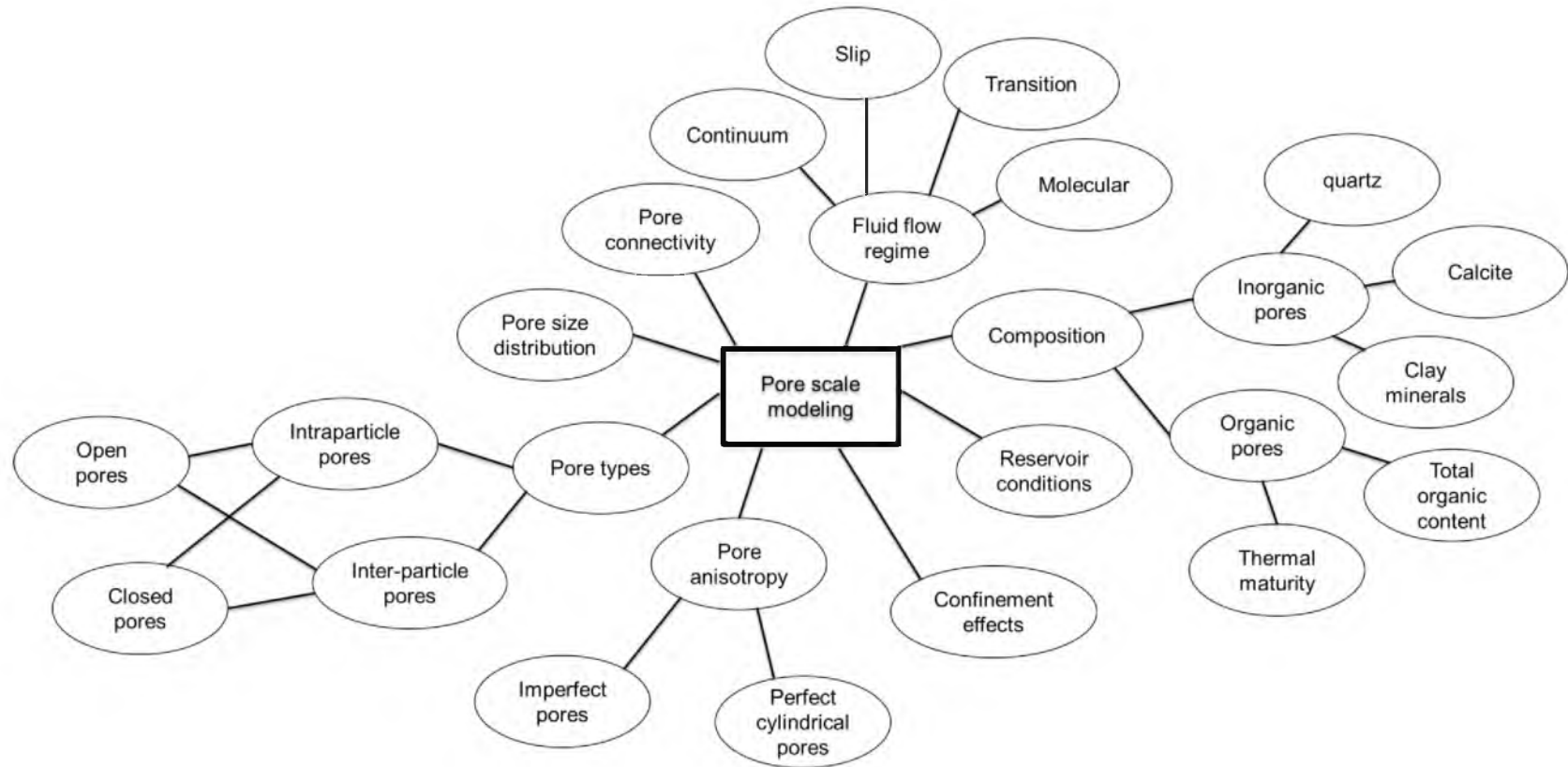
FIGURE 2.3 Factors affecting pore-scale fluid flow modeling and simulation in shale nanopores
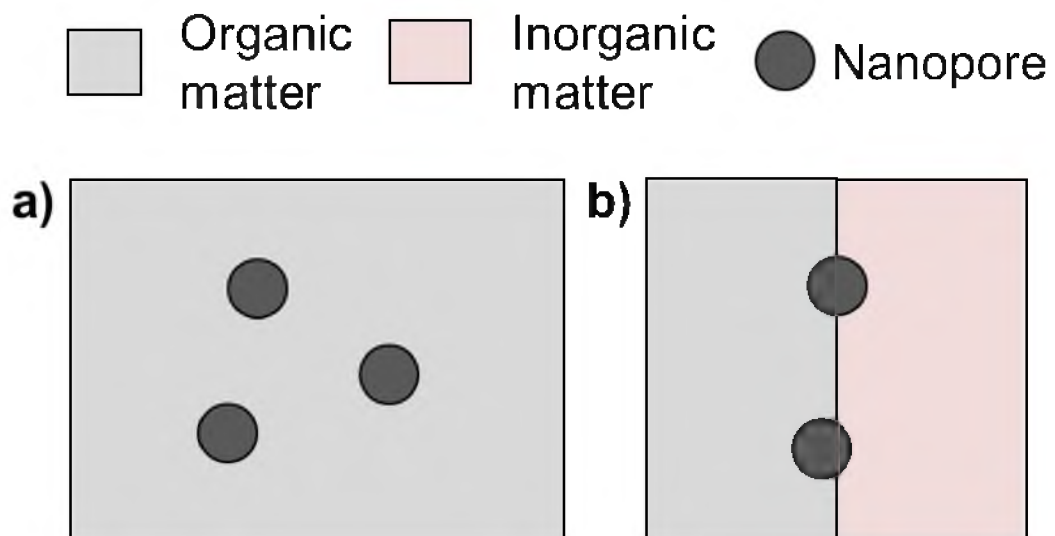
FIGURE 2.4 a) Intraparticle pores and b) Interparticle pores
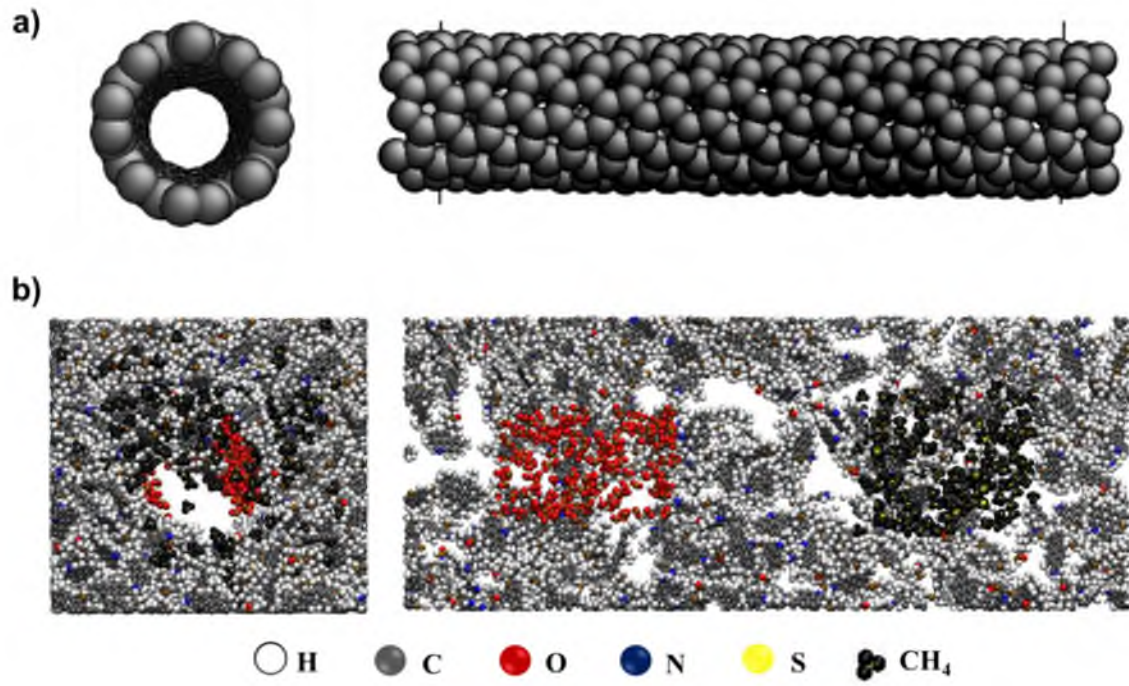
FIGURE 2.5 a) Ideal pore structure and b) Representative (realistic) pore structure
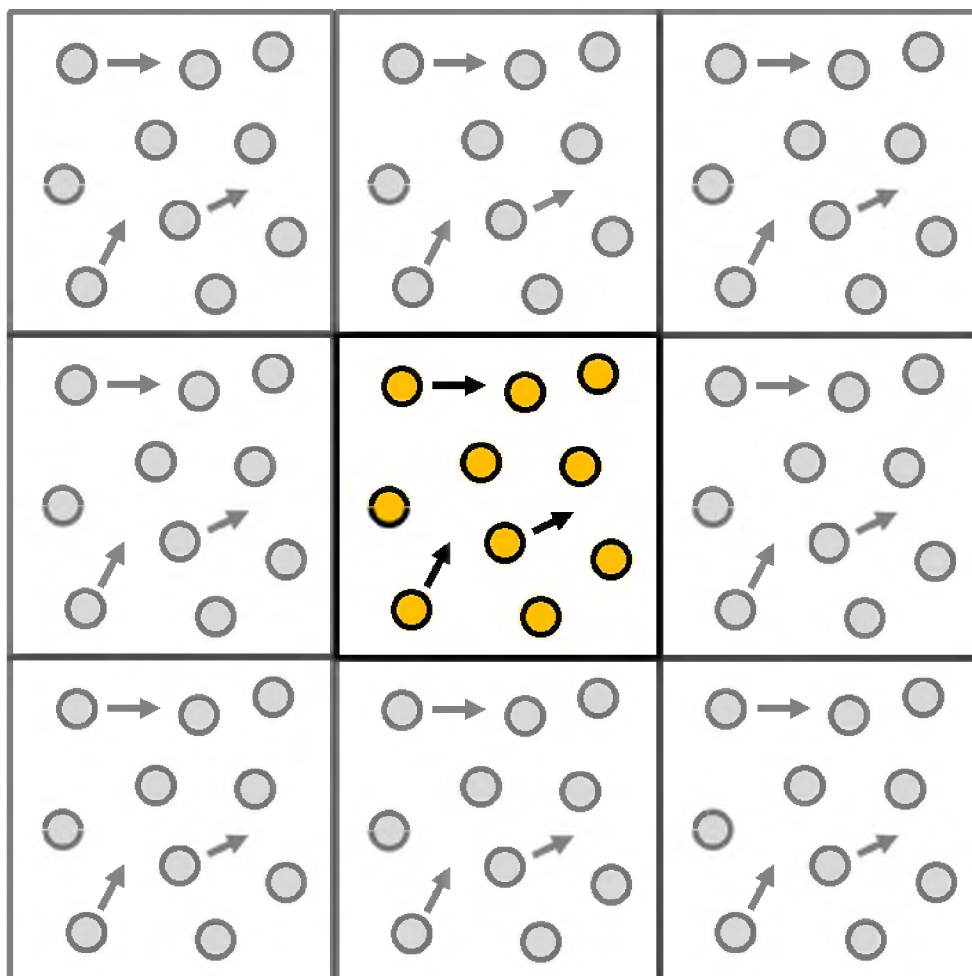
FIGURE 2.6 Periodic boundary condition
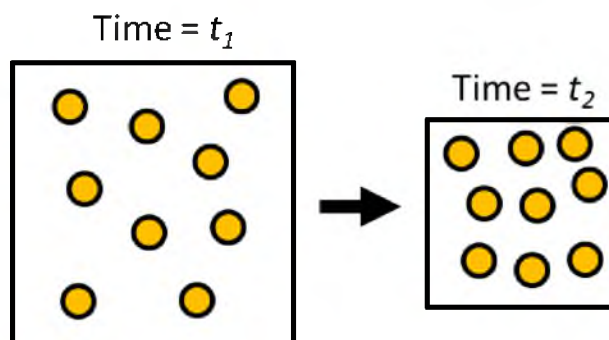
FIGURE 2.7 NPT ensemble
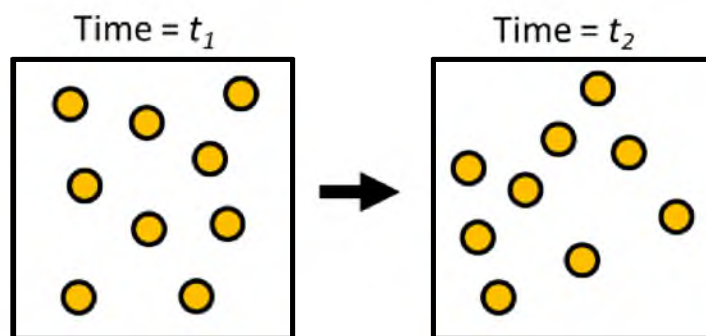
FIGURE 2.8 NVT ensemble
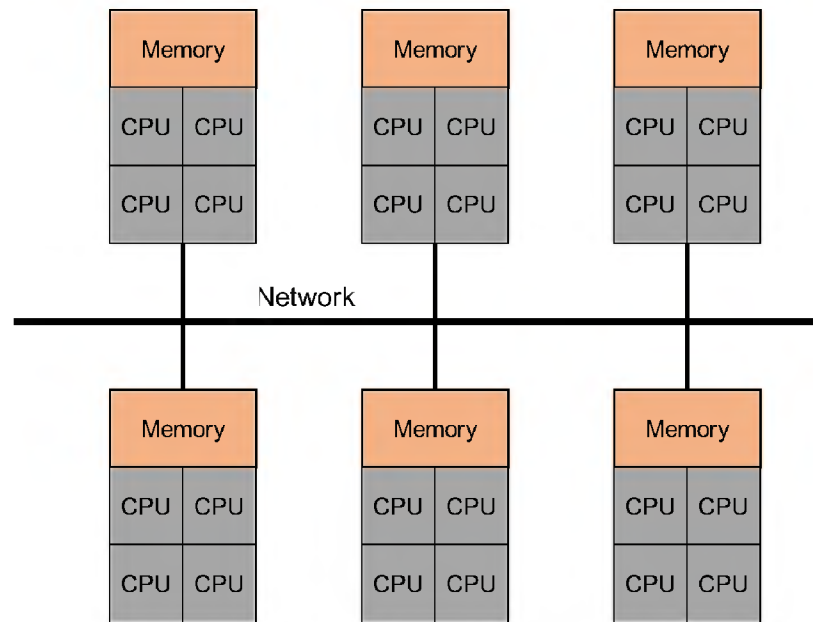
FIGURE 2.9 The typical modern parallel computer architecture
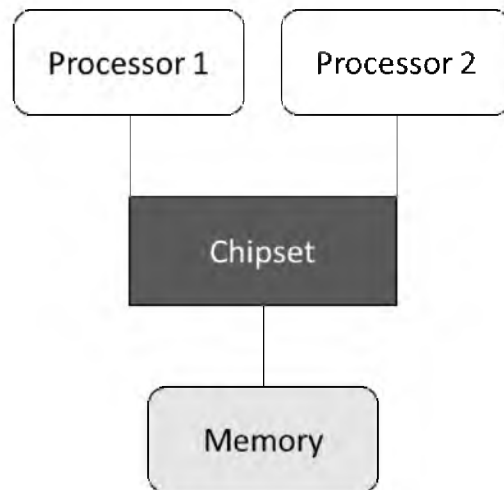
FIGURE 2.10 Shared-memory computer architecture

Communication network
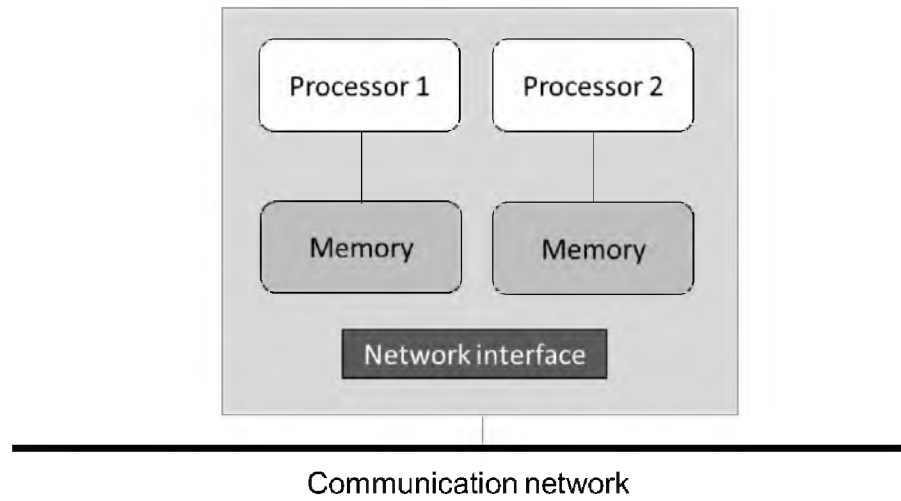
FIGURE 2.11 Distributed-memory architecture
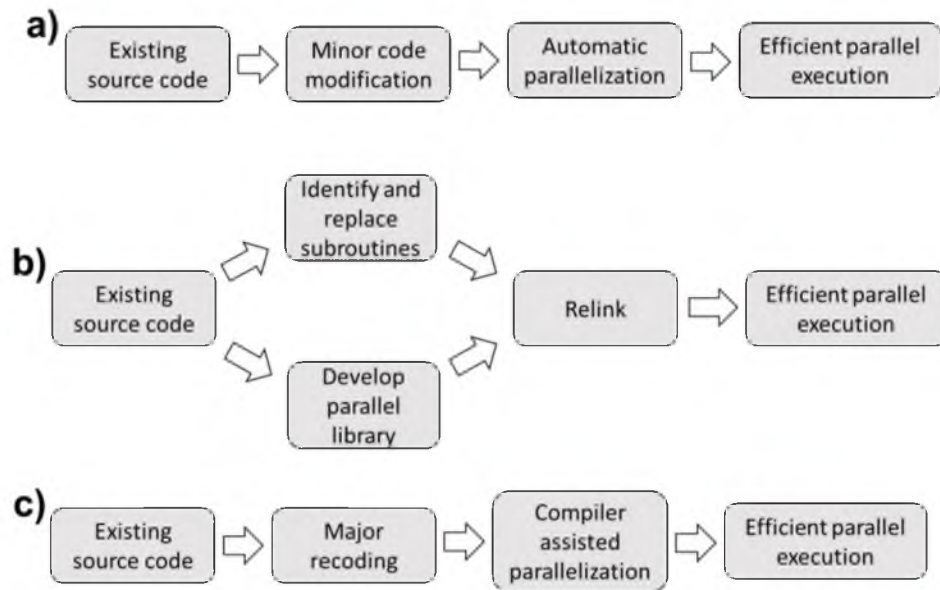
FIGURE 2.12 Porting strategies a) Automatic parallelization, b) Parallel libraries, and c) Major recoding
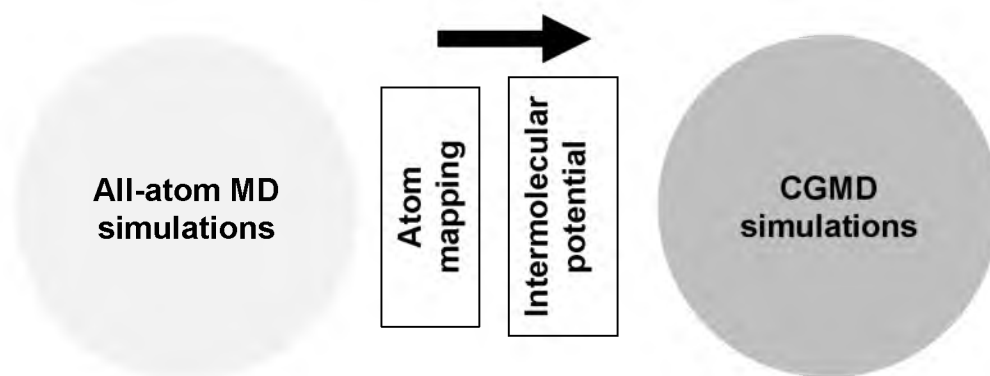
FIGURE 2.13 All-atom molecular dynamics to coarse-grained molecular dynamics
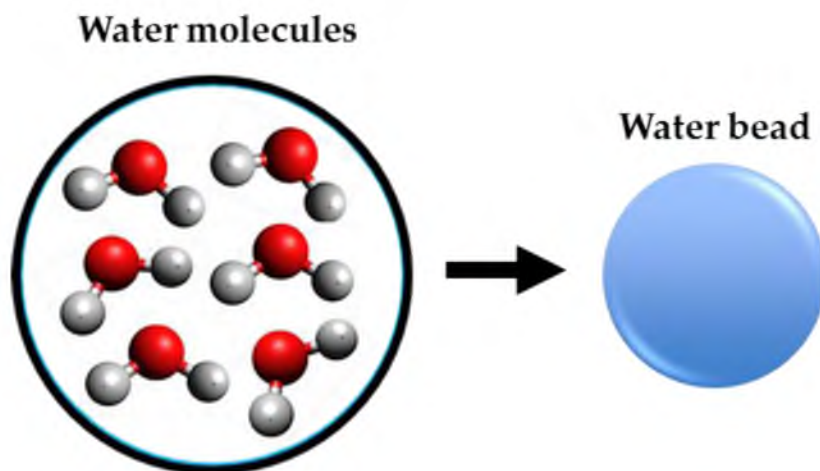
FIGURE 2.14 Schematic representation of mapping in CGMD

TABLE 2.1 Review of important studies summarizing shale structure, shale composition, and modeling and simulation in shales

Reference	Study	Main findings
(Firouzi and Wilcox 2012)	Molecular modeling to determine the transport properties of pure carbon dioxide, methane, nitrogen, and the binary mixtures nitrogen-carbon dioxide and methane-carbon dioxide in *3D carbon based pore network*	• Found that the pore morphology plays a significant role in flow and transport properties of fluids • Permeability is zero due to low pore connectivity (low porosity)
(Hao and Cheng 2010)	Performed pore-scale simulation of two-phase flow in packed-sphere bed and carbon paper gas diffusion layer with the lattice Boltzmann method	• Relative permeability of the packed bed evaluated with lattice Boltzmann method was in agreement with the experimental method
(Yan et al. 2013)	Simulation of two-phase microscale flow in shale reservoirs using the multiple porosity models	• Diffusion mechanism in kerogen plays an important role in the total gas production
(Firincioglu et al. 2012)	Extension of *vapor-liquid equilibrium calculations* to include the capillary and the surface van der Waals forces	• Phase behavior of liquid-rich reservoirs subjected to confinement effect, the capillary discontinuities and surface forces significantly deviates from conventional phase behavior • Phase behavior in unconventional reservoir depends on the pore geometry, the fluid configuration, and the mineralogical content of the pore surface
(Teklu et al. 2014)	Used modified *vapor-liquid equilibrium (VLE) calculations* to study the phase behavior of reservoir fluids in unconventional reservoirs	• Results showed that the bubble point pressure, gas/oil interfacial tension, and minimum miscibility pressure decreases with the confinement • Work applies to single pore size and *requires the model of unconventional matrix with surface-chemical heterogeneity and the pore size distribution*
(Takahashi and Kovscek 2010)	Experimental study of the spontaneous countercurrent imbibition in siliceous shale rocks	• Evaluated the water saturation profiles

TABLE 2.1 continued

Reference	Study	Main findings
(Roychaudhuri et al. 2013)	Experimental investigation of the spontaneous imbibition of water in Appalachian basin shale to investigate the role of the capillarity in the fluid loss mechanism	• The significant amount of injection fluid can be absorbed by the shale
(Curtis et al. 2011)	Investigated the relationship between organic porosity and thermal maturity in the Marcellus shale	• Observed no significant differences in pore sizes and the amount of porosity and emphasized the need for further investigation
(Wang and Reed 2009)	Investigated the effects of organic matter on the petrophysical properties, pore network and fluid flow in nonorganic matter, organic matter, natural fractures, and hydraulic fractures	• Significant amount of free gas stored in the organic matter • Gas permeability in organic matter is significantly higher than the nonorganic matrix
(Ahmad and Haghighi 2012)	Performed mineralogical, porosity, and petrophysical characterization of Roseneath and Murteree shale formations from southern Australia	• Concluded that the Roseneath and Murteree shale samples contain clay, organic matter, quartz, and fine-grained minerals • Observed linear/elongated, wedge-shaped, and triangular void spaces in these shale samples and the pores are of irregular size and shapes
(Bernard et al. 2010)	Performed multiscale characterization of an over-matured organic-rich calcareous mudstone from northern Germany with combination of transmission electron microscopy and scanning transmission X-ray microscopy	• Reported multiscale mineralogical and chemical heterogeneities from millimeter to the nanometer scale
(Chareonsuppanimit et al. 2012)	Measured adsorption isotherms of methane, nitrogen and carbon dioxide in New Albany shale samples from Illinois basin	• Found that adsorption in shales is an order of magnitude lower than the coals. Also, presence of ash reduces gas adsorption capacity of shales
(Falk et al. 2015)	Performed molecular dynamics and statistical mechanics to simulate the sub-continuum mass transport of condensed hydrocarbons in disordered carbon structure (used to represent the kerogen)	• Showed that the Darcy's law fails to describe the fluid transport in nanoporous media

TABLE 2.1 continued

Reference	Study	Main findings
(Hu et al. 2015)	Investigated the dynamics of water molecules and NaCl electrolytes confined in an activated kerogen and MgO pores	• Significant changes in the water distribution within the nanopores when surface roughness and surface functionalized groups incorporated in the kerogen structure
(Chalmers et al. 2012)	Characterized shale samples from Barnett, Woodford, Marcellus, Haynesville, and Doig shales to analyze the pore systems	• Observed that the kerogen, clay, and/or carbonate together holds most of the macropores and mesopores • Pore distribution and their orientation affect the fracture design • Pore structure in kerogen is very complex

TABLE 2.2 Fluid flow regimes in shale nanopores
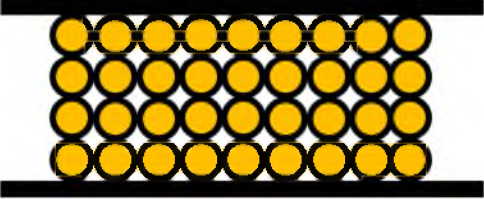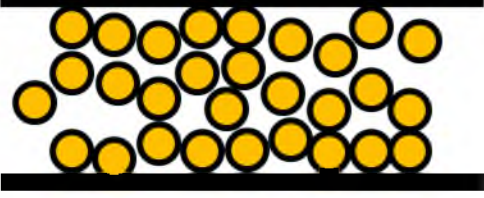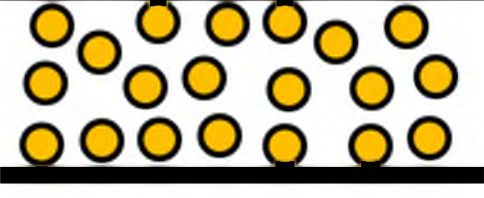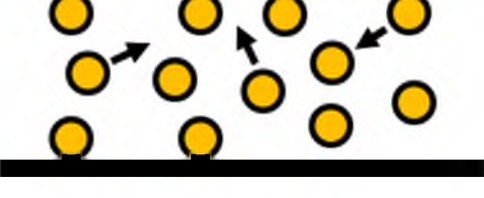
Fluid flow regime	Knudsen number (*Kn*)	Graphical representation
Continuum flow	$Kn \leq 0.001$	
Slip flow	$0.001 < Kn < 0.1$	
Transition flow	$0.1 < Kn < 10$	
Free molecular flow	$Kn \geq 10$	

TABLE 2.3 MD simulation applications

Reference	Study	Main findings/ Recommendations
(Wang et al. 2004)	Evaluated the effect of the carbon nanotube (CNT) diameter and helicity on the static properties of water molecules confined in armchair and zigzag CNTs	• The bulk water properties differ from water properties subjected to confinement
(Xu et al. 2012)	Investigated the effect of temperature on the fluid flow in CNTs as a function of pore radius and fluid transport rate	• Shear rate of fluid increases with the increased fluid transport rate • The length of the CNTs should be at least eight times the pore radius for the robust data collection
(Thornton et al. 2009)	Developed the mathematical model to study the transport of lighter molecules (methane and carbon dioxide) in carbon and silica slits and nanopores	• Described the theoretical pore size range for which activation, surface diffusion, and Knudsen diffusion mechanisms can be differentiated
(Hanasaki and Nakatani 2006)	Analyzed the water flow in a convergent nozzle consisting of carbon nanotube	• Observed the rise in the pressure and temperature in the convergent portion of the nozzle • Also, found the density difference in the upstream and downstream region of nozzle
(Chun-Yang and Mohanad 2009)	Characterized the effect of the force applied to liquid Argon on velocity and pressure profiles of liquid Argon	• Observed the noticeable difference observed in velocity and pressure profiles due to reduced effect of the attractive and the repulsive forces at the higher applied forces
(Huang et al. 2006)	Examined the entrance and exit effect on Argon molecules flow in the neutral and hydrophobic wall	• No difference observed in the pressure and velocity profiles in presence of the natural wall • A significant difference observed in streamwise velocity for the hydrophobic wall
(Hui and Chao 2012)	Evaluated the Behavior of Argon molecules in a Janus interface (molecular configuration with hydrophilic and hydrophobic interfaces)	• Observed nonlinear velocity profile, where the velocity profile is skewed more towards the hydrophobic surface
(Huang et al. 2010)	Analyzed the effect of the cut-off distance on the static and dynamic properties of Argon molecules	• Recommended the use of the minimum cut-off distance (four times the characteristics length of NVT simulations) to minimize the error in the dynamic fluid properties

TABLE 2.3 continued

Reference	Study	Main findings/ Recommendations
(Clarkson et al. 2012)	Discussed the need for better understanding of the transport of liquid hydrocarbons in unconventional reservoirs in presence of variable pore structure, mineralogical and organic content	• Did not mention how to tackle the fluid transport challenges in the presence of the variable pore structure, mineralogical and organic content
(Janecek and Netz 2007)	Performed the Monte Carlo (MC) simulation of adsorption and depletion of water molecules in presence of hydrophobic and hydrophilic surfaces	• Stressed the requirement of large number of simulation parameters to model complex systems (which will reduce the uncertainty in the results)

TABLE 2.4 Applications of GPUs in MD and CGMD simulations

Author	Applications	GPU Architecture	Speed up (max)
(Che et al. 2008)	Miscellaneous (Structured grid, unstructured grids, optimization problems, data mining)	NVIDIA GTX260	72
(Hou et al. 2013)	MD with many-body potentials	NVIDIA TESLA C2050	65.4
(Levine et al. 2011)	Analysis of MD trajectories for RDF histogramming	NVIDIA GeForce GTX480	92
(Anandakrishnan et al. 2010)	Evaluation of surface electrostatic potential for viral capside	ATI Radeon 4870	182.8
(Yokota et al. 2011)	Evaluation of the electrostatic interaction protein-drug binding	NVIDIA GTX295	26
(Shkurti et al. 2013)	GPU optimization of CGMD models	NVIDIA GTX480	14
(Chen et al. 2009)	MD study of cavity flow and particle-bubble interaction	NVIDIA Tesla C870	60
(Kim et al. 2012)	Characterization of zeolites to find local adsorption properties	NIVIDA Tesla C2050	50
(Rizk and Lavenier 2009)	Study of RNA folding mechanism	NVIDIA GTX280	17

TABLE 2.5 Coarse-grained molecular dynamics applications

Reference	Study	Major findings
(Riniker and van Gunsteren 2011)	Developed CG model of water and evaluated thermodynamic and physical properties of water	• The comparison of surface tension and the thermal expansion did not agree with the experimental results and SPC water model
(Gohlke and Thorpe 2006)	Performed CG simulation of biomolecules	• Compared the mobility of biomolecules evaluated with CGMD with the experimental results and found a good agreement
(Izvekov et al. 2005)	Utilized force-matching algorithm to develop CG model of C_{60} and carbonaceous nanoparticle from all-atom MD simulation	• Found good agreement in structural properties (radial distribution function) between CG and all-atom MD models
(Jusufi et al. 2011)	Investigated the effect of the fullerene size on their adsorption capacity into biomolecular bilayers	• Found good agreement for the potential mean force (PMF) with CG and all-atom MD models
(Baron et al. 2006)	Compared the configurational entropy properties of n-alkane up to hexa- and octa-decane	• Provided the guidelines to the check the quality of CG model that includes the model resolution, the CG mapping procedure, and the experimental verification to optimize the CG parameters
(Stukan et al. 2012)	Simulated the imbibition mechanism to understand the recovery of asphaltenic crude oil using surfactants	• Achieved the qualitative understanding of imbibition mechanism is nanopores
(Markutsya et al. 2013)	Simulated polysaccharide chains in cellulose and comparison with the all-atom MD simulations	• Emphasized the number of atoms that needs to be selected to form a bead (small number of beads will be still computationally expensive while large number of beads will reduce the accuracy of the simulations)

CHAPTER 3

PROBLEM STATEMENT

The inadequate understanding of the pore-scale multiphase fluid transport, in particular, the adsorption, absorption, and diffusion of hydrocarbons, in realistic organic and inorganic matrices is one of the many factors that affect the hydrocarbon recovery rates and economic development of unconventional resources such as shale reservoirs. As Darcy's law is not applicable for the nanoscale multiphase fluid transport simulation, a comprehensive modeling and simulation framework is required to improve our predictive capability. A molecular dynamics based workflow is presented in this dissertation that is used to:

- develop molecular models of nanometer and subnanometer pores found in organic and inorganic matrices,

- simulate the pore-scale multiphase fluid flow in these nanopores, and

- characterize the transport processes in nanometer and subnanometer pores.

The present research will enable the simulation of complex pore-scale fluid transport in unconventional reservoirs, which will enhance our predictive capability of hydrocarbon recovery from unconventional reservoirs.

CHAPTER 4

A MOLECULAR DYNAMICS SIMULATION WORKFLOW

4.1 Introduction

A workflow for molecular dynamics (MD) simulations of the pore-scale multiphase fluid transport in nano-structured inorganic pore is presented in this chapter. The workflow is comprised of three distinct phases. First, a molecular model of the pore, characteristic of unconventional source rocks with embedded nanopores, is developed. Then, MD simulations of the multiphase gas-liquid flow in the pore are performed using LAMMPS (Large-scale Atomic/Molecular Massively Parallel Simulator), an open source molecular dynamics package developed by Sandia National Laboratory (Plimpton 1995). Finally, upscaling of MD simulations to longer time scales, using a highly scalable parallel computing algorithm, is tested. An application of the proposed workflow is demonstrated by simulating a pore-scale cocurrent imbibition of water in a methane-saturated pore. Various flow properties under nano-confinement, including the mean square displacement (MSD) and the effective diffusion coefficient of water and methane, are evaluated and the simulation scalability is tested for up to 600 computing cores.

4.2 MD model development

Typical MD simulation workflow consists of three distinct stages: initial system definition, a solution of equations of motion, and analysis of atomic trajectories and determination of key system parameters (Haile 1993). Figure 4.1 summarizes these three

stages, and a brief description of tasks performed in each stage is described in the subsequent paragraphs.

The accuracy of the MD simulation is highly dependent on a precise description of the atomistic structure and model geometry. Description of the initial molecular configuration, which includes the assignment of all fundamental atomic properties including the mass, partial atomic charges, and the interatomic potential between atoms/molecules, is performed during the first stage. The key model parameters, which are used to characterize the atomic interactions, are assigned based on the force field.

In the second stage, the equations of motion are solved to obtain temporal positions of the atoms. Various numerical schemes can be used. The most widely used solution scheme is the velocity Verlet algorithm, due to its simplicity and minimal computational and data storage requirements (Young 2004). The general form of the equation of motion can be written as (Ungerer et al. 2005):

$$F_i = m_i \frac{d^2 r_i}{dt^2} \qquad (4.1)$$

and, expressed as a function of the total potential energy of the system, Equation 1 becomes:

$$F_i = \nabla \big(U(r_i) \big) \qquad (4.2)$$

where, m_i is the mass of an atom, r_i represents (x, y, z) coordinates of an atom, and U is the total potential energy of the system. In the absence of information about the kinetic energy of the system, the total potential energy can be estimated using bonded (E_b) and non-bonded (E_{nb}) atomic interactions:

$$U = E_b + E_{nb} \tag{4.3}$$

The bonded atomic interaction consists of bond stretching (E_B), bond bending (E_A), and the dihedral angle torsion (E_T) while the nonbonded interactions consist of van der Waal's (E_{vdW}) contribution and the electrostatic (E_C) contribution. The individual energy terms are given below (Equations 4.6 - 4.10):

$$E_b = E_B + E_A + E_T \tag{4.4}$$

$$E_{nb} = E_{vdW} + E_C \tag{4.5}$$

$$E_B = \frac{1}{2}K_e(R - R_e)^2 \tag{4.6}$$

$$E_A = \frac{1}{2}K_\theta(\theta - \theta_e)^2 \tag{4.7}$$

$$E_T = \frac{1}{2}V\{1 - cos[n(\emptyset - \emptyset_e)]\} \tag{4.8}$$

$$E_{vdW} = 4\varepsilon\left[\left(\frac{\sigma}{r}\right)^{12} - \left(\frac{\sigma}{r}\right)^{6}\right] \tag{4.9}$$

and

$$E_C = C\frac{q_i q_j}{\epsilon r} \tag{4.10}$$

The Lorentz-Berthelot rule (Anderson et al. 2005; Hui and Chao 2012),

$$\varepsilon_{ij} = \sqrt{\varepsilon_i \varepsilon_j} \tag{4.11}$$

and

$$\sigma_{ij} = \frac{\sigma_i + \sigma_j}{2} \tag{4.12}$$

are used to calculate the van der Waals parameters for dissimilar atoms.

To minimize the total computational time and provide an accurate representation of the underlying processes, a number of MD simulation parameters have to be accurately selected and optimized prior to simulation. Table 4.1 summarizes some important simulation parameters and their potential impact on the MD simulation results.

In the last stage, the atomic trajectories evaluated at different time steps are used for qualitative and quantitative analysis of the underlying physical processes. In this study, which is focused on the investigation of multiphase fluid flow in nano-confined geometry, diffusion coefficients and spatial variation of the number densities of both methane gas (displaced phase) and water (displacement fluid) are evaluated.

4.3 MD simulation of the cocurrent imbibition in inorganic pore

An MD simulation of cocurrent imbibition of water in nano-structured inorganic pore saturated with methane gas is performed using LAMMPS. An inorganic pore consisting of amorphous quartz is used in this study. The cross-section of the pore is shown in Figure 4.2. The length and the diameter of the pore are 5-nm and 80-nm, respectively, whereas the pore wall thickness is 2-nm. The pore structure is fixed to maintain the integrity of the pore during the simulation and to avoid the pore collapse. A total of 1,500 water

molecules, 1,500 methane molecules, and 14,000 unit quartz structures were used in the simulation. Each quartz unit structure consists of three silicon and six oxygen atoms. A number of molecules used in the simulation are selected to get accurate representation of the system while minimizing the total computational cost of the MD simulations.

The SPC/E model (Mark and Nilsson 2001) is used to simulate water molecules; methane molecules were simulated as independent rigid bodies (Ungerer et al. 2005). The MD simulation parameters used in the present study are summarized in Table 4.2. For dissimilar atoms, the Lorentz-Berthelot rule is used to estimate the ε (interatomic potential well depth) and σ (distance at which the interatomic potential is zero) parameters.

The particle-particle particle-mesh (pppm) algorithm is used to evaluate the long-range Coulombic interactions having a tolerance of $1e^{-5}$ (in per-atom force calculation) with the cut-off distance of 12 Å. A periodic boundary condition is utilized in all directions. The system is simulated in the NVE ensemble, and the Langevin thermostat is used to maintain the system temperature at the desired level. An adaptive time stepping is used to perform the time integration with minimum and maximum time steps of 0.00001 fs and 0.1 fs respectively. The atomic trajectory information is stored at every 1,000 time steps and is used to evaluate the mean square displacement (MSD) of water and methane.

Further, the effective diffusion coefficients of water and methane molecules are also evaluated using Equation 4.13.

$$D = \frac{1}{6}\frac{\langle |r(t) - r(0)|^2 \rangle}{t} \qquad (4.13)$$

The diffusion coefficient reported for water and methane are the effective diffusion coefficient in the quartz nanopore, as they are the result of interactions between the fluid-

fluid molecules, as well as the fluid molecules-pore surface at a 0 Kcal/mol-Å applied force (no externally applied force) to water molecules.

Finally, the methane number density is determined as a function of time, applied force to the water molecules, and the system temperature. The resulting methane number density is used to evaluate methane distribution within the pore and on the pore surface, and to assess the impact of above-defined attributes on the methane behavior inside the quartz pore.

4.4 Results and discussion

Figure 4.3 shows the comparison between overall water and methane displacements in quartz nanopore along the x-direction at two distinct times — at the beginning, and at the intermediate time — to examine the impact of the various applied forces on methane recovery. Three distinct scenarios are depicted in Figure 4.3 where the force of 0 Kcal/mol-Å, 0.1 Kcal/mol-Å, and 1 Kcal/mol-Å were applied to each atom of water molecules. The visual molecular dynamics (VMD) package (Humphrey et al. 1996) is used for all visualization.

From Figure 4.3 a), it can be observed that the overall water and methane molecules displacements are small at the 0 Kcal/mol-Å force, and the primary mode of transport, in this case, is the diffusion caused by the fluid (water and methane) and the pore surface (quartz) interactions. A very small displacement of water and methane show the typical characteristics of unconventional reservoirs having extremely slow hydrocarbon recovery rates. Further, significant water and methane displacements were observed for an applied force of 1 Kcal/mol-Å to water molecules and are shown in Figure 4.3 c). Thus, it implies the requirement of the higher applied force to water molecule (numerically, force of 1

Kcal/mol-Å = 69.5 pN) to overcome the dominant fluid-pore surface interactions and to enhance the hydrocarbon recovery rates from unconventional reservoirs.

4.4.1 The mean square displacement and the effective diffusion coefficient

Figures 4.4 and 4.5 show the mean square displacement (MSD) of water and methane molecules for various applied forces (AF) to water molecules. From Figure 4.4 and Figure 4.5, it can be observed that the MSD of water and methane increases with an increase in a cumulative simulation time and the applied force to water molecules, as expected. Further, the MSD of methane was higher than the MSD of water. In addition, the effective diffusion coefficient of water and methane in the quartz nanopore is calculated with Equation (13) and summarized in Table 4.3. The time steps between 950,000 and 1,000,000 (time between 0.09 and 0.095 ns) were used to calculate the diffusion coefficients. From Table 4.3, it can be seen that the effective diffusion coefficient of methane is higher than the effective diffusion coefficient of water. Further, the effective diffusion coefficient increases with an increase in the temperature of the system.

4.4.2 The number density

Figures 4.6 and 4.7 show the variation of the methane number density along the y-direction, at the temperature of 340 K and 360 K, for various applied forces to water molecules. The number densities reported at 0 ps represent the distribution of molecules after a small fraction of time when the actual data logging process started. From Figures 4.6 and 4.7, it is observed that the methane number density is higher around the center of the pore at the beginning of the simulation and becomes wider near the pore wall as the simulation progresses, suggesting the enhanced rate of adsorption on the pore wall is due

to the influence of fluid-pore surface interactions. Further, Figures 4.6 and 4.7 show that the methane distribution is skewed towards the lower side of the pore, which is the direct consequence of the initial distribution of water molecules inside the pore as shown in Figure 4.8.

At 0 Kcal/mol-Å applied force, the rate of molecule getting closer to the pore surface is low and increases with an increase in the applied force (shown in Figure 4.9). Also, the water molecules near the pore wall prefer to remain on the wall, even under the influence of high applied forces to water molecules, thus indicating the water retention by the pore surface during the hydrocarbon recovery process. Further, the water molecules away from the pore wall undergo displacement and are primarily responsible for the displacement of the methane molecules.

The double methane density peak is observed when the force on the water molecules increases. For 0.1 Kcal/mol-Å force on water molecules, the double number peak is observed but becomes more evident for 1 Kcal/mol-Å force. By increasing the system temperature to 360 K, similar behavior is observed in the methane number density (shown in Figure 4.7), except the methane number density peak becomes wider near the pore wall, suggesting the enhanced rate of adsorption on the wall.

4.4.3 Extension of MD simulation capability for longer time scale with massively parallel CPU-based computing

MD simulations are computationally expensive and most of the simulation time is used to calculate the long-range electrostatic interactions. Figure 4.10 shows the typical time utilization in MD simulations. There are many MD simulation parameters, which play a significant role in the total simulation time, e.g., the force field used to characterize the

molecular interaction, and the cut-off distance to calculate electrostatic interactions. However, due to the advent of modern CPU- and GPU-based computational capabilities, it is possible to extend the capability of MD simulations for longer simulation times (Hou et al. 2013; Levine et al. 2011; Pohl and Heffelfinger 1999).

In the present study, a different number of computing cores were used to compare the computational efficiency and the scalability of the MD simulations with a large number of massively parallel CPUs. The comparison of total simulation time is shown in Figure 4.11. It can be observed that the total computational time decreases with an increase in a number of cores used. However, the observed trend of the total computational time is not linear. This is potentially due to the distribution of various MD simulation tasks on different cores and the increased intercore communication time with a large number of cores.

In summary, the molecular dynamics simulation-based workflow is presented to model and simulate the pore-scale multiphase fluid transport in organic/inorganic phases, containing nanopores. An example of a cocurrent imbibition mechanism (water displacing methane) in a quartz pore is shown to demonstrate the application of the proposed workflow. The diffusion coefficient and the number density of methane were evaluated to obtain insight into the pore-scale methane recovery process. Overall, the proposed workflow will enable the simulation of complex pore-scale fluid transport in unconventional reservoirs, which will enhance our predictive capability of hydrocarbon recovery from unconventional reservoirs.

MODEL CONFIGURATION

Definition of atomic unit structures
(building blocks)

Packing of the building blocks into
representative 3D model

Definition of atomic properties
(charge, mass, interatomic potential)

**SOLUTION OF EQUATIONS
OF MOTION**

Initial state of the system
(position, velocity)

Time step definition (Δt) and total
simulation time

Definition of thermostat properties

**ANALYSIS OF ATOMIC
TRAJECTORIES**

Evaluation of atomic trajectories at
different time-steps

Qualitative and quantitative analysis
of underlying physical processes

*This study:
Estimation of diffusion coefficients
and spatial distribution of number
density of displaced phase and
displacement fluid*

FIGURE 4.1 MD simulation stages
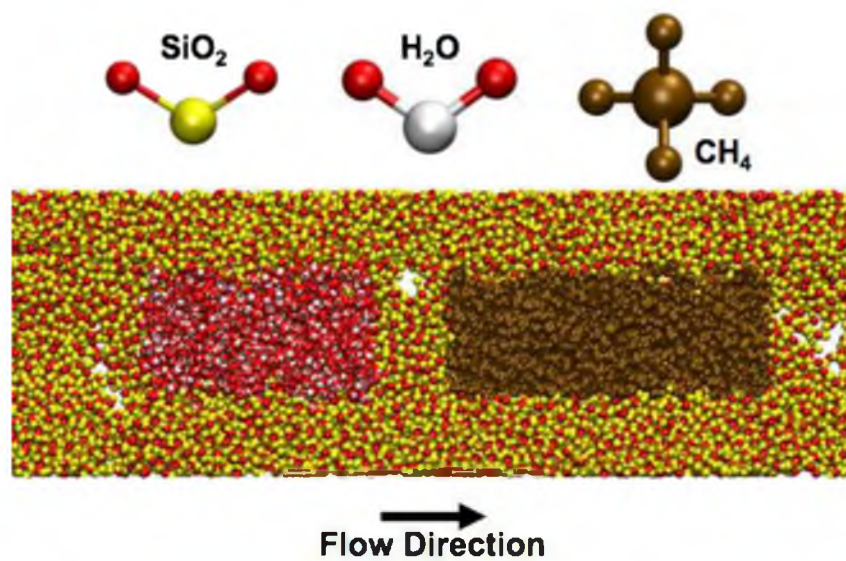
FIGURE 4.2 Atomistic representation of a methane saturated pore model
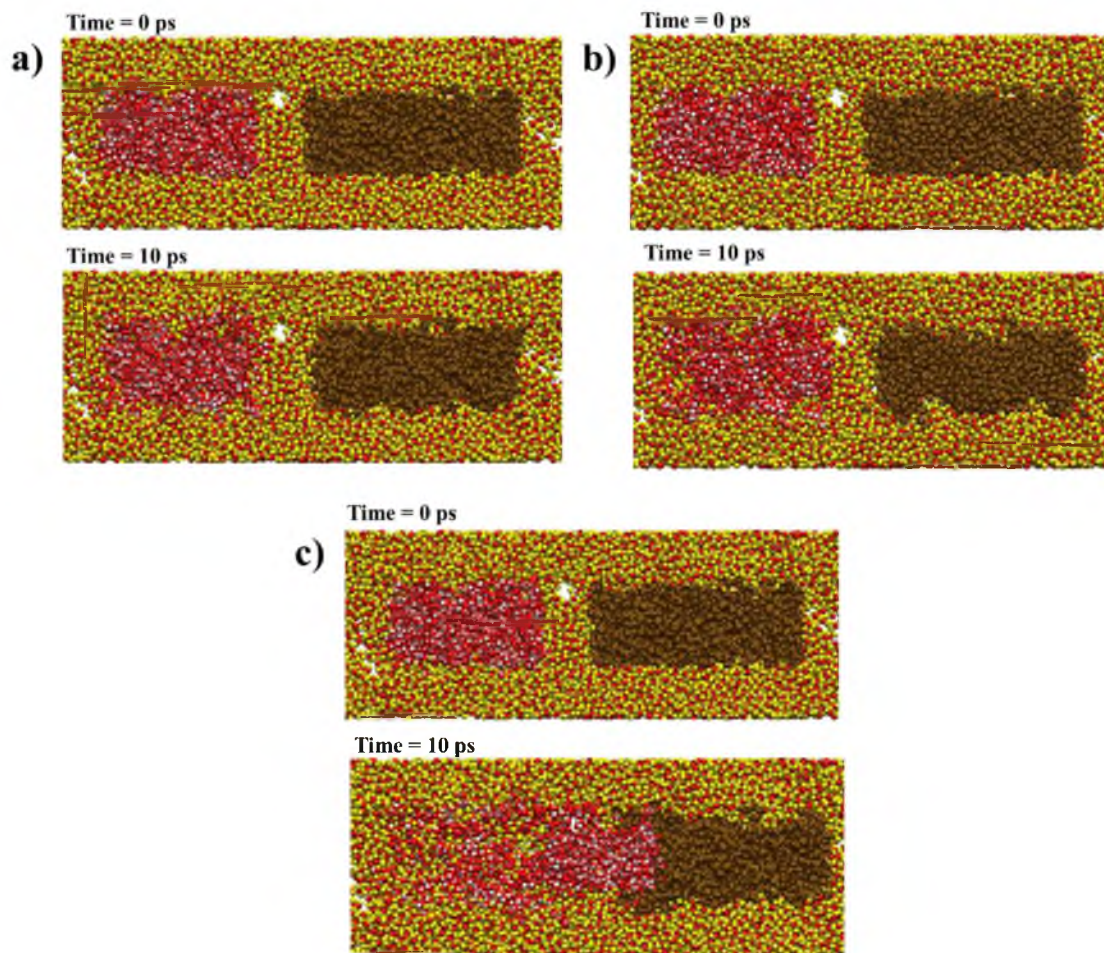
FIGURE 4.3 Fluid molecules at different time steps for three applied injection forces: a) 0 Kcal/mole-Å, b) 0.1 Kcal/mole-Å, and c) 1 Kcal/mole-Å
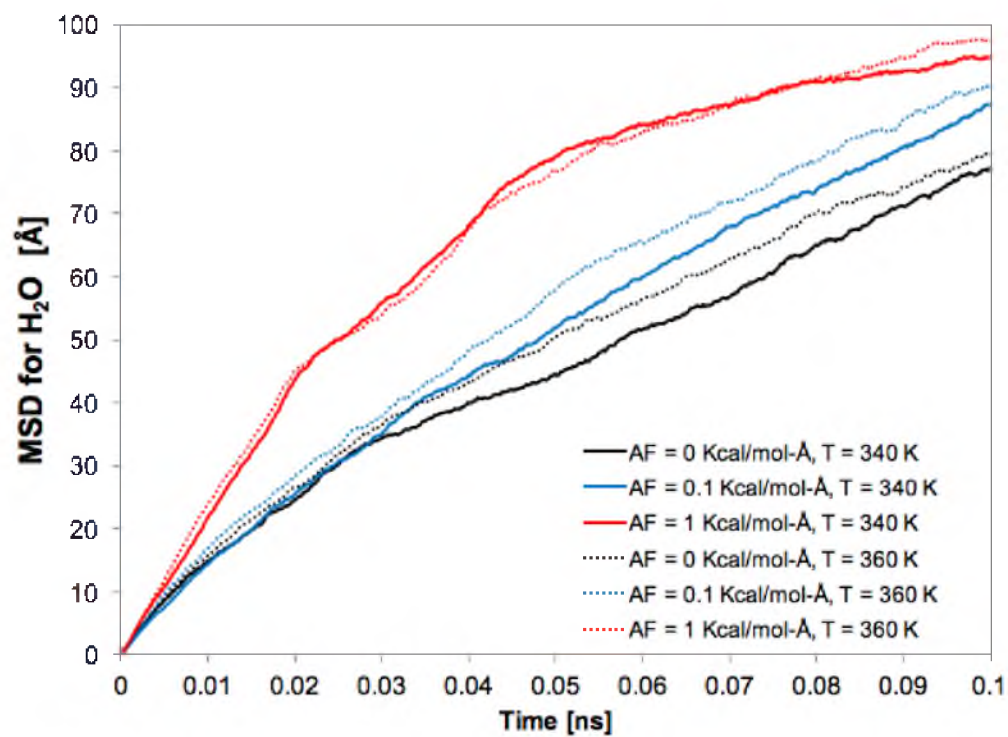
FIGURE 4.4 Mean square displacements of water at 340 and 360 K
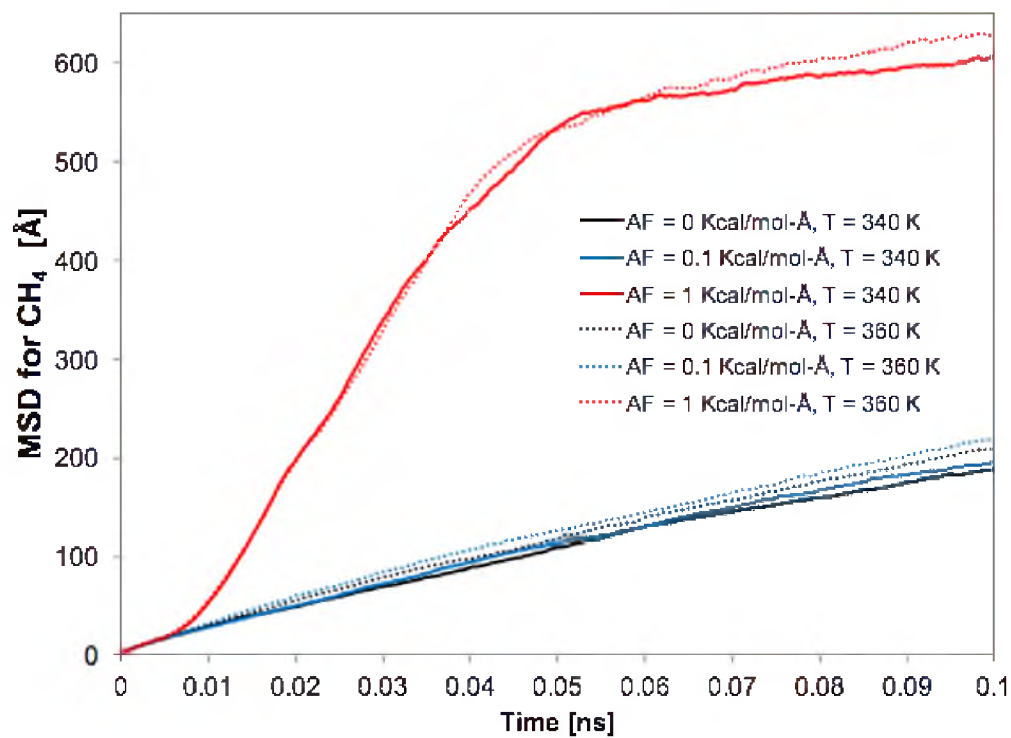
FIGURE 4.5 Mean square displacements of methane at 340 and 360 K
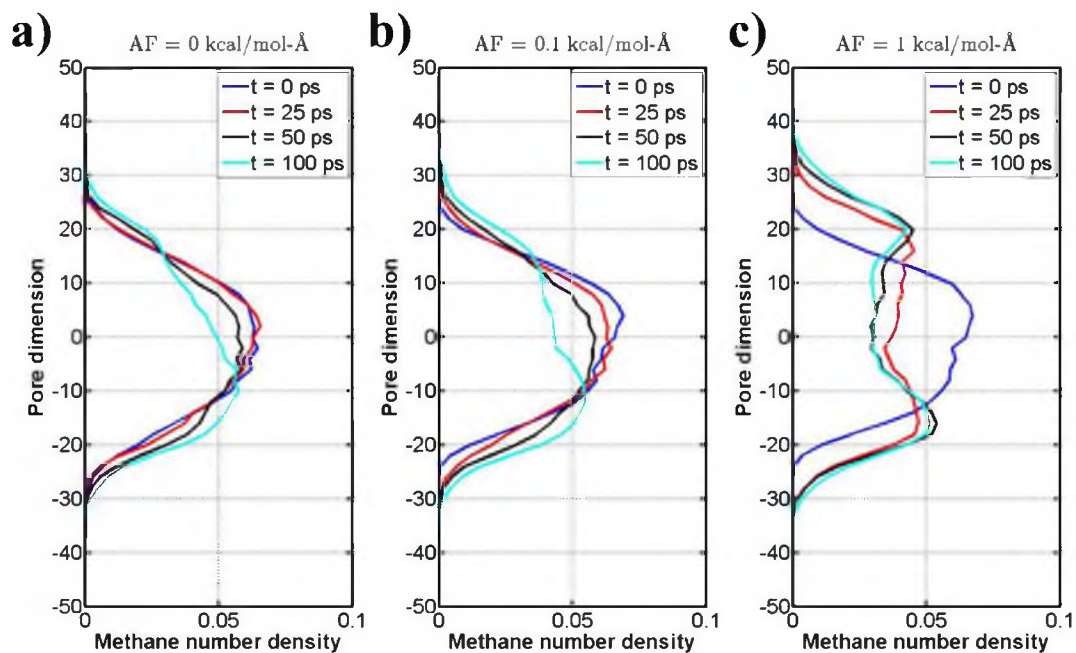
FIGURE 4.6 Methane number density at 340 K and applied force to water of a) 0 Kcal/mol-Å, b) 0.1 Kcal/mol-Å, and c) 1 Kcal/mol-Å (the "pore dimension" axis represents the pore system dimension in y-direction (which includes the pore diameter and the pore wall) measured in Å, where 0 represents the center of the pore)
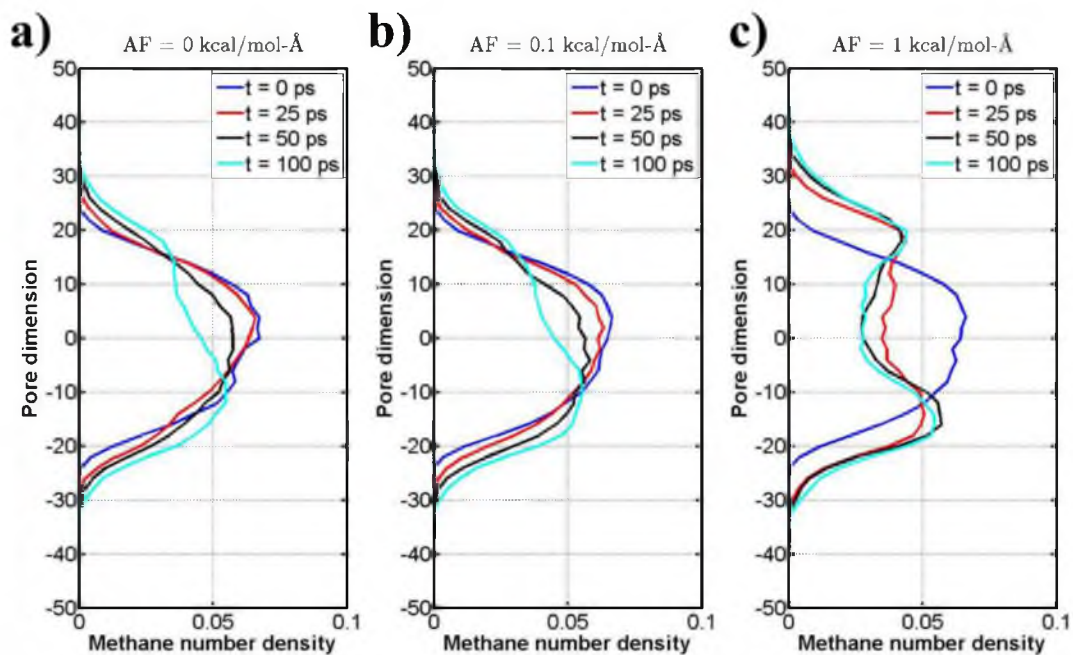
FIGURE 4.7 Methane number density at 360 K and applied force to water of a) 0 Kcal/mol-Å, b) 0.1 Kcal/mol-Å, and c) 1 Kcal/mol-Å
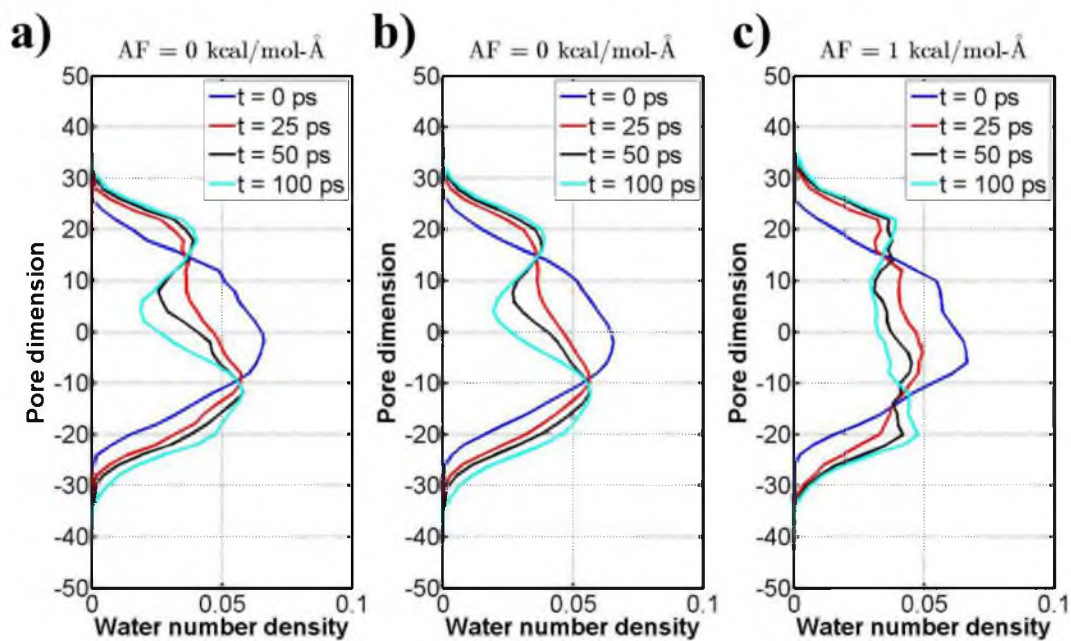
FIGURE 4.8 Water number density at 340 K and applied force to water of a) 0 Kcal/mol-Å, b) 0.1 Kcal/mol-Å, and c) 1 Kcal/mol-Å
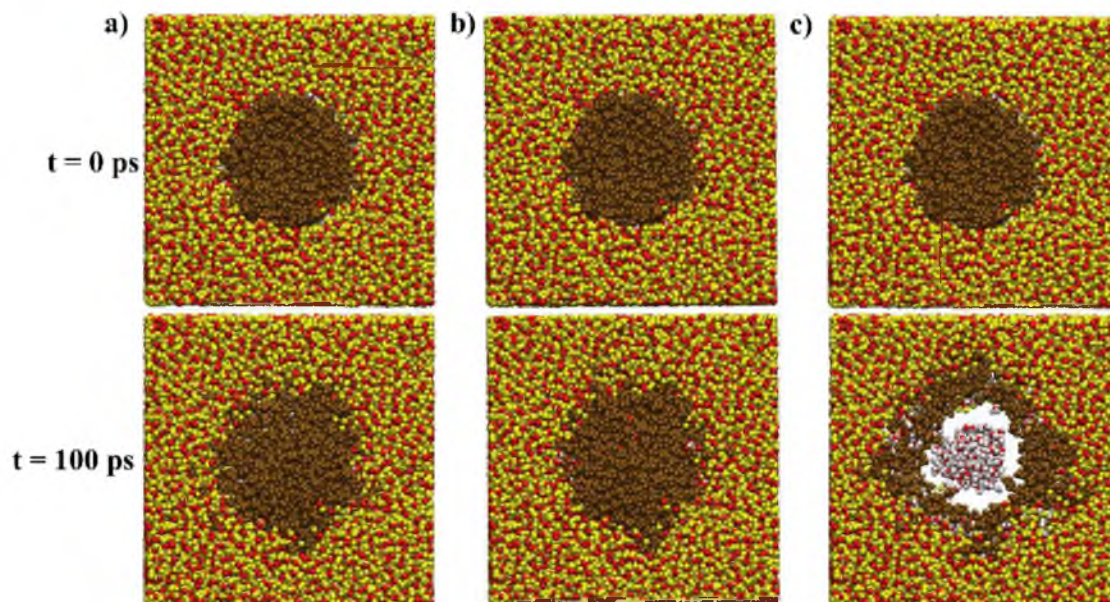
FIGURE 4.9 Methane distribution within the pore at 340 K and applied force to water of a) 0 Kcal/mol-Å, b) 0.1 Kcal/mol-Å, and c) 1 Kcal/mol-Å
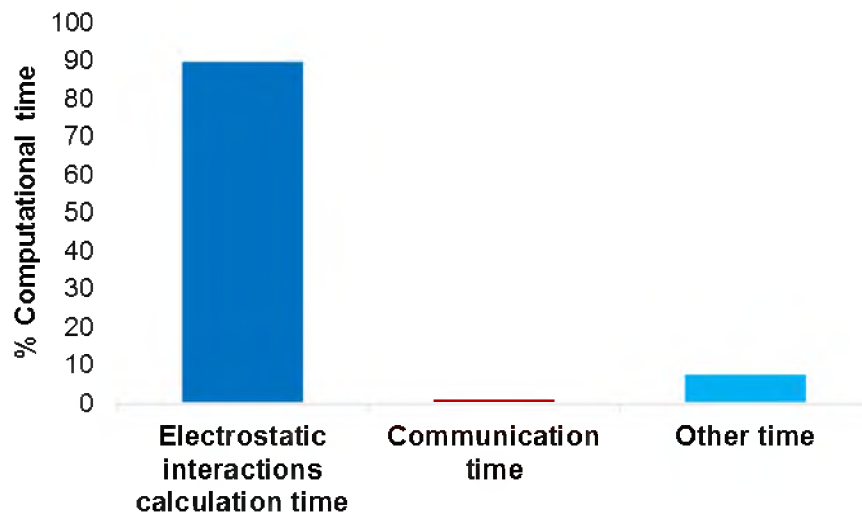
FIGURE 4.10 Typical computational time utilization in pore-scale MD simulation with 600 computing cores and 25,000 time-steps
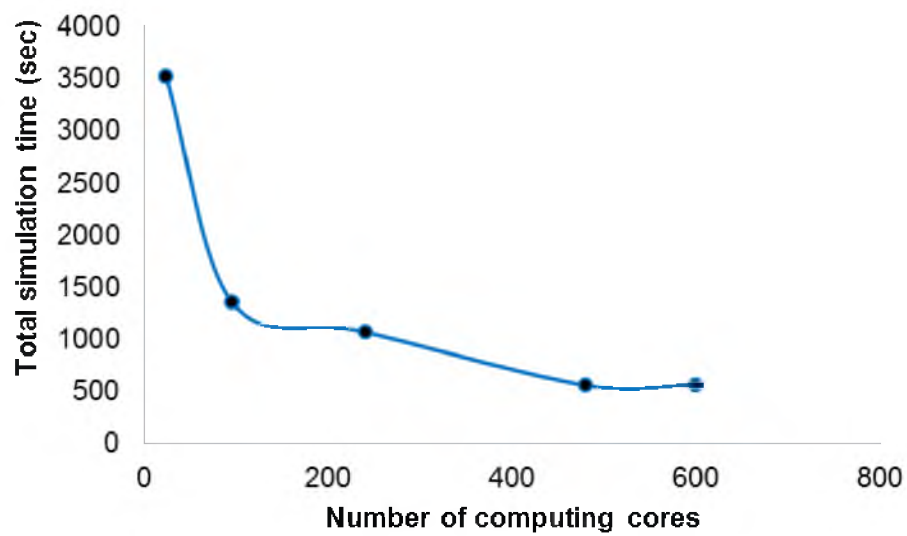
FIGURE 4.11 Computational performance of the typical pore-scale MD simulations for 25,000 time-steps with a different number of computing cores

**TABLE 4.1 MD simulation parameters optimization and
their potential impact on the simulation results**

Parameter	Aspect of the MD simulation
Time step	• Affects the total simulation time • Larger time step reduces the number of simulation steps and time but decreases accuracy of the simulation
Total simulation time	• Shorter simulation time affects the convergence of the system to equilibrium state (particularly for slow fluid flow and transport processes, which are characteristics of unconventional reservoirs) • Many quasi-equilibrium states can exist at a given temperature, and longer simulation times are required to ensure that the system has reached equilibrium
Cut-off distance	• Affects the total simulation time and the accuracy of the simulation • Smaller cut-off distance results in shorter simulation time but reduces accuracy • Large cut-off distances lead to improved accuracy but higher computational cost
Force field	• Affects the predicted system properties • Improper force field selection may lead to simulation results that deviate from experimental observations
Trajectory information storage frequency	• Too frequent storing of trajectory information results in an extremely large data file, which is particularly difficult to handle, analyze, and visualize • Less frequent data logging results in a loss of simulation details

TABLE 4.2 MD simulation parameters

Parameter	ε [kJ/mol]	σ [Å]	q [e⁻]	Reference
O (water)	0.6502	3.166	-0.8476	(Reed and Westacott 2008; Zielkiewicz 2005)
H (water)	-	-	0.4238	(Reed and Westacott 2008; Zielkiewicz 2005)
C (methane)	1.231	3.73	-	(Docherty et al. 2006; Reed and Westacott 2008)
Si (quartz)	0.5335	3.795	2.4	(McCaughan et al. 2013)
O (quartz)	0.6487	3.154	-1.2	(McCaughan et al. 2013)

TABLE 4.3 The effective diffusion coefficient of water and methane at 340 and 360 K

Fluid	Effective diffusion coefficient, $D \times 10^{-9}$ m^2/s	
	T = 340 K	T = 360 K
Methane	2.15	2.16
Water	0.83	1.08

CHAPTER 5

EXTENSION OF THE GENERAL-PURPOSE DREIDING

FORCE FIELD TO MODEL KEROGEN

5.1 Introduction

Hydrocarbon production from unconventional resources has grown enormously in recent years, due to advances in recovery methods, including hydraulic fracturing, fracture propping, and directional drilling, but the overall hydrocarbon recovery factors from these hydrocarbon accumulations have remained much lower than the recovery rates from conventional reservoirs. The lower recovery factors are due, in large part, to the nanoscale porosity, large specific surface area, and the high solid organic matter (kerogen) content of the host rocks, which results in very low permeability, very high capillary pressures, and a variety of hydrocarbon sorption phenomena.

In particular, the adsorption and absorption of hydrocarbons and other small molecules by kerogen, and the transport of small molecules in kerogen plays a significant role in the retention of hydrocarbons in source rocks and the production of oil and gas from kerogen containing tight rocks. A better understanding of these processes, at the molecular level, could provide a rational basis for the development of new improved recovery technologies.

However, the development of representative kerogen models is challenging because of its complex and heterogeneous nature that depends on the biological precursors

and the processes that occur during diagenesis and catagenesis. Kerogens do not have well-defined chemical structures, and because of their various biological origins, and possibly, because they underwent different biogeochemical transformations during diagenesis, one kerogen particle may have a different chemical composition and a different morphology than another kerogen particles that are separated from it by distances on the order of only 1 μm. It is likely that most of the organic matter in a kerogen particle consists of one or more enormous cross-linked macromolecules that would be much too large to simulate using molecular dynamics.

Various two-dimensional (2D) (Behar and Vandenbroucke 1987; Siskin et al. 1995) and three-dimensional (3D) (Liu et al. 2015; Orendt et al. 2013) kerogen models have been developed to obtain the representative kerogen structure. Two-dimensional models define the way in which the atoms are connected by chemical bonds, and three-dimensional models describe, in addition, the way in which the molecule pervades three-dimensional space.

Several force fields including the ReaxFF (Liu et al. 2015), PCFF+ (Collell et al. 2014; Ungerer et al. 2014), MM+ (Orendt et al. 2013) have been used in the literature to model and simulate the behavior of kerogen on the molecular level. The outcome of any molecular dynamics simulation, including the predicted equilibrium state and transport properties, depends on the force field. For some applications such as the development of a better understanding of generic behaviors, simple force fields such as the Lennard-Jones and Born-Lande (electrostatic plus short range repulsion) force fields can be used. On the other hand, tailored force fields have been developed for some commercially and scientifically important materials, such as silicon and water. For complex and variable

organic materials such as kerogens, which contain C, H, O, N, and S atoms, the simplest force fields cannot be used to obtain results of predictive value, and tailored force fields, based on quantum mechanical calculations and/or optimization to reproduce key physical properties are often not practical. Hence, generalized force fields, such as the DREIDING force field (Mayo et al. 1990) provide a reasonable compromise between the simplest force fields that reduce the computational burden, facilitate the simulation of larger systems, or enable processes with longer physical time scales to be simulated, and tailored force fields that are costly in terms of human resources.

The primary purpose of the present chapter is to investigate the capability of the general-purpose DREIDING force field to simulate a kerogen and evaluate it by comparison of molecular modeling results with experimental and simulation results reported in the scientific literature, bearing in mind the limitations of representative molecular structure models for kerogen. This chapter is organized into sections as follows.

- Section 5.2 describes the development of realistic kerogen matrix models of Type I (immature), Type II (middle-end oil window), and Type III (over matured) kerogens.

- Section 5.3 includes the explanation of the DREIDING force field that will be significant to parametrize the DREIDING force field for the Type I, Type II, and Type III kerogens.

- Section 5.4 provides the molecular simulation details. Finally, Section 5.5 discusses the results obtained for kerogen density and atomic pairwise distribution function for each kerogen type and the comparison of the results with the prior experimental and simulation results from the literature.

5.2 Development of a realistic kerogen matrix model

Twenty identical unit kerogen molecules of Type I, Type II, and Type III were packed in a periodic cubic simulation box with sides of length 7-nm. The workflow and the resulting initial kerogen matrix structure is shown in Figure 5.1. The representative unit structures of Type I, Type II, and Type III kerogens were taken from literature (Ungerer et al. 2014) and are shown in Figure 5.2. The Type I kerogen molecule, dominated by aliphatic carbons, corresponds to the immature lacustrine kerogen, similar to the Green River oil shale Kerogen. The Type II and Type III kerogen molecules represent middle-end oil windows and over mature kerogens, and they are dominated by aromatic carbons. The Type III kerogen molecule is more aromatic than the Type II kerogen, as is expected for a more mature humic kerogen. Further details of these unit kerogen models can be found elsewhere (Ungerer et al. 2014).

5.3 DREIDING force field

The DREIDING force field has been successfully used to model a variety of organic molecules, biological molecules, and main-group inorganic molecules. The total potential energy in the DREIDING force field consists of bonded (E_b) and nonbonded (E_{nb}) atomic interactions. The bonded atom interactions include the bond stretching (E_B), bond bending (E_A), and dihedral angle torsion (E_T), while the nonbonded interactions consist of van der Waals (E_{vdW}) and the electrostatic (E_C) contributions to the potential energy. The mathematical expression for the molecular interaction parameters (Equations 4.4 – 4.10) are already described in Chapter 4.

The bond (K_e), angle (K_θ), and torsion parameters (V) are determined by simple rule-based relations (Mayo et al. 1990). The selected kerogen molecules were initially

analyzed with the visual molecular dynamics (VMD) tool (Humphrey et al. 1996) to identify the unique number of bonds, angles, and dihedrals present in the unit kerogen structures. The VMD analysis prevents the assignment of spurious bonds and angles while developing an initial kerogen molecular configuration containing a large number of unit kerogen structures.

In the original DREIDING force field implementation, the partial atomic charges were either neglected or evaluated using the Gasteiger method (Gasteiger and Marsili 1980). In the present study, the partial atomic charges were estimated using the Gasteiger algorithm implemented in the Chimera molecular package (Pettersen et al. 2004). In the Gasteiger method, the partial atomic charges are determined by an iterative partial equalization of the orbital negativities.

5.4 Molecular simulation details

The LAMMPS package was used to perform the numerical MD simulations. The particle-particle particle-mesh (PPPM) algorithm was used to compute the electrostatic interactions between charged atoms with an accuracy of $1e^{-5}$ (relative root mean square (RMS) error in per-atom force calculation). An adaptive time-stepping algorithm was used to perform the time integration, with minimum and maximum time steps of 0.00001 and 1.0 fs. A velocity verlet algorithm was used to solve the equations of motion and to obtain the temporal position of the atoms.

Further, the high temperature of 2000 K and pressure of 1000 atm were used to anneal complex kerogen structure (which consists of a large number of, and different types of atoms). Because of the large number of atoms in each kerogen molecule and the even larger number of atoms in the simulated system, there are many molecular conformations

with energies that are not much different from that of the conformation with the lowest energy, and there is an extremely large number of configurations in the system as a whole, with energies that are very similar to that of the lowest energy configuration (on the order of k_BT higher or less, where k_B is the Boltzmann constant, and T is the absolute temperature). These low energy states are separated by energy barriers that are often substantially higher than k_BT at temperatures that are typical of hydrocarbon bearing formations in the subsurface. Hence, a series of NVT and NPT simulations (described in section 2.3.1.3) were performed to generate one of many low-energy states that are typical of the equilibrated system (Carlson 1992) and summarized in Table 5.1.

Two different sets of simulations were performed for each kerogen type to verify that the density had converged to a constant value and that the kerogen had reached an equilibrium state. The total simulation times of (0.79 ns, 1.35 ns), (0.72 ns, 1.25 ns), and (0.82 ns, 1.39 ns) were used for Type I, Type II, and Type III kerogens, respectively. The total number of simulation steps utilized in all cases was the same, but the total simulation time was different due to the utilization of adaptive time stepping. Additional simulations were performed for each kerogen type to analyze the effect of different initial simulation box sizes on the kerogen density. A periodic cubic simulation box with sides of length 5.5-nm was used to perform additional simulations. A small difference (< 3 %) was observed in the final kerogen density values.

5.5 Results and discussion

Various key molecular properties including the structural characterization, the molecular vibrational frequencies, and the heats of formation can be reproduced to validate the force field. The most routinely analyzed properties, which were evaluated in the present

study, are the kerogen density and the atomic pair distribution function between carbon atoms.

5.5.1 Kerogen density

The kerogen density depends on thermal maturity, the elemental composition of the kerogen and its molecular architecture. Figure 5.3 shows the equilibrated structures of Type I, Type II, and Type III kerogens. The gray, white, red, blue, and yellow colors represent C, H, O, N, and S atoms, respectively. From Figure 5.3, it can be seen that the aliphatic carbon along with hydrogen (high H/C ratio) dominate Type I kerogen with traces of sulfur. As the thermal maturity of kerogen increases, the overall H/C ratio decreases, due to the decomposition of the long aliphatic carbon chains and the formation of low molecular mass products with high H/C ratio, during the geochemical transformation of kerogen. Further, the sulfur content decreases as the maturity of kerogen increases.

Figure 5.4 depicts the variation of kerogen densities for Type I, Type II, and Type III kerogens at different annealing stages (temperatures and pressures). The kerogen densities at the beginning of the simulation were 0.3684, 0.3359, and 0.3381 g/cm^3 for Type I, Type II, and Type III kerogens, which were determined by knowing the total mass and the initial simulation box size of respective kerogen structures. The kerogen density remains constant during NVT simulations and changes during the NPT simulations.

Figure 5.4 shows that the kerogen density increases as kerogens become more thermally mature, resulting in the lowest density for Type I kerogens and the highest density for Type III kerogens. Further, the difference observed between Type II and Type III kerogen densities was small, which is consistent with the previous simulation study (Ungerer et al., 2014). The final kerogen densities obtained for Type I, Type II, and Type

III kerogens after equilibration were 0.71, 0.84, and 0.89 g/cm^3, respectively. Table 5.2 summarizes kerogen densities from the literature and provides a comparison with the present study. The kerogen densities obtained in the present study are lower than the simulation and experimental kerogen densities reported in the literature.

The primary reason for the underprediction in the kerogen densities is the generalized nature of the DREIDING force field that has a tendency to underpredict density values (Nakamura et al. 1993; Wu and Xu 2006). There are additional factors that also affect the kerogen densities which include:

1. the existence of the free volume and the intrinsic subnanometer scale porosity within kerogen matrix,

2. the lack of cross-linking between unit kerogen molecules,

3. the generalized nature of the DREIDING forcefield, and

4. incomplete equilibration during the annealing simulations.

The following sections provide a detailed description of these factors.

5.5.1.1 The existence of the free volume and intrinsic subnanometer scale porosity within the kerogen matrix

A kerogen matrix consists of cross-linked aliphatic and aromatic carbon chains that form a complex polymeric structure. During the thermal maturation process, kerogen is exposed to temperatures and pressures that are high, relative to surface temperatures and pressures. In particular, the elevated temperature enables extensive chemical transformation to occur on geological time scales. During this process, the functional groups rearrange themselves to reduce the system free energy, as the temperature, pressure, and chemical environment change. Because of the constraints imposed by chemical

bonding, molecular rigidity, and complex molecular shapes, kerogen molecules cannot pack together without small voids remaining. These voids, frequently referred to as free volume or intrinsic porosity in polymers (Budd et al. 2005), play an important role in the sorption and transport of small molecules in kerogens. The intrinsic porosity within a kerogen matrix may be continuous, intermittently connected, or completely isolated, thus affecting the retention of hydrocarbons in a kerogen and their release during hydrocarbon production. This intrinsic porosity is on a much smaller scale than the nanoscale porosity often seen in focused ion beam-scanning electron microscopy (FIB-SEM) images of high maturity kerogen, Therefore, small molecule – kerogen interactions are expected to have a strong influence on this extremely small scale "porosity." The percent of intrinsic porosity depends on the thermal maturity of the kerogen, the kerogen molecular structure, and the overall kerogen molecular rigidity (McKeown and Budd 2010).

A preliminary analysis was performed to characterize the intrinsic porosity and improve understanding of the subnanometer scale features within the kerogen matrix. The equilibrated kerogen matrix structures were virtually sliced, using the VMD tool to obtain a series of 2D cross-sections of kerogen matrix with a slice thickness of 5 Å. The 2D images were analyzed with ImageJ (Abràmoff et al. 2004), revealing the internal kerogen matrix structure shown in Figure 5.5. The white and dark portion represents the kerogen and intrinsic porosity, respectively. The overall dimensions of each kerogen matrix (which contains both kerogen and intrinsic porosity) is approximately 5-nm × 5-nm. It can be seen that a significant number of subnanometer scale pores exist within the kerogen matrix, which can act as nano-reservoirs that retain hydrocarbons and other fluids. Although a direct relationship between the subnanometer scale porosity and the thermal maturity of

kerogen is not established at this stage, the analysis provides an insight into subnanometer scale features within kerogen matrices, which cannot be investigated using currently available experimental methods, including Transmission Electron Microscopy (TEM) or even Scanning Electron Microscopy (SEM), because they are unable to resolve the subnanometer scale features within kerogen matrices. In addition, kerogen isolation from the source rock is a complex process that may alter the kerogen structure.

Focused ion beam and broad ion beam milling are frequently used to prepare "flat" surfaces and thin specimens for high-resolution imaging, but even these "gentle" methods may cause severe damage on the subnanometer scale. Presently, we believe that the existence of intrinsic porosity affects the predicted kerogen densities, and higher kerogen densities can be expected, if intrinsic porosity is reduced by annealing for a longer time.

5.5.1.2 The lack of cross-linking between unit kerogen molecules

Because they are not soluble in nonreactive solvents, it is not possible to determine the molecular mass distribution of kerogens. However, it is very likely that these geopolymers have extremely high molecular masses, and that they consist of highly cross-linked molecular networks, similar to elastomers in a glassy or rubbery state. In the work described here, we did not consider crosslinking between unit kerogen molecules, which results in comparatively small molecular masses. It has been observed that the long carbon chains help to increase the coal density (Carlson 1992), and hence, the lack of cross-linking between kerogen molecules may be one of the reasons why the kerogen densities predicted by molecular dynamics with the DREIDING force field are lower than experimental kerogen densities.

The inclusion of cross-linking between unit kerogen molecules would result in a

more accurate prediction of the kerogen densities. A detailed investigation is required to determine the cross-linking mechanism between kerogen molecules, to analyze the effect of the kerogen maturity on the cross-link density, and the distribution of various types of cross-links and their effects on kerogen stiffness.

5.5.1.3 The generalized nature of the DREIDING force field

The DREIDING force field is a general-purpose force field that can be used for any organic molecule and main-group of inorganic molecules. The parameterization of the force field is based on simple hybridization rules and does not depend on the particular combination of atom types, e.g., the bond stiffness constant is the same irrespective of the combination of atoms. As a result, the properties evaluated with the DREIDING force field may differ from their actual values. Various studies (Hu et al. 2010; Wu and Xu 2006) have compared the performance of the DREIDING force field and found that the DREIDING force field underpredicts the material densities (epoxy resin and coal density) owing to the generalized nature of the force field.

5.5.1.4 Incomplete annealing

In these and other molecular dynamics simulation that aim to simulate kerogen under equilibrium conditions, the system is quenched from a high temperature to the purported equilibrium state on a timescale on the order of 10^{-8} s at most, and the rate of temperature change is on the order of 10^{11} K/s^{-1}. This is $\geq 10^6$ times the critical quench rates needed to form mixed-metal glasses. At these fast quench rates, it is unlikely that annealing is complete, particularly for large complex molecules of low flexibility. The challenge of annealing large kerogen molecules is similar to the problem of protein folding.

While some small proteins fold over time scales of 10^{-6} –10^{-4} s (very long for all-atom molecular dynamics simulations), the folding times for large proteins may be very much longer. In practice it is difficult to determine when the equilibrium density has been reached. Kerogen is formed via a long sequence of chemical transformations that occur on time scales of up to $\approx 10^{16}$ s, and while molecular dynamics with reactive force fields might better represent this process in principle, it is not practical under the (P, T) conditions encountered in hydrocarbon bearing formations, because of the high reaction activation energies. All molecular dynamics simulations are faced with these challenges, which are exacerbated by the very small time steps required for accurate integration.

5.5.2 Carbon-carbon pairwise distribution function

The atomic pairwise distribution function, g (r), is the probability of finding atoms at a given radial distance from the reference atoms. The pairwise distribution function provides local and average structural information (Petkov et al. 2013) about kerogen that can be used to characterize the structural evolution of kerogen, during geological transformation or to compare different representative kerogen structures.

Figure 5.6 shows the overall carbon-carbon pairwise distribution function for different equilibrated kerogen structures considered in the present analysis and the detailed carbon-carbon pairwise distribution function between 1-Å and 2-Å. The well-defined peaks reveal the dominance of aliphatic or aromatic carbon in a given kerogen structure. In particular, the first and second peak of g (r), observed at distances 1.39-Å and 1.54-Å, corresponds to the aromatic carbon (with the shorter bond length) and the aliphatic carbon (with the longer bond length). Figure 5.6 confirms that the Type I kerogen is dominated by aliphatic carbon, since the magnitude of the peak in g (r), corresponding to aliphatic carbon,
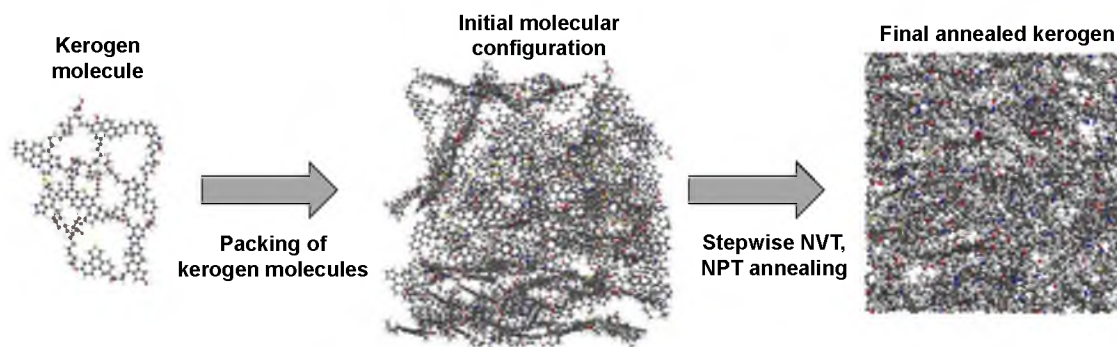
is greater than the magnitude of the peak corresponding to aromatic carbon. Further, the magnitude of the aromatic carbon increases as the thermal maturity of the kerogen increases.

Finally, the pairwise distribution function beyond 2.0-$\mathring{A}$ corresponds to the carbon atoms which are not directly bonded to each other. Overall, the carbon-carbon pair distribution function is consistent with the results reported in the literature (Orendt et al. 2013; Ungerer et al. 2014).

In summary, molecular dynamics simulations were performed to evaluate the capability of the general-purpose DREIDING force field to model and simulate representative kerogen structures, having the variable thermal maturity and elemental composition. The kerogen density and pairwise distribution functions are determined by molecular dynamics simulations and are compared with the experimental and simulation results available in the literature. Kerogen density increases with increasing thermal maturity. The kerogen densities were under-predicted by molecular dynamics simulations, using DREIDING force field for all kerogen models, due to the existence of subnanometer-scale intrinsic porosity within the kerogen matrix, the lack of cross-linking between kerogen molecules, the generalized nature of the force field, and by incomplete annealing. The pair distribution function obtained for all kerogen models was consistent with the results from the literature.

The present study shows that the general-purpose DREIDING force field can be used to simulate the complex kerogen matrix, where little or no experimental data is available. Further, the outcomes from the present study can be coupled with modern CPU and GPU-based high-performance computational capabilities to simulate the larger and

more complex kerogen models that will help in the better understanding of the kerogen structure, which is crucial in supercritical carbon dioxide enabled hydrocarbon recovery processes in unconventional reservoirs.

Kerogen molecule

Initial molecular configuration

Final annealed kerogen

Packing of kerogen molecules

Stepwise NVT, NPT annealing

FIGURE 5.1 The workflow to develop a realistic kerogen matrix structure
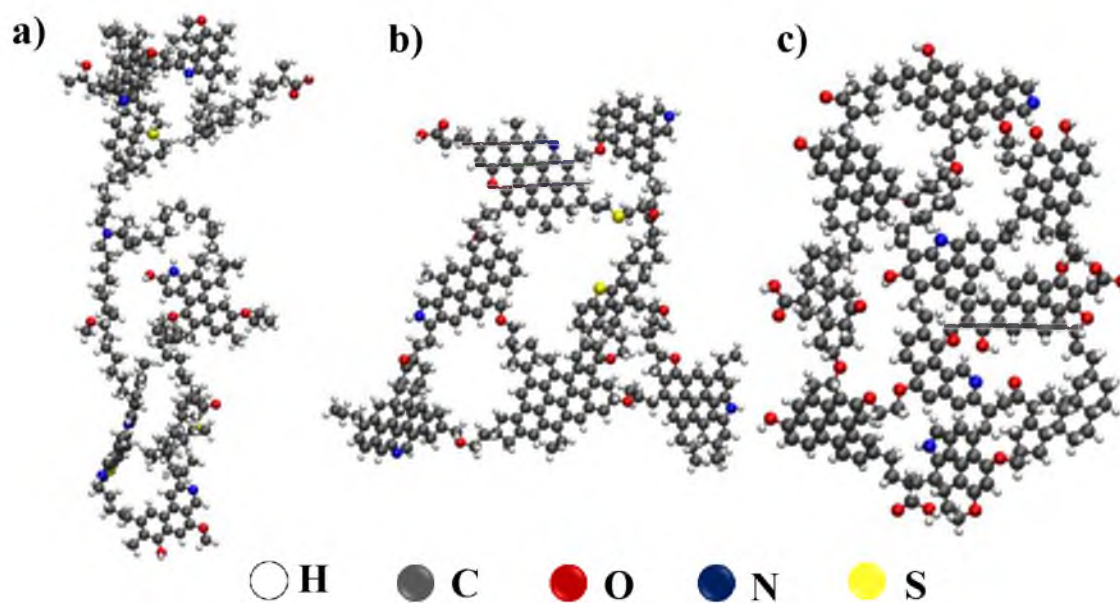
FIGURE 5.2 Different kerogen types a) Type I (immature Green River shale kerogen), b) Type II (middle-end oil window kerogen), and c) Type III (matured kerogen) "Reprinted (adapted) with permission from (Ungerer 2015). Copyright 2015 American Chemical Society"
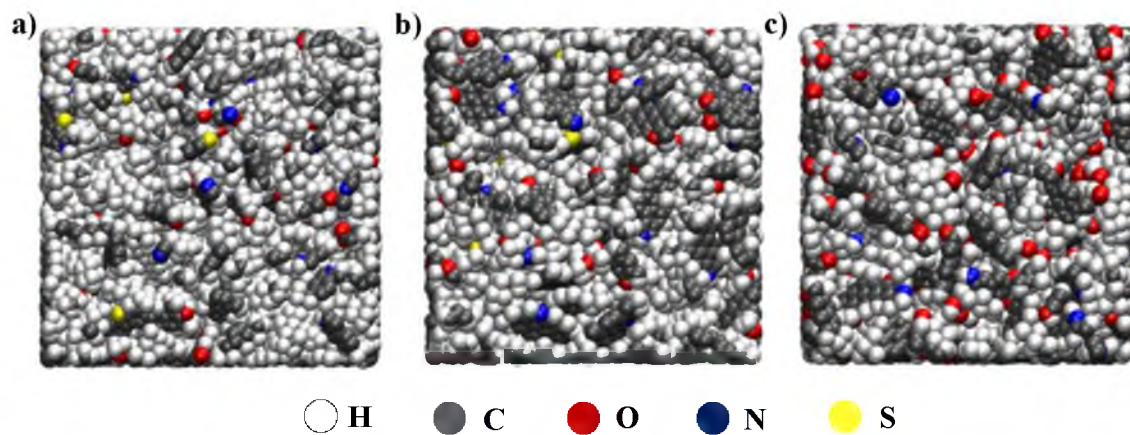
FIGURE 5.3 Annealed a) Type I, b) Type II, and c) Type III kerogen structures
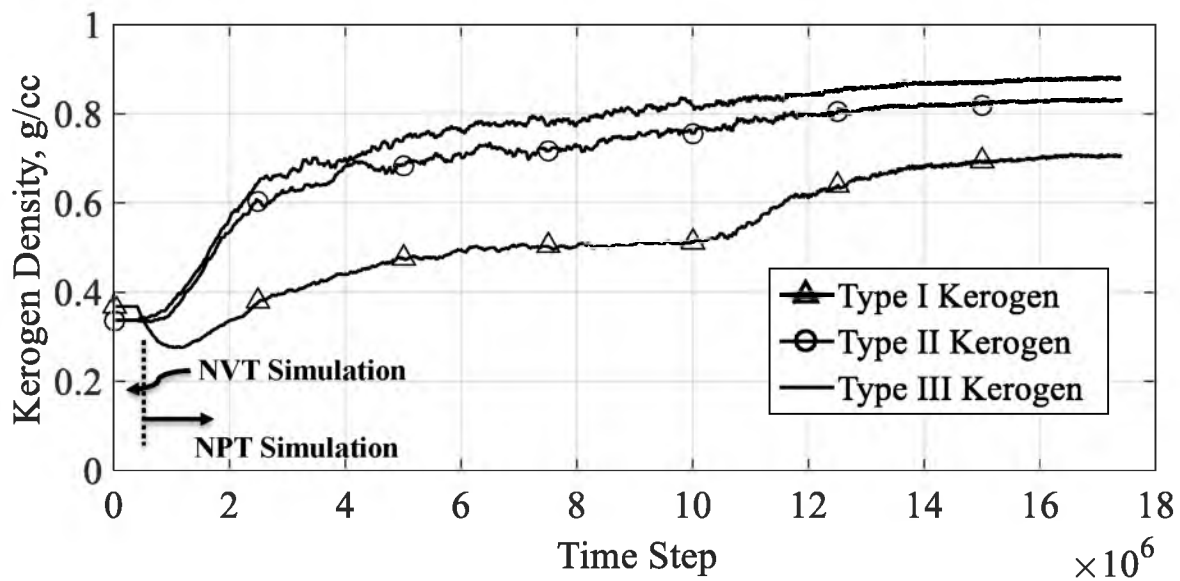
FIGURE 5.4 Kerogen density variation during different annealing stages
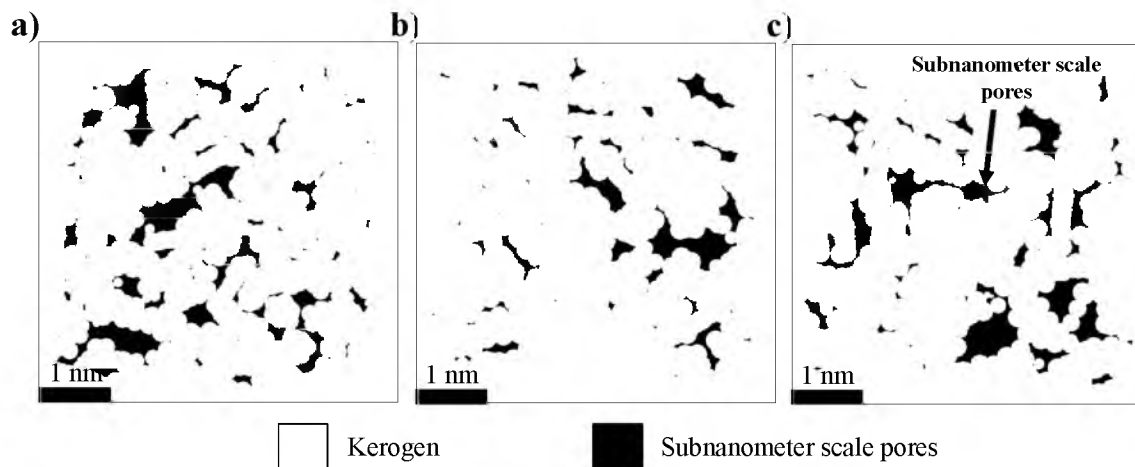
FIGURE 5.5 Intrinsic subnanometer scale porosity in a) Type I, b) Type II, and c) Type III kerogen matrices
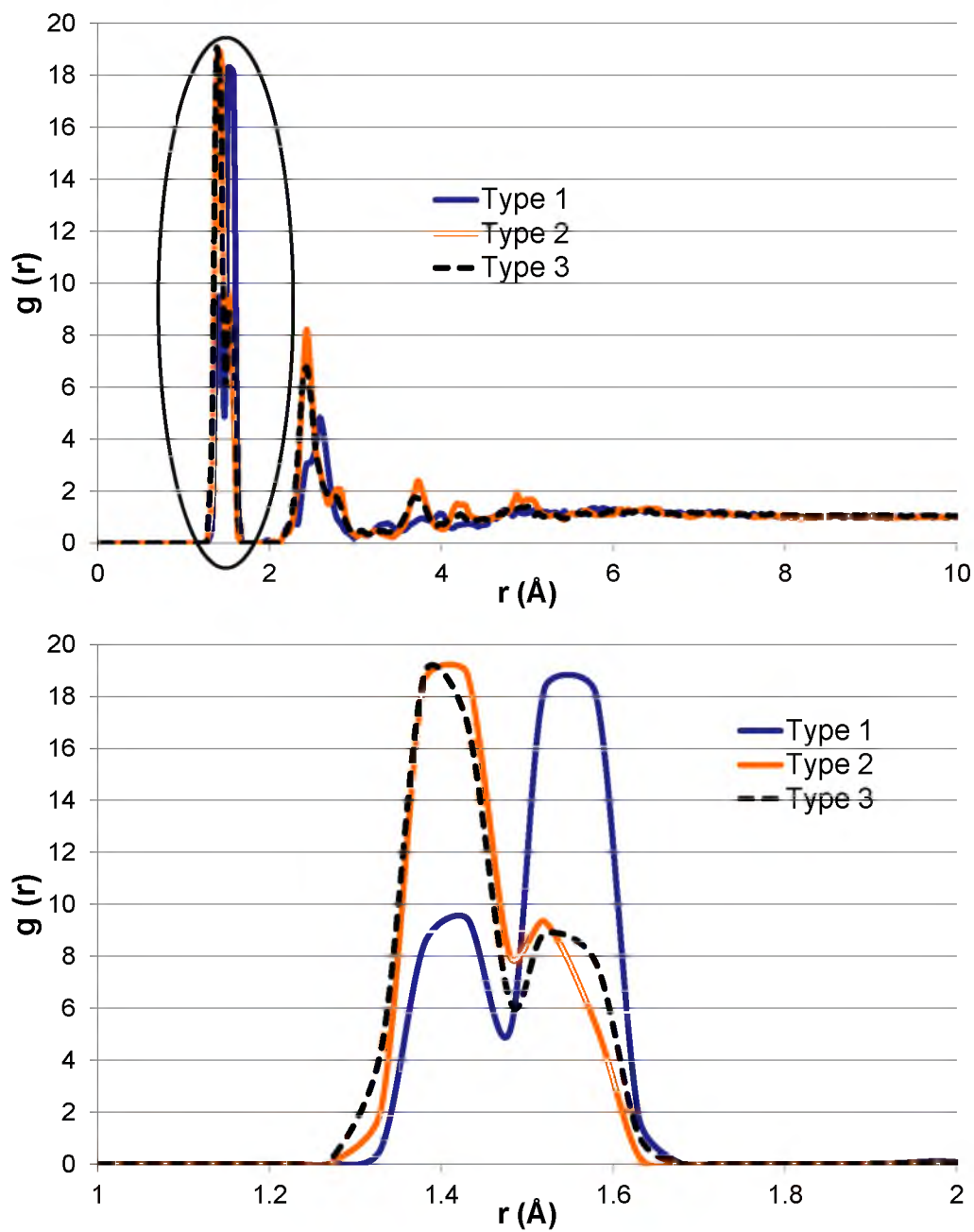
FIGURE 5.6 The overall carbon-carbon atomic pairwise distribution function and the carbon-carbon atomic pairwise distribution between 1 Å and 2 Å

TABLE 5.1 Kerogen annealing stages

Annealing sequence	Ensemble	P (atm)/ T (K)	Number of steps		
			Type I kerogen	Type II kerogen	Type III kerogen
1	NVT	300 – 2000 K	400,000	400,000	400,000
2	NPT	1000 atm, 2000 K	70,00,000	70,00,000	70,00,000
3	NPT	100 atm, 1000 K	30,00,000	30,00,000	30,00,000
4	NPT	10 atm, 500 K	30,00,000	30,00,000	30,00,000
5	NPT	1 atm, 300 K	46,00,000	46,00,000	46,00,000

TABLE 5.2 Comparison of kerogen densities

	Kerogen Type		
	Type I	**Type II**	**Type III**
Experimental	0.95 (Facelli 2011)	1.18-1.25 (Okiongbo et al. 2005) 1.18-1.22 (Stankiewicz et al. 1994)	1.25 (Jiménez et al. 1998)
Simulation	1.00 (Ungerer et al. 2015) 0.66 (Liu et al. 2015) 0.90 (Facelli 2011)	1.13-1.28 (Ungerer et al. 2015)	1.16-1.20 (Ungerer et al. 2014)
Present work	0.71	0.84	0.89

CHAPTER 6

THE MULTIPHASE SIMULATION IN REALISTIC

NANOMETER AND SUBNANOMETER PORES

FOUND IN KEROGEN MATRIX

6.1 Introduction

A significant research effort characterizing various aspects of shale reservoirs manifest the potential of shale gas as the one of the vital energy sources, which constitute the major fraction of the total natural gas used in the United States. Despite the enormous potential of shale resources, the lower hydrocarbon recovery rate is one of the major factors hindering the economic development of shale reservoirs. This is mainly due to the complex, heterogeneous, nanoporous structure of shales having a permeability of the order of nano-darcy, the existence of poorly connected pore networks, the presence of the multiscale mineralogical and structural heterogeneity, the random distribution of organic matter throughout the reservoir matrix, and the limited application of the Darcy's law describing the fluid transport in the nanostructures shales. Further, the fluid flow in shales is controlled by more than one factor — the pore size distribution, the pore connectivity, the pore composition, the pore surface anisotropy, the pore injection pressure, and the pore temperature — altogether coupled with the pore confinement effects, making the fluid flow modeling and simulation in shales a challenging task. As a result, various hydrocarbon migration and storage mechanisms in shale are not fully comprehended.

Numerous attempts (Falk et al. 2015; Hu et al. 2015; Javadpour et al. 2007) have been made to reduce the gap in the present understanding of the nanoscale multiphase fluid transport, but mostly pure carbon-based/activated carbon-based systems were used to define the organic matter — which is one of the most important component of shales and the source of hydrocarbons. However, in reality, the kerogen structure is complex; it consists of long aliphatic and aromatic carbon chains, and has a varying elemental composition — the presence of C, H, N, O, and S atoms that define the oxygen and hydrogen indices — depending on the type and the thermal maturity of kerogen.

Further, most of the studies performed in the literature focused on the fluid transport in the perfectly cylindrical nanopores. However, in practice, as described by numerous shale petrophysical characterization studies (Ahmad and Haghighi 2012; Loucks et al. 2009), the pores observed in organic matter are not perfectly cylindrical, and they deviate from the ideal to a more irregular pore size and shape. One of the main reasons for the observed irregularity in pore sizes and shapes is the fundamental arrangement of the atomic structure/functional groups of the organic and the inorganic matter, during the geo-thermal transformation of shales. As a result, the realistic pore structures exhibit features such as heterogeneous and irregular pore surfaces, which affect the underlying fluid transport, the fluid storage, and the fluid migration. Thus, it is imperative to model and simulate a multiphase flow transport in a realistic kerogen pore structure enabling a more accurate characterization of the nanoscale fluid transport in shales.

A molecular dynamics (MD) simulation approach is used in the present chapter to model and to investigate the multiphase flow of liquid-gas (water-methane) transport in methane saturated pores with open and closed (pore with a dead end) configurations found

in an organic matrix. The pore sizes of 0.8 and 5-nm (subnanometer and nanometer size) were used, and the impact of an external driving force applied to water and the effects of the pore system temperature was investigated based on the dynamics of the methane molecules in the confined system.

6.2 The development of a molecular model of a nanopore found a kerogen matrix

(Dow 1977) described a kerogen as the portion of organic matter in sedimentary rocks which is insoluble in organic solvents. The kerogen is distributed randomly throughout the reservoir matrix, and the total organic content varies from the reservoir to reservoir, which determines the quality and the quantity of hydrocarbons generated, based on the kerogen concentration, the kerogen type, and the thermal maturity of kerogen. The structural characterization of the kerogen shows that the nanoporous kerogen structure consists of the mixture of the well-connected, the partially-connected, or the completely isolated pores, where the pore diameters vary from a few angstroms to a micrometer.

Thus, considering the complexities of the kerogen structure, the development of the molecular model of a nanopore structure found in a kerogen matrix is not a straight forward task and requires a significant optimization of MD simulation parameters at various stages of the model development process. The key considerations in the kerogen model development are summarized in the subsequent paragraphs.

First, kerogen is differentiated into various types based on the Van Krevelen diagram (Van Krevelen 1984) based on a biological precursor of kerogen, and the thermo-geo-chemical transformation of the kerogen over the geological timescale, and the thermal maturity of kerogen. The replication of the kerogen evolution procedure, which occurs over

a significant amount of time, is nearly impossible with an MD simulation (where most of the simulations are carried on the time scale of a few nanoseconds), and thus requires simplifying assumptions.

Most of the experimental kerogen characterization studies provide the average kerogen structure corresponding to the specific geological time/thermal maturity of the kerogen, which can be used as a reasonable initial molecular configuration of the kerogen required for the MD simulations. Very few 3D kerogen models are available in the literature where the typical size of an unit kerogen structure is less than a nanometer. Hence, a large number of such 3D kerogen structures are required to develop an average representative kerogen structure.

Second, while developing an initial molecular configuration of kerogen (the first stage of MD simulations), a large number of unit kerogen molecules are loosely packed in a simulation box with predefined dimensions. The dimensions of the simulation box should be optimized to minimize the higher computational time required to equilibrate the large simulation box and to avoid the overlap between atoms.

Third, the annealing (the equilibration) of the kerogen structure is a complex process and requires optimization of many simulation parameters, including the simulation time step, the total simulation time, and the cut-off distance of long-range atomic interactions. This is due to the complex and heterogeneous kerogen structure that consists of C, H, O, N, and S atoms and the difference in the fundamental atomic properties, such as atomic masses and the partial atomic charges.

Fourth, the pore structure can be modeled as a rigid pore (as in the case of the present research) or a flexible pore (where the organic matrix surrounding the pore is

allowed to deform during the simulation). For rigid pores, it is important to maintain the pore structural integrity during the kerogen equilibration process to avoid the pore collapse and the expulsion of reservoir fluids. This can be achieved by the stepwise annealing process where the kerogen structure is equilibrated first, excluding the reservoir fluids from the time integration, and following a similar procedure to equilibrate the reservoir fluids. Also, the kerogen structure can be excluded from the production simulation run if the pore is rigid and only the properties of the fluids are of interest. This will help to minimize the computational cost of the simulation.

Fifth, the force applied to water molecules is important as the water molecules in small pores displaces relatively faster than the larger pores for the same applied force.

Finally, the pore surfaces are not regular and exhibit surface anisotropy, which results in small voids on the pore surface, thus making the pore surface discontinuous. For the organic matrix with subnanometer pores, the surface discontinuity is less and increases with an increase in the pore diameter. The primary reason for this observation is the atomic arrangement during the equilibration process. For an organic matrix with subnanometer pores, the simulation box is like a perfect cube where atoms can be exchanged easily on the periodic boundaries of the simulation box, during high pressure and temperature annealing. On the other hand, for the larger pore sizes, the atoms prefer to remain near the pore surface, and atoms are not exchanged easily on the periodic boundaries, resulting in a discontinuous pore surface.

After implementing the above-defined consideration, initial molecular configurations of a kerogen matrix with nanopore is developed for both open-pore configurations and the closed-pore configuration. A total of two pore sizes are used,

including 0.8-nm and 5-nm. The numbers of kerogen, water, and methane molecules utilized in each configuration are summarized in Table 6.1. Figure 6.1 shows the graphical representation of various pore configurations used for the present study.

6.3 Molecular simulation details

The three-stage MD simulation workflow proposed in Chapter 4 is used, and only the parameters relevant to multiphase flow simulation in kerogen are summarized here. The LAMMMPS simulation package is used to perform the MD simulations. The general-purpose DREIDING force field is used to characterize the bonded and nonbonded interactions between kerogen molecules; the SPC/E water model is used to simulate water molecules, whereas the methane is simulated as independent rigid bodies. The standard velocity Verlet algorithm is used to solve the equations of motion. The particle-particle particle-particle mesh algorithm is used to calculate the electrostatic interactions with a cut-off distance of 10 Å. The Nose-hover thermostat is used to maintain the system at the desired temperature. The atomic trajectories were stored every 1,000 time steps and used to evaluate the dynamic fluid properties of water and methane and is summarized in the next section.

6.4 Results and discussion

A qualitative and quantitative assessment of water and methane transport properties in nanometer and subnanometer size pores found in a kerogen matrix is performed. In particular, the impact of various pore scale attributes — summarized in Section 2.3 — on the water and methane diffusion and on methane number density (methane distribution within the nanopores) are analyzed and described in the following sections.

6.4.1 Qualitative comparison

6.4.1.1 The impact of the force applied to water molecules

Figure 6.2 shows the water and methane behavior in 0.8-nm diameter pores found in a kerogen matrix. Part a) of Figure 6.2 represents the positions of water and methane molecules at the beginning of the simulation while parts b) through d) of Figure 6.2 depict the final positions of water and methane molecules for 0, 0.05, and 0.1 Kcal/mol-Å forces applied to each atom of water molecules.

At a force of 0 Kcal/mol-Å, there is no significant displacement observed for water and methane molecules. The displacement of water and methane increases with an increase in the force applied to the water molecules. The displacement of water and methane in subnanometer pores is limited primarily by two factors: the extremely high surface forces in subnanometer pores and the surface anisotropy. The surface forces compete with the externally applied forces to water molecules, and thus, significantly high force on water molecules are required to overcome the surface forces. Further, the surface anisotropy results in either in the voids or the obstructions in the pore surface that affect the flow of water and the number of water molecules reaching to the methane molecules.

The above-defined observations have various implications on the fluid transport in subnanometer scale pores. First, the results depicted in Figure 6.2 show the existence of a threshold force limit (depending on the pore size and pore composition) that needs to be overcome before inducing a noticeable displacement in injected reservoir fluid (water in this case). Second, the injected reservoir fluids and the displaced hydrocarbons (e.g., methane) will remain trapped inside the subnanometer pores until the resultant force is below the threshold value.

Also, the state of hydrocarbons (free, adsorbed, or absorbed forms) cannot be defined accurately in subnanometer size pores due to the pore size, which affects fluid transport in all directions.

Figure 6.3 depicts the water and methane transport in a 5-nm kerogen pore. Part a) of Figure 6.3 depicts the initial position of the water and methane molecules in a 5- nm pore, while part b) through d) of Figure 6.3 shows the final positions of water and methane molecules for various applied forces to water molecules.

The behavior of water and methane in a 5-nm pore is different from the 0.8-nm pore in various aspects. First, the free methane and methane in other forms (adsorbed and diffused) within the pore can be distinguished easily. Second, the water molecules can reach the methane molecules and displace them in the axial direction of the pore as the force applied to water molecules increases. Only the water molecules near to the pore surface are retained on the pore wall (suggesting possible water adsorption on the pore surface and give an idea about the possible water loss during the hydrocarbon recovery process), while the water molecules away from the pore are mainly responsible for the methane displacement. Also, at zero applied force (shown in Figure 6.3b), the methane molecules are mainly diffused in the kerogen matrix. On the other hand, the methane molecules preferred to remain within the pore for higher applied forces to water molecules. This is potentially due to the minimum time available for diffusion of methane molecules into the kerogen matrix before water molecules come in the contact with the methane molecules in response to the higher forces applied to water molecules.

For the closed pore, similar kinds of observations can be made for 0.8-nm and 5-nm diameter pores, except for the following differences. The water and methane molecules

are subjected to additional long-range interaction forces due to the presence of the pore surface on the exit side of the pore. Also, a high surface anisotropy exists near the entrance of the pore due to the molecular arrangements during the kerogen equilibration. As a result, there exists a larger size cavity near the entrance of the pore affecting the displacements and the dynamic properties of water and methane molecules. As a result, the water molecules are not able to reach the closed end of the 5-nm pore, whereas water and methane are diffusing in the available conduits of a size equal to or greater than molecules at the closed end of the 0. 8-nm pore.

The major difference in the hydrocarbon recovery between subnanometer and nanometer pores is that few molecules are displaced in subnanometer-sized pores as a result of the pore size and pore anisotropy, resulting in a comparatively lower recovery from these pores. On the other hand, for the larger pores, the comparatively large number of methane molecules reaches to the end, enhancing the recovery rates.

Also, both the open pore and closed pore configurations retain water and methane molecules on the pore surface, and some molecules are absorbed in the organic matrix, resulting in a simultaneous adsorption and diffusion in the kerogen matrix.

6.4.1.2 The impact of the pore system temperature

Figures 6.4 and 6.5 show the effect of temperature on water and methane behavior in the 0.8 and 5-nm pores at 0 Kcal/mol-Å force applied to water molecules. The 0 Kcal/mol-Å is selected for the analysis to exclude the contribution of the applied force on the displacements of water and methane molecules. Three different temperatures of 300 K, 325 K, and 340 K, were used for the analysis. Figure 6.4 shows that the mobility of water and methane increases with the rise in the pore system temperature and results in a

displacement of molecules towards the pore surface and into the kerogen matrix. A similar observation can be made for the 5-nm diameter pore, which is more distinguishable. Further, the increased temperature results in frequent collisions of water and methane molecules with the pore wall, especially for the 0.8-nm diameter pore.

6.4.1.3 The impact of the pore diameter on the fluid flow

From the analysis presented in the previous sections (in Figures 6.2 through 6.5), the overall impact of the pore size on the water and methane displacements in pores of 0.8-nm and 5-nm diameters is summarized here to analyze the effect of pore size. It is observed that the water and methane confined in pores are subjected to very high surface forces, where the effect of the surface forces on fluid molecules decreases as the distance between fluid molecules and pore wall increases. For the 0.8-nm pore, the confined fluids are subjected to high surface forces at all locations within the pore, due to the comparable dimensions of fluid molecules and the pore size. For larger pores, e.g., 5-nm pore, the effect of surface forces is high around the pore surface and decreases towards the pore center. This is the main reason for the observation of the retention of the fluid molecules near the pore wall and transport of only the molecules at the center of the pore, which are primarily responsible for the methane recovery.

6.4.2 The quantitative comparison

The mean square displacements of water and methane molecules, the number density of methane molecules, and the effective diffusion coefficients of water and methane were determined for the 0.8-nm and 5-nm diameter open and closed pores at different pore system temperatures. The important observations are summarized in the following

sections.

6.4.2.1 The mean square displacements of water and methane

Figures 6.6 through 6.9 show the mean square displacement (MSD) of water and methane molecules in 0.8-nm and 5-nm open and closed pores, respectively, at various forces applied to water molecules and at different system temperatures. From Figures 6.6 and 6.8, it can be seen that the MSDs of water and methane in 0.8-nm size pores (subnanometer pores) are chaotic and do not show any obvious correlation. The primary reason for this observation is the comparable sizes of the fluid molecules and the actual pore size, which results in frequent collisions of fluid molecules with the pore wall. Further, the MSDs of water molecules in 0.8-nm diameter open and closed pores are more chaotic than those of methane, due to the additional contribution of the forces applied to the water molecules. Also, the chaotic behavior of fluid molecules increases with the increase in system temperature. Further, the MSDs of methane, which is a gas, are higher than the water molecules in all simulation cases. At 0 Kcal/mol-Å applied force, the difference between MSDs in a 5-nm pore at various temperatures is very small.

6.4.2.2 The methane number density

The methane number density in nanometer and subnanometer pores represents the distribution (concentration) of methane molecules at different regions in the radial direction from the pore center. Figures 6.10 – 6.13 show the variation of methane number density for 0.8-nm and 5-nm open and closed pores at various forces applied to water molecules and the different system temperatures. Labels t_1 and t_2 represent the initial and the final times where methane number densities are recorded. Note that times t_1 and t_2 are not same

due to the utilization of the adaptive time stepping. Table 6.2 summarizes t_1 and t_2 for different simulation cases.

From Figures 6.10 and 6.12, it can be seen that the methane molecules are concentrated around the pore center at the beginning of the simulation in the 0.8-nm diameter pore due to the small pore size, thus representing a layered distribution of water and methane molecules. With the increase in the simulation time, methane molecules move close to the pore surface and in the kerogen matrix and they are evident with small tails observed in the number density curves. Further, various trends in the methane number density are observed for the 0.8 diameters including methane concentrated on the pore surfaces, methane concentration only on the one side of the pore surface, and at methane concentration at the center of the pore. This is due to the coupled effect of the pore size, the pore composition, the pore system temperature, and the force applied to water molecules.

As the pore diameter increases, the molecules are distributed almost evenly in the pore (except at the pore surface) due to the comparatively large size of the pore. Also, the number densities shown in Figures 6.10 through 6.13 are not symmetric, which means the mobility of atoms is not symmetrical and potentially affected by an initial molecular distribution or the affinity of the one type of molecule(s) towards another type of molecules from kerogen.

6.4.2.3 The effective diffusion coefficient in nanometer and subnanometer pores

Figures 6.14 and 6.15 depict the variation of the effective diffusion coefficients of water and methane in open and closed pore configurations at different system temperatures. The effective diffusion coefficients are evaluated from the mean square displacement at 0

Kcal/mol-Å. As previously described, the mean square displacements in 0.8-nm pores are chaotic. Thus, the evaluation of the diffusion coefficient from such complicated behavior needs to be done carefully. A statistical approach is used to accomplish this task. Mean square displacements are selected at sufficiently long simulation times such that the standard deviation of the mean square displacement is less than three times the standard deviation of the sample analyzed. Tables 6.3 through 6.6 provide a brief summary of the diffusion coefficient along with the standard deviation of the mean square displacements.

From Figure 6.14, it can be observed that the effective diffusion coefficient of both water and methane are low in 0.8-nm and increases as the pore diameter increases. Further, the diffusion coefficient of methane is higher than the diffusion coefficient of water, due to the higher mobility of methane (gas) molecules as compared to water (liquid) molecules. Also, as the temperature of the system increases, the effective diffusion coefficients of water and methane increase. The rate at which the diffusion coefficient increases are higher than the rate of increase of diffusion coefficient of water.

For the closed pore shown in Figure 6.15, the diffusion coefficients of water and methane are higher than the open pore, due to the additional long-range interactions between water and methane and the closed pore wall.

6.5 GPU implementation of molecular dynamics simulations

The development of an initial molecular configuration is the least computationally expensive task and can be completed on a regular CPU-based workstation. However, the solution of the equations of motion requires a significant amount of computational resources. Thus, a high-performance massively parallel computing is necessary. The utility of the graphics processing units (GPUs) is shown to model a water-methane-quartz system

(similar to the system presented in Chapter 4). A total of 1285 water molecules, 191 methane molecules, and 5337 quartz molecules were used, and the computational performance of GPUs were compared for 10,000 time steps.

The NVIDIA 2090 GPU architecture was used, where the number of GPU nodes varied from 1 to 6 (2 GPUs/node). The total computational time for each test case is determined and plotted, and shown in Figure 6.16. As expected, the total computational time decreases with an increase in the number of nodes (total number of GPUs). Further, the total computational time for six nodes is comparatively higher than the five nodes. The observed nonlinearity may be due to the increased communication time between GPUs.

Further, the computational speedup is also compared with a different number of GPUs. The computational times of NVIDIA 2090 GPU architecture and the Intel Xeon (Sandybridge E5-2670) node were used for the comparison. Figure 6.17 depicts the computational speedup achieved for a different number of GPUs. It can be seen that the maximum computational speedup of 4 is achieved with 5 GPU nodes. The present analysis was restricted up to 6 available GPU nodes but can be extended further to achieve the similar computational speedup reported in the literature review.

6.6 Dissipative particle dynamics (DPD) simulation method

Due to the slow evolving processes in shale reservoirs, the traditional MD method can not be used to simulate the fluid flow for more than a few nanoseconds, due to the computational requirements. Thus, a dissipative particle dynamics (DPD) simulation technique, which is a type of coarse-grained simulation technique, is a suitable choice that can bridge the gap between the traditional molecular dynamics simulations and the continuum simulations, thus providing an opportunity to model the transport processes in

shale reservoirs for the longer length and time scales. As the hydrodynamics of the fluids confined in nanopore and subnanometer-sized pores found in organic and inorganic matrices is less studied, the upscaling of all-atom molecular models is a challenging task — but has significant potential — and requires a step-by-step approach, as summarized in the literature review. Presently, the DPD analysis is limited to explore the behavior of water confined in a quartz nanopore.

Before providing the details of the DPD model of water confined in a quartz nanopore, a brief introduction to the DPD method is presented. Additional details of the DPD method can be found elsewhere (Groot and Warren 1997).

6.6.1 The DPD formulation

In the DPD method, Newton's laws are used to describe the motion of the particles and the total force acting on a particle "i" is given as,

$$\frac{dv_i}{dt} = f_i = f_i^{int} + f_i^{ext} \tag{6.1}$$

where f_i^{ext} is the external force acting on a particle, e.g., the gravitational force, while f_i^{int} is the internal force particle acting on the particle (Liu et al. 2007). The total internal force consists of three components and is given by Equation 6.2:

$$f_i^{int} = \sum_{i \neq j} F_{ij} = F_{ij}^C + F_{ij}^D + F_{ij}^R \tag{6.2}$$

where, F_{ij}^C is the conservative force due to the soft interactions along the line of particle centers, F_{ij}^D is the dissipative force that characterizes the effect of viscosity, and F_{ij}^R is the

random force due to the thermal fluctuations of the particles. The mathematical expression for the conservative, dissipative, and random forces are given by Equations 6.3 – 6.5,

$$F_{ij}^C = a_{ij} w^C(r) \hat{r}_{ij} \tag{6.3}$$

$$F_{ij}^D = -Y w^D(r_{ij})(\hat{r}_{ij}.v_{ij})\hat{r}_{ij} \tag{6.4}$$

$$F_{ij}^R = \sigma w^R(r_{ij})(r_{ij})\xi_{ij}\hat{r}_{ij} \tag{6.5}$$

where a_{ij} is the maximum repulsion between particles, Y is the viscosity coefficient, σ is the coefficient for the repulsive force, and w^C, w^D, and w^R are the weight functions for the conservative, dissipative, and the repulsive forces. Further, the relation between different coefficients described above can be given as,

$$w^D(r) = [w^R(r)]^2 \tag{6.6}$$

and

$$Y = \frac{\sigma^2}{2k_B T} \tag{6.7}$$

where, k_B is the Boltzmann constant and all interaction energies are expressed in terms of $k_B T$.

6.6.2 MD and DPD simulation of water confined in a quartz nanopores

An MD simulation of the water confined in a quartz nanopore is performed to obtain the mean square displacement and the diffusion coefficient of water molecules that can be used to calibrate the DPD simulation parameters. The interatomic potential parameters described in Chapter 4 were used to simulate the water-quartz system. A total of 1000 water molecules, and the total simulation time of 16.7 ps with adaptive time stepping algorithm were used. LAMMPS package was utilized to perform both the MD and the DPD simulations.

The DPD simulations are complex and require the matching of numerous fluid properties including the Schmidt's number, viscosity, and the dimensional compressibility of the real fluid. Presently, only the mean square displacement and the diffusion coefficient, a dynamic fluid transport properties, are compared, as the primary purpose of this section is to show the capability of the DPD method to simulate the fluid transport for the longer length and time scales, which is challenging with the traditional all-atom MD simulation technique. A rigorous analysis is required for the detailed study.

For the DPD simulations, the method described by (Ghoufi and Malfreyt 2011) is used. Three water molecules are combined to form a water bead, resulting in about 333 water beads. The particle mass, the system temperature, and the interaction range are taken as units of mass, temperature, and length respectively. An iterative approach is used to calibrate the DPD (particle interaction) parameters. The repulsive parameter (a_{ij}), the interatomic potential cut-off distance, and the viscosity coefficient (Υ) are optimized. Initially, the repulsion parameters of water and water-quartz were taken as $a = 25.0$ with the cut-off distance of 1.0 and optimized further during the calibration process.

Figures 6.18 and 6.19 show the graphical representation of the all-atom and the DPD simulation of water confined in quartz nanopore. Further, Figures 6.20 and 6.21 depicts the mean square displacement of water molecules obtained with the all-atom MD simulation and the DPD simulation. A diffusion coefficient of water, 2.15 x 10^{-8} m^2/s, is extracted from Figure 6.20 and converted into an equivalent DPD diffusion coefficient, 0.068 (in DPD units), using the relation provided by Ghoufi and Malfrey (2011). The DPD simulations performed with various possible combinations of the repulsive parameter, the cut-off distance, and the viscosity coefficient, and corresponding mean square displacement and diffusion coefficient are determined and shown in Figures 6.21 and 6.22. It was observed that the combination of $a = 25$, $r_c = 0.08$, and $Y = 0.25$ predicted the diffusion coefficient more closely to the value predicted by all-atom simulations. As expected, the DPD simulations were significantly faster than the all-atom MD simulations and able to simulate the fluid flow for the longer length and time scales.

To summarize the present chapter, a pore-scale dynamics of the water-methane system is simulated in the nanometer and subnanometer pores found in a kerogen matrix as a function of the system temperature and the external driving force to liquid molecules. The mean square displacement, the effective diffusion coefficients, and the number densities were determined. The results show that the realistic pore structures are not perfect. High external driving forces applied to water molecules are necessary to overcome the fluid-pore surface interactions and to enhance the mobility of methane. Further, the diffusion coefficient increases with increases in the pore diameter and the system temperatures, but the variation is not linear. The fluid molecule shows the asymmetric number density due to the underlying pore surface structure, the distribution of the water

molecules in the initial configuration, and the possible affinity of the molecules toward specific function groups from kerogen.

Pore diameter = 0.8 nm

a)

Pore diameter = 5 nm

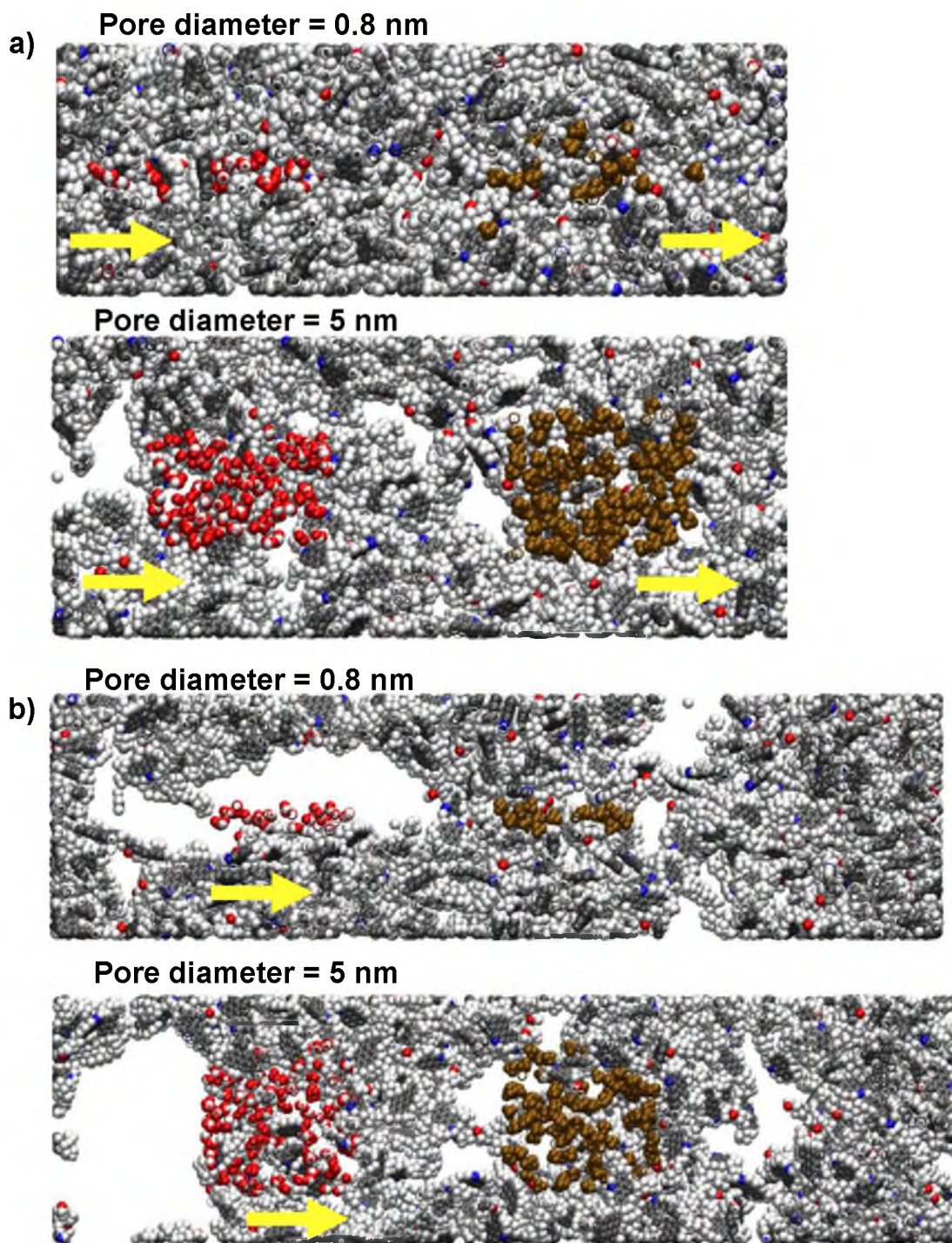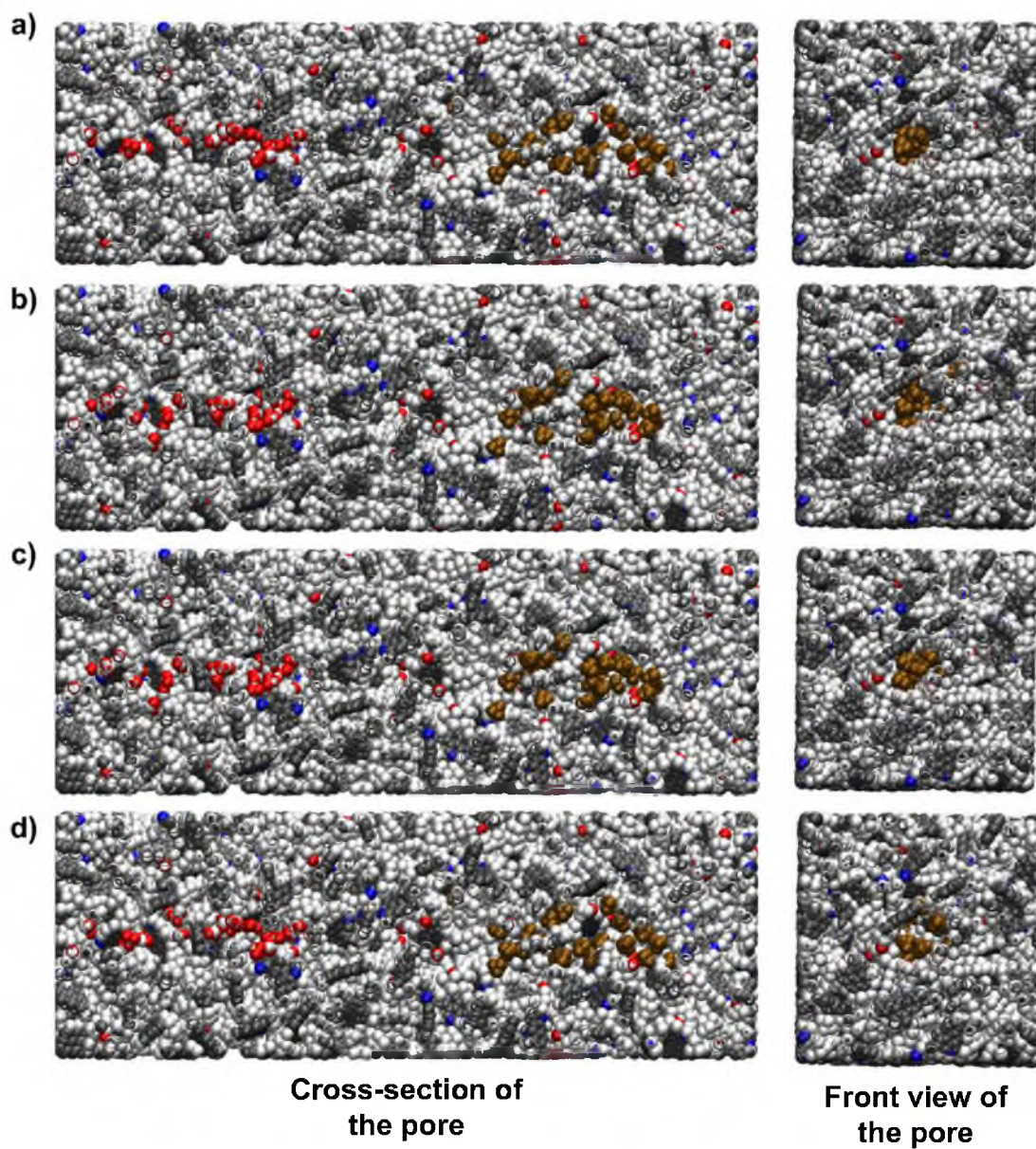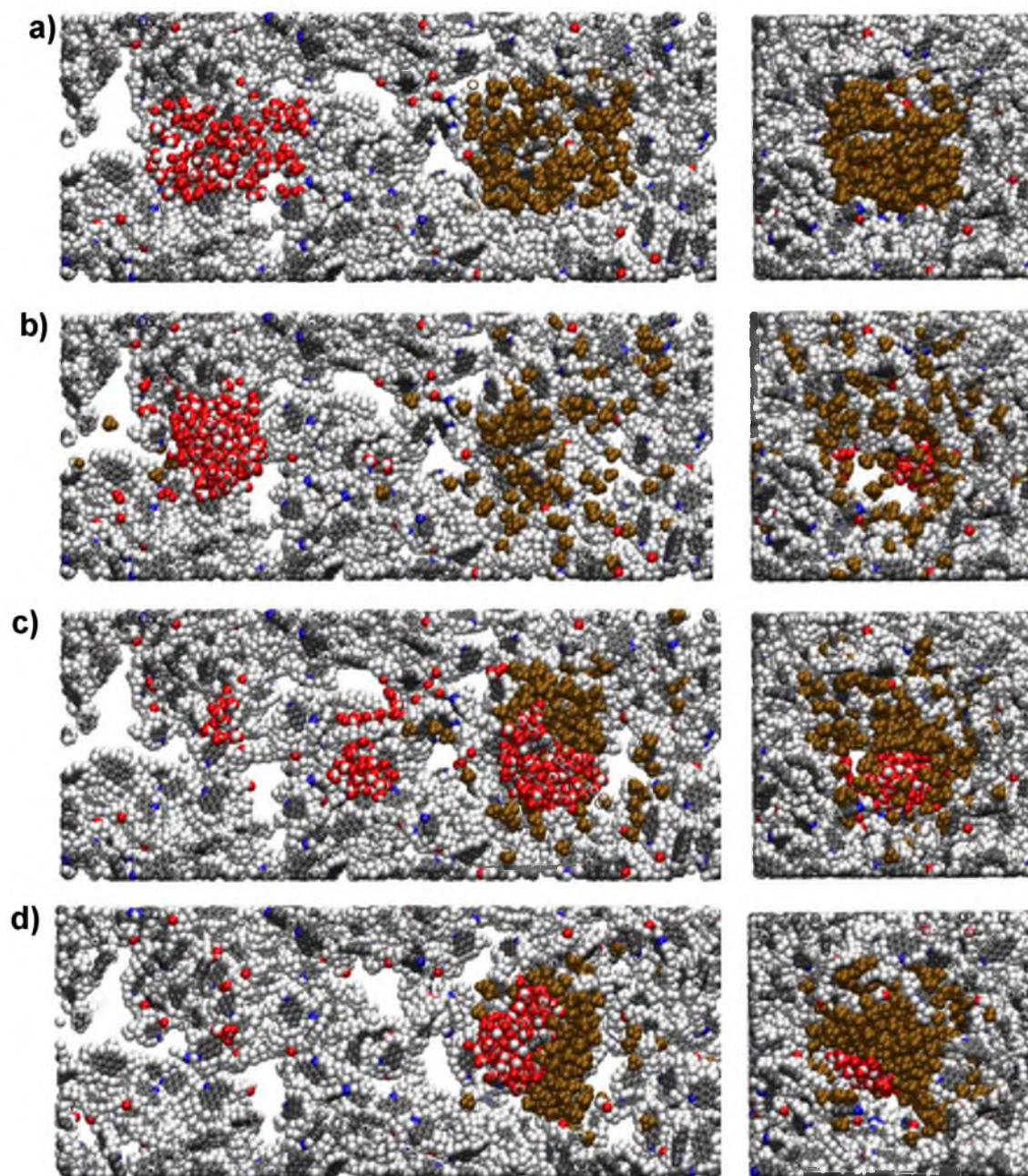**Pore diameter = 0.8 nm**

b)

Pore diameter = 5 nm

**FIGURE 6.1 Initial molecular configuration of a) open pores and b) closed pores**

FIGURE 6.2 a) Initial molecular configuration, and final molecular configuration of 0.8-nm pore at applied force of b) 0 Kcal/mol-Å, c) 0.05 Kcal/mol-Å, and d) 0.1 Kcal/mol-Å to water molecules
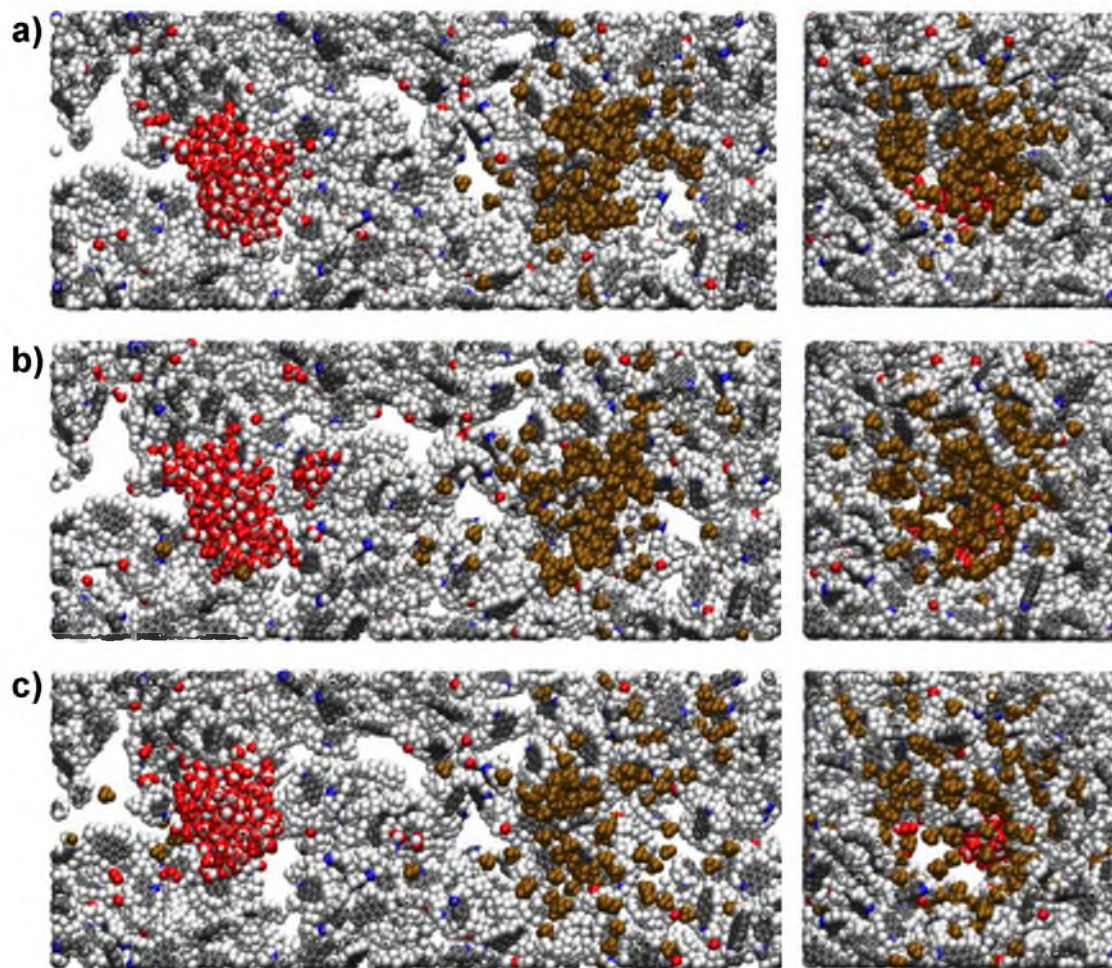
FIGURE 6.3 a) Initial molecular configuration, and final molecular configuration of 5-nm pore at applied force of b) 0 Kcal/mol-Å, c) 0.05 Kcal/mol-Å, and d) 0.1 Kcal/mol-Å to water molecules
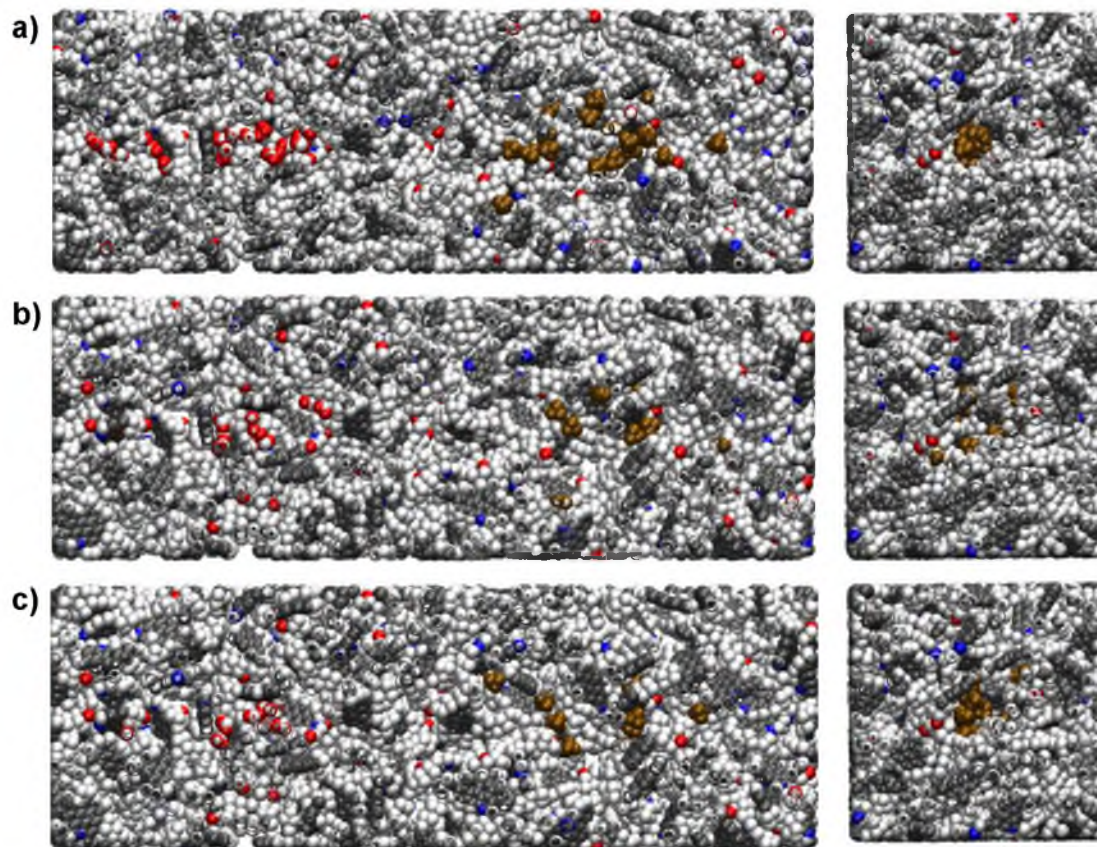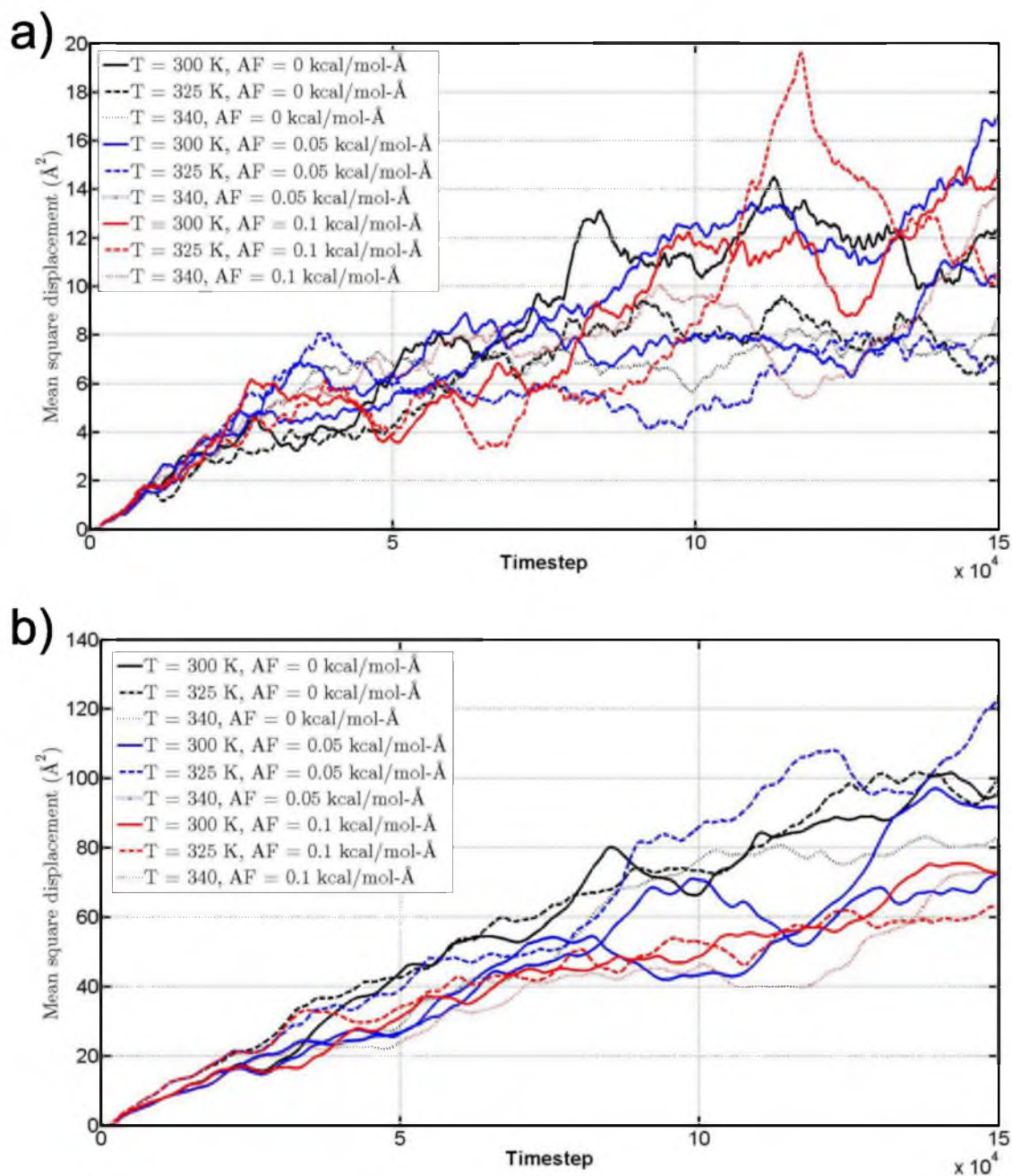
FIGURE 6.4 The impact of the system temperature on the water and methane behavior in 0.8-nm open pore at the temperature of a) 300 K, b) 325 K, and c) 340 K
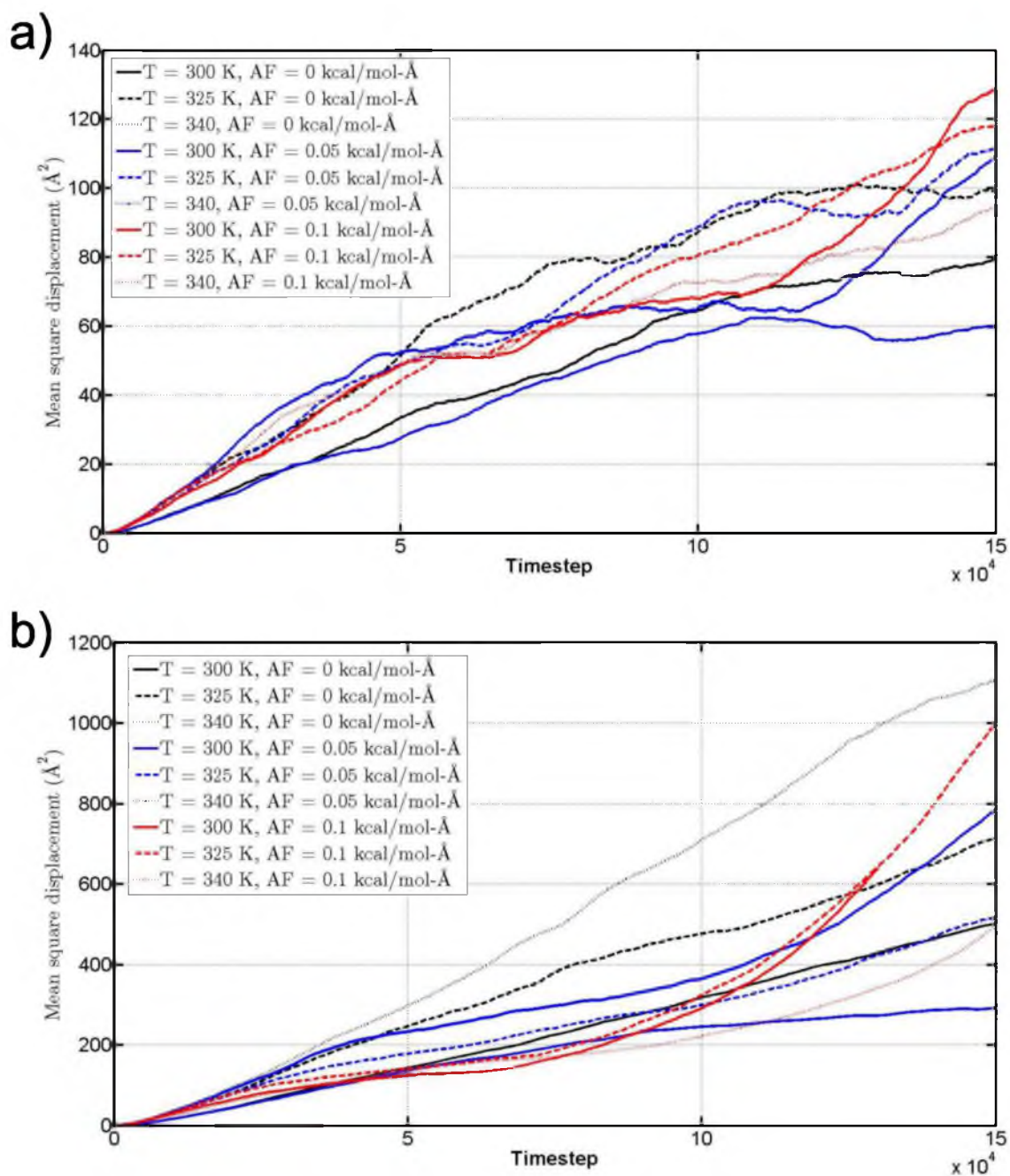
FIGURE 6.5 The impact of the system temperature on the water and methane behavior in 5-nm open pore at the temperature of a) 300 K, b) 325 K, and c) 340 K
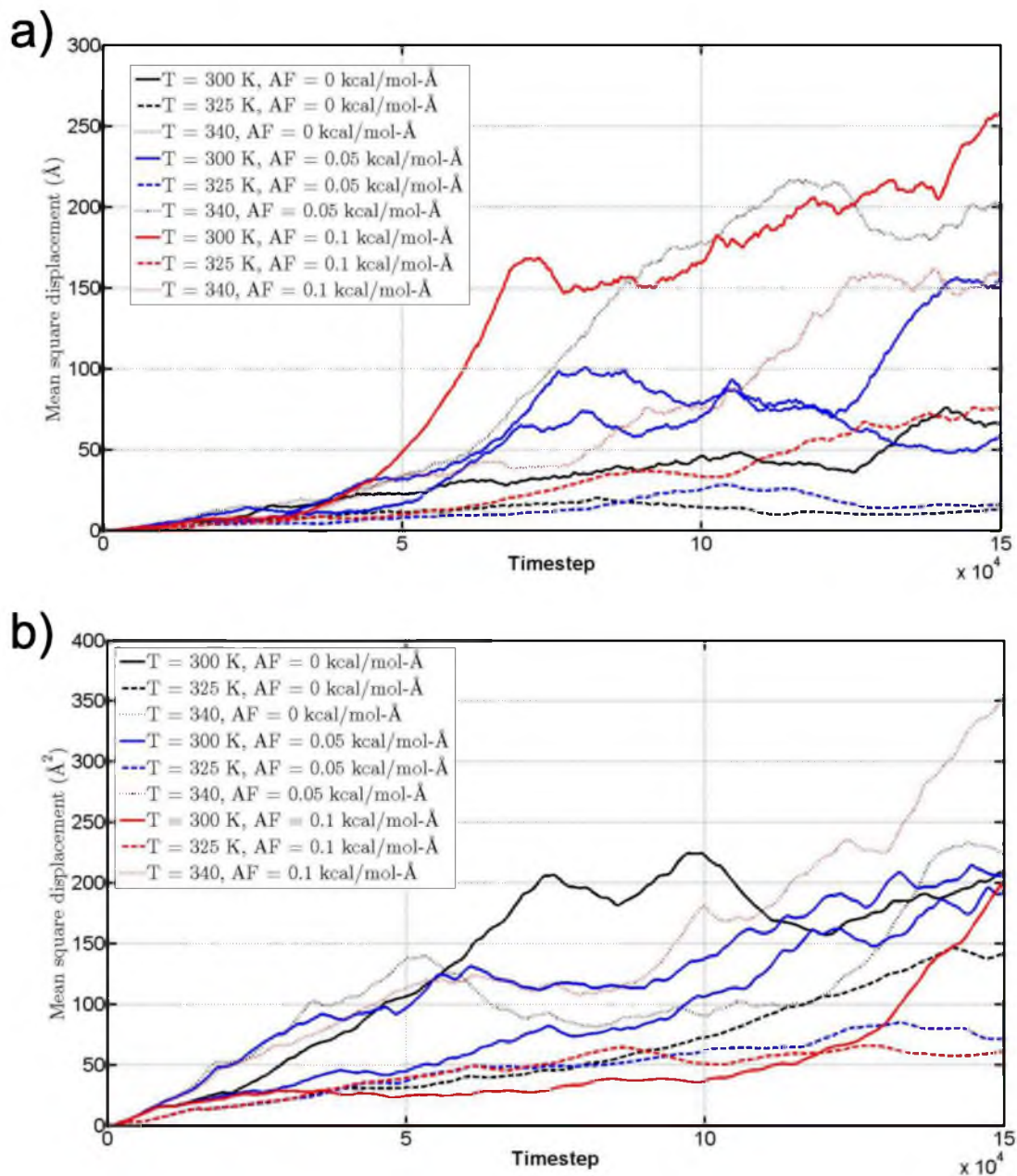
FIGURE 6.6 Mean square displacements of a) water and b) methane in 0.8-nm diameter open kerogen pore at various forces applied to water molecules and at different system temperatures

FIGURE 6.7 Mean square displacements of a) water and b) methane in 5-nm diameter open kerogen pore at various forces applied to water molecules and at different system temperatures
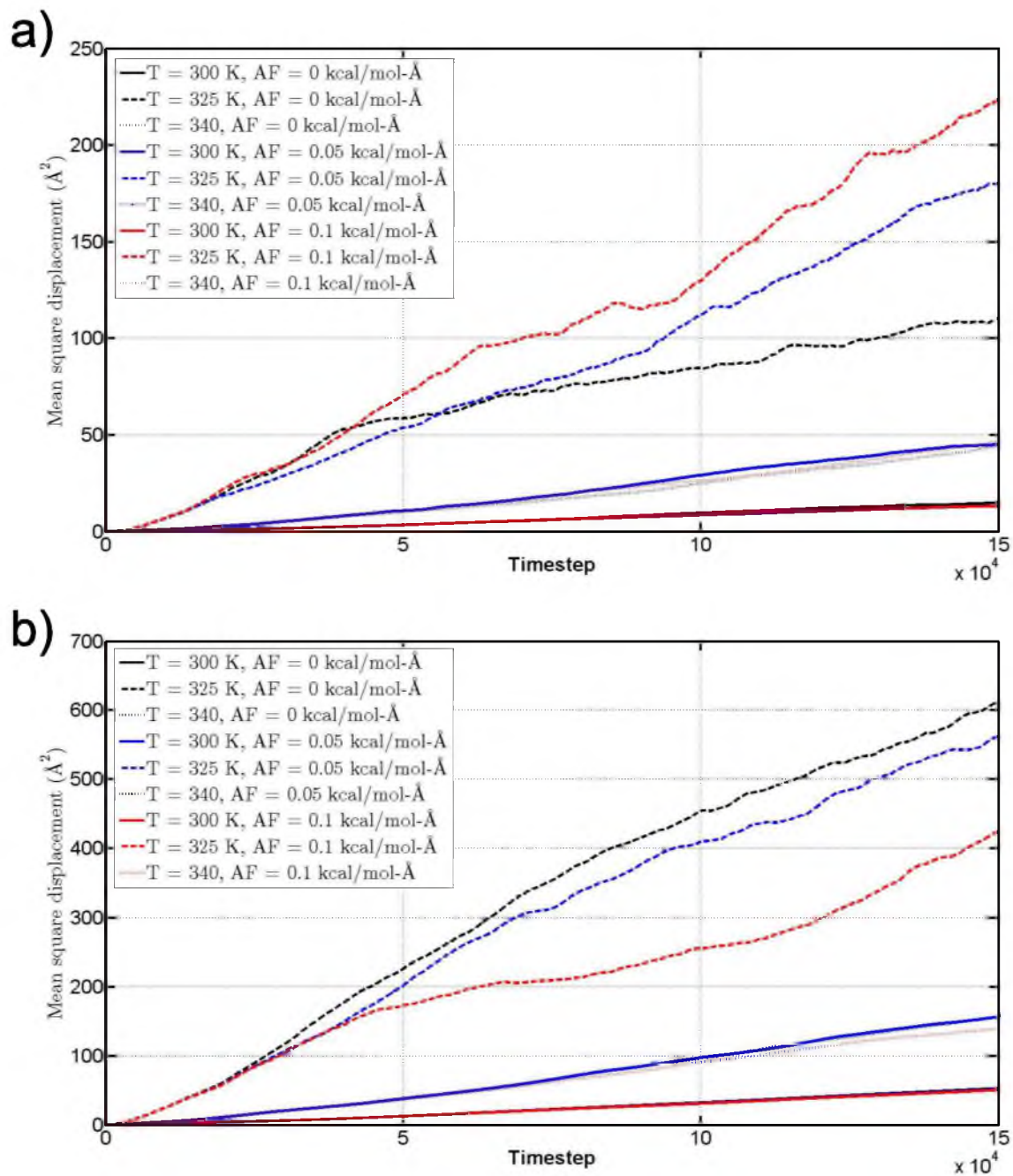
FIGURE 6.8 Mean square displacements of a) water and b) methane in 0.8-nm diameter closed kerogen pore at various forces applied to water molecules and at different system temperatures

FIGURE 6.9 Mean square displacements of a) water and b) methane in 5-nm diameter closed kerogen pore at various forces applied to water molecules and at different system temperatures
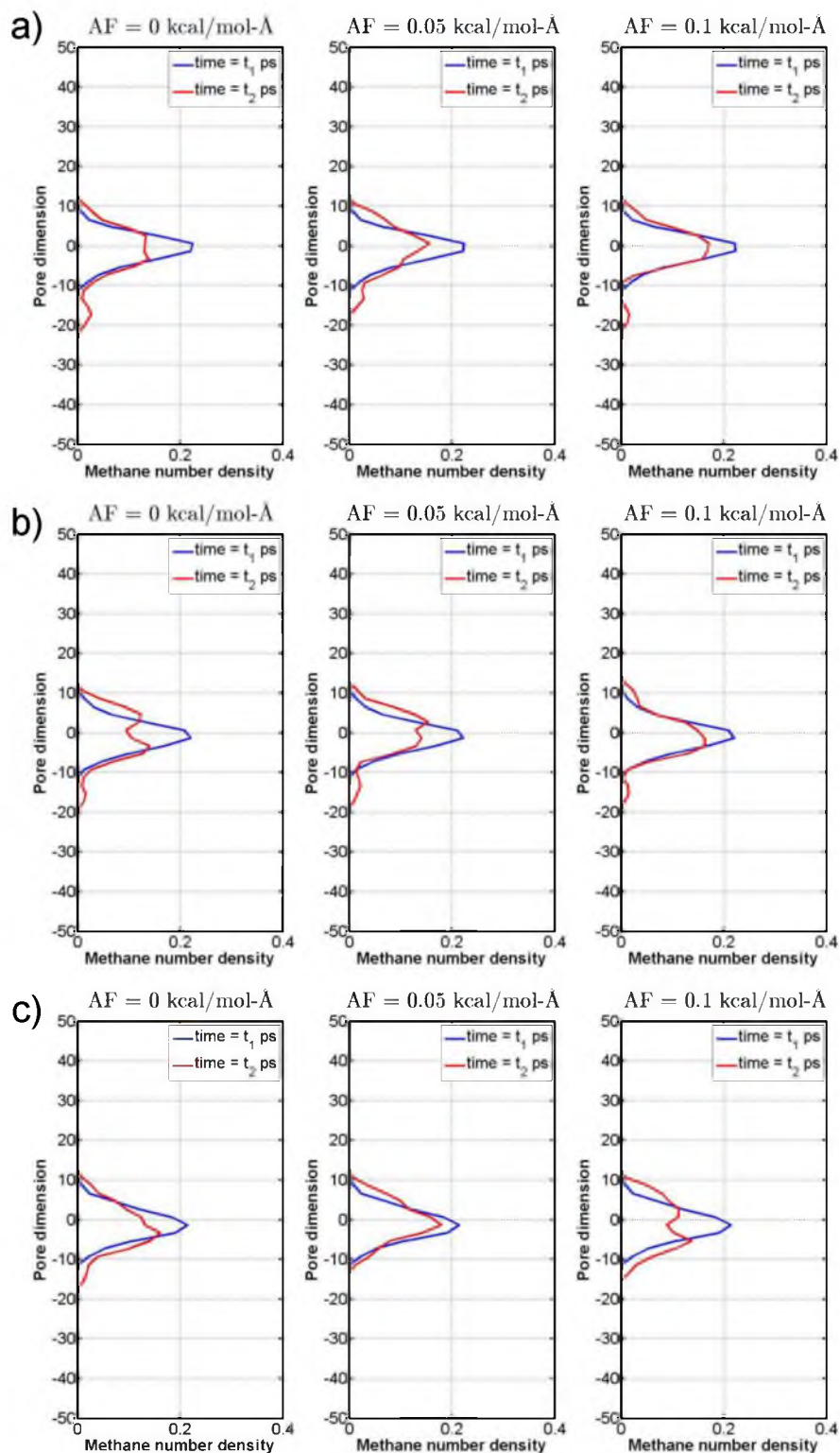
FIGURE 6.10 The methane number density in 0.8-nm diameter open pore for various forces applied to water molecules at temperature of a) 300 K, b) 325 K, and c) 340 K (meaning of "pore dimension" axis label explained on p. 50)
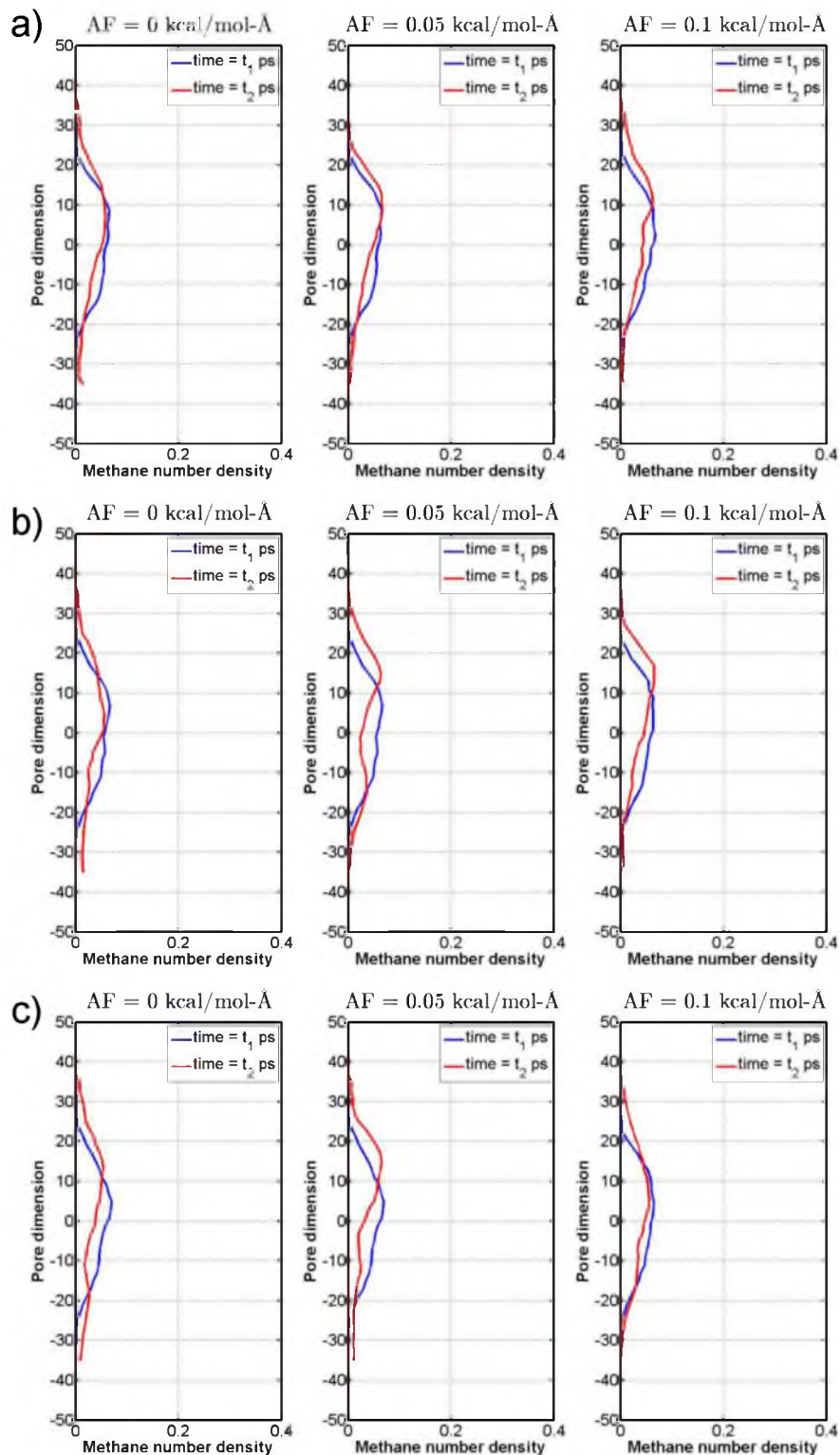
FIGURE 6.11 The methane number density in 5-nm diameter open pore for various forces applied to water molecules at temperature of a) 300 K, b) 325 K, and c) 340 K

FIGURE 6.12 The methane number density in 0.8-nm diameter closed pore for various forces applied to water molecules at temperature of a) 300 K, b) 325 K, and c) 340 K

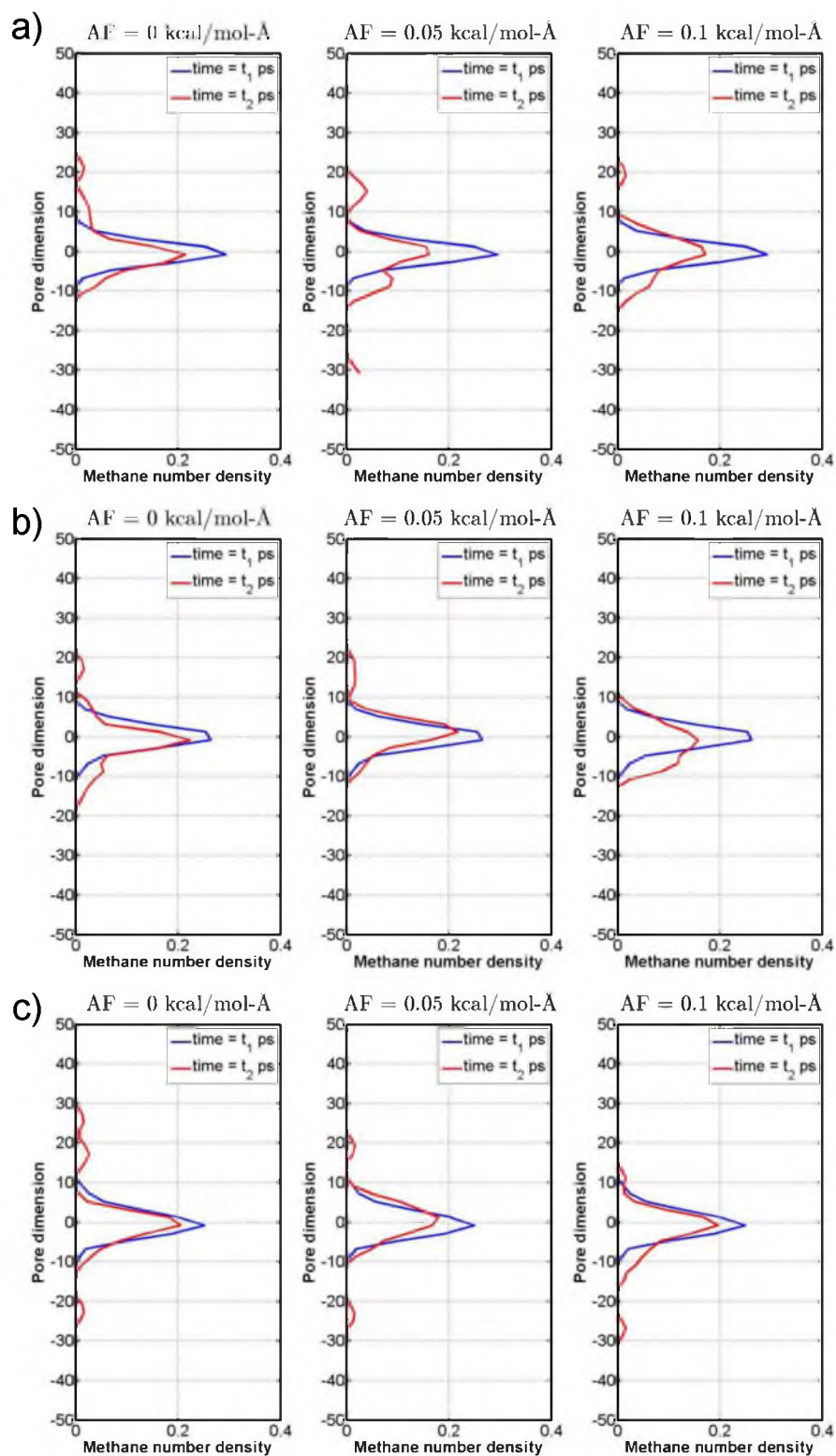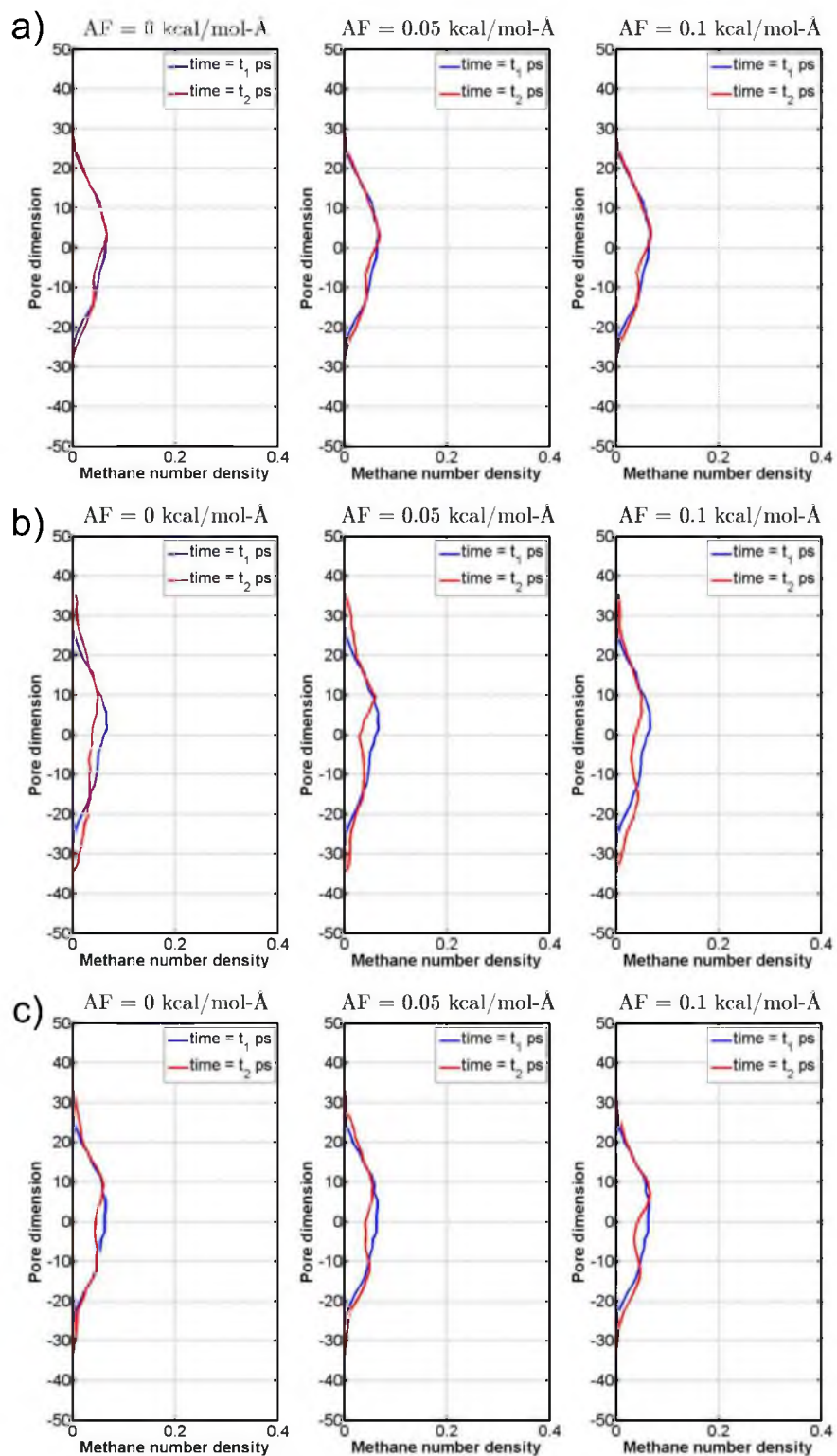**FIGURE 6.13 The methane number density in 5-nm diameter closed pore for various forces applied to water molecules at temperature of a) 300 K, b) 325 K, and c) 340 K**
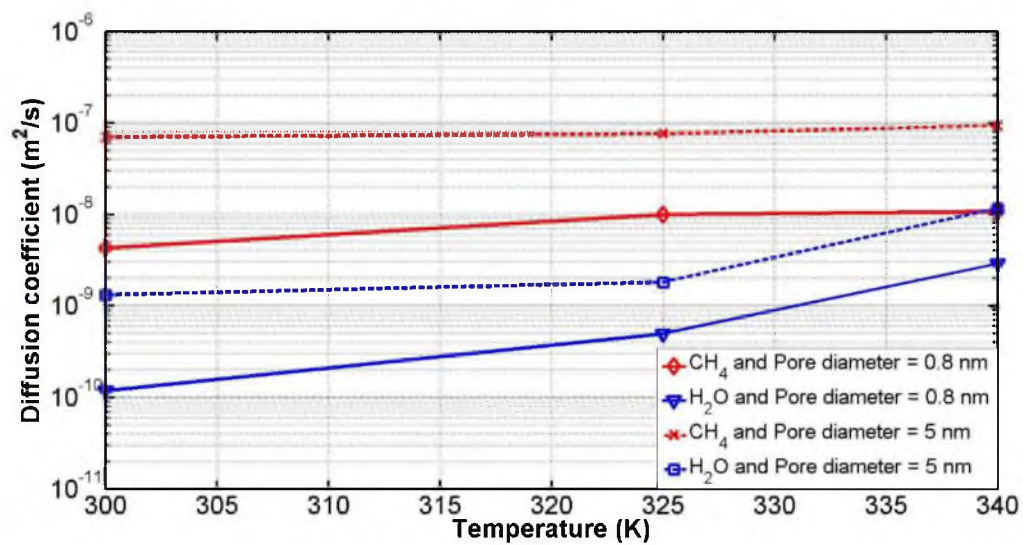
FIGURE 6.14 The water and methane effective diffusion coefficient in open pores at 0 Kcal/mol-Å force applied to water molecules and at temperature of a) 300 K, b) 325 K, and c) 340 K
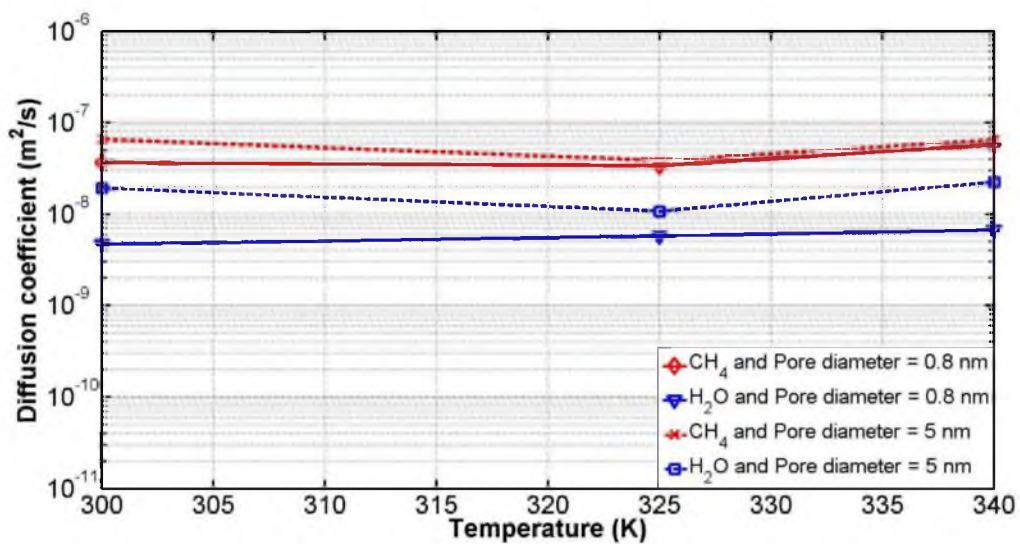
FIGURE 6.15 The water and methane effective diffusion coefficient in closed pores at 0 Kcal/mol-Å force applied to water molecules and at temperature of a) 300 K, b) 325 K, and c) 340 K
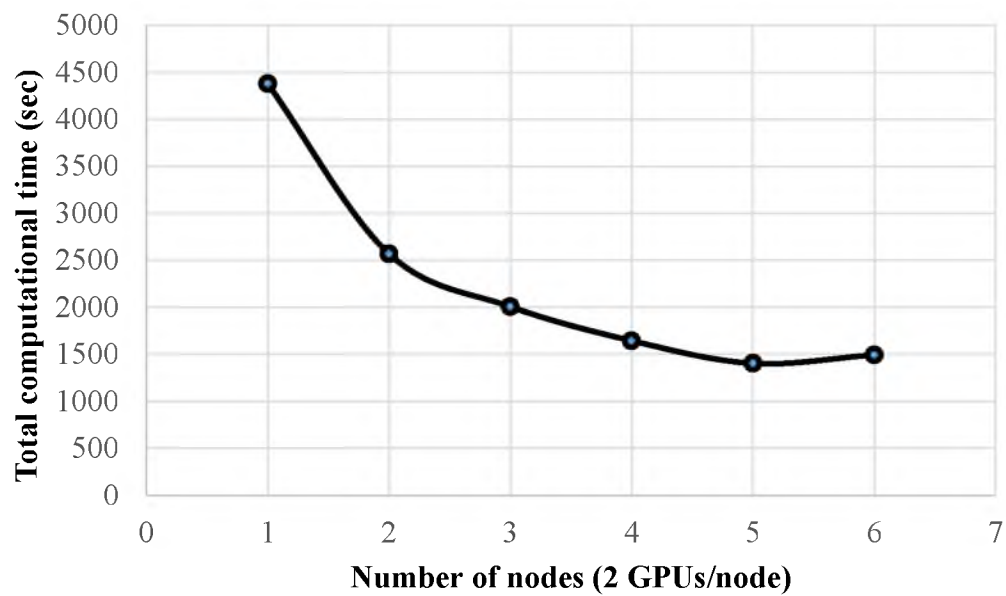
FIGURE 6.16 Comparison of the total computational time
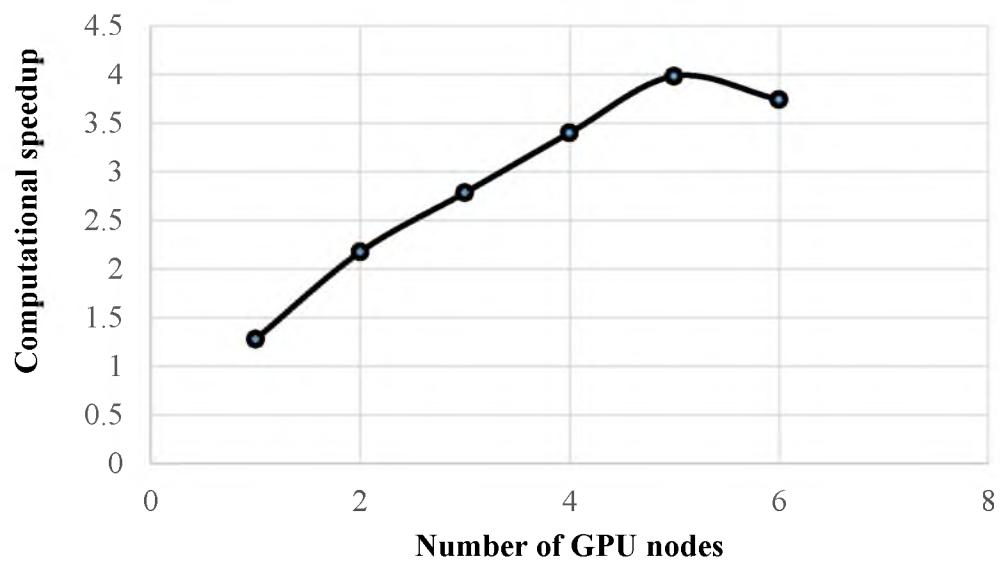
FIGURE 6.17 Computational speed up with GPUs
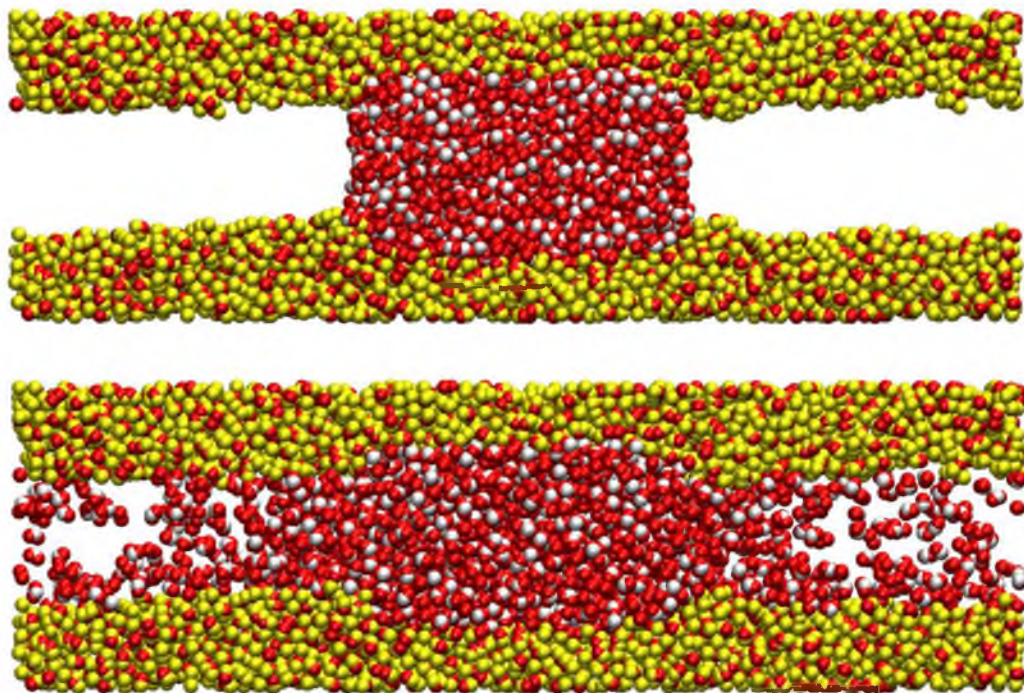
FIGURE 6.18 All-atom MD simulation of water confined in a quartz nanopore showing initial system configuration (top) and the final system configuration (bottom)
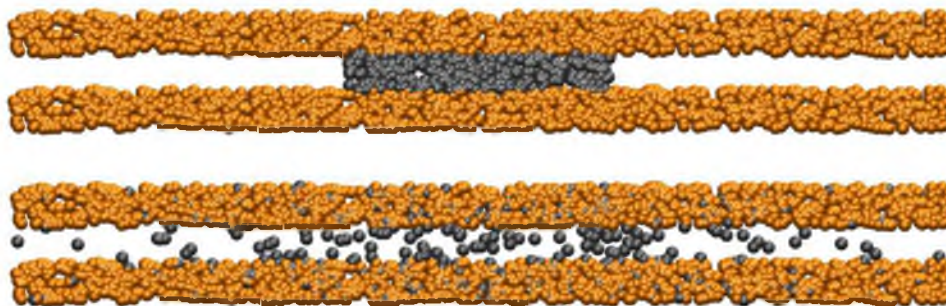
FIGURE 6.19 DPD simulation of water (gray color) confined in a quartz (orange color) nanopore showing initial system configuration (top) and the final system configuration (bottom)
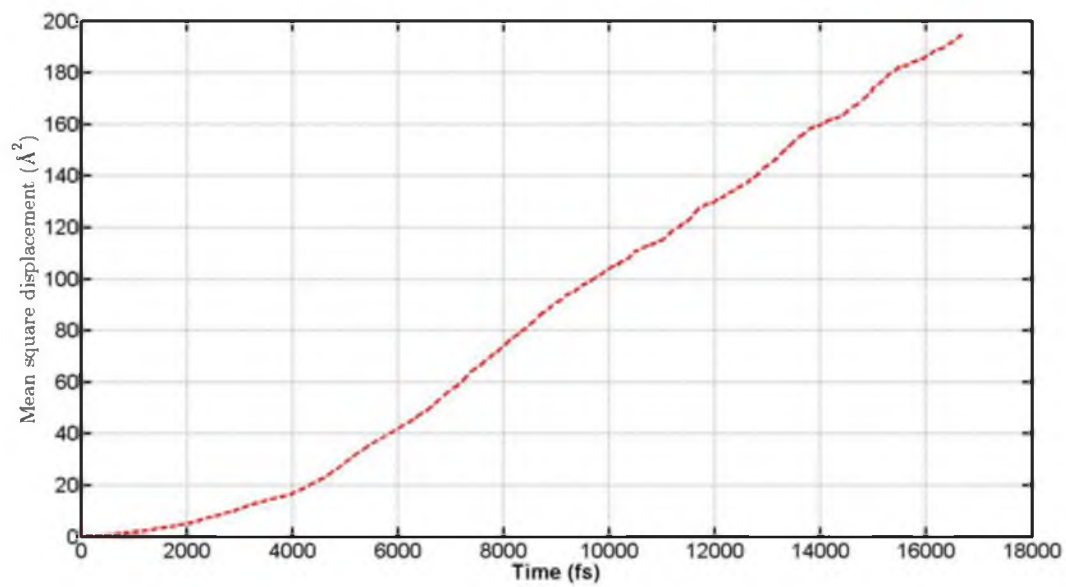
FIGURE 6.20 Mean square displacement of water confined in a quartz nanopore obtained with the all-atom MD simulation
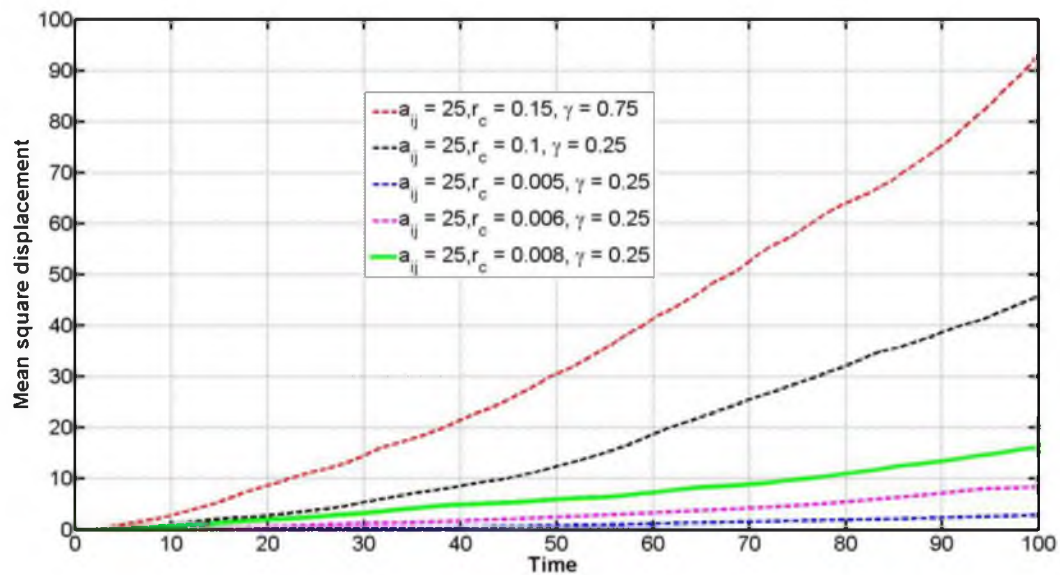
FIGURE 6.21 Mean square displacement of water (in DPD units) confined in a quartz nanopore obtained with the DPD simulation
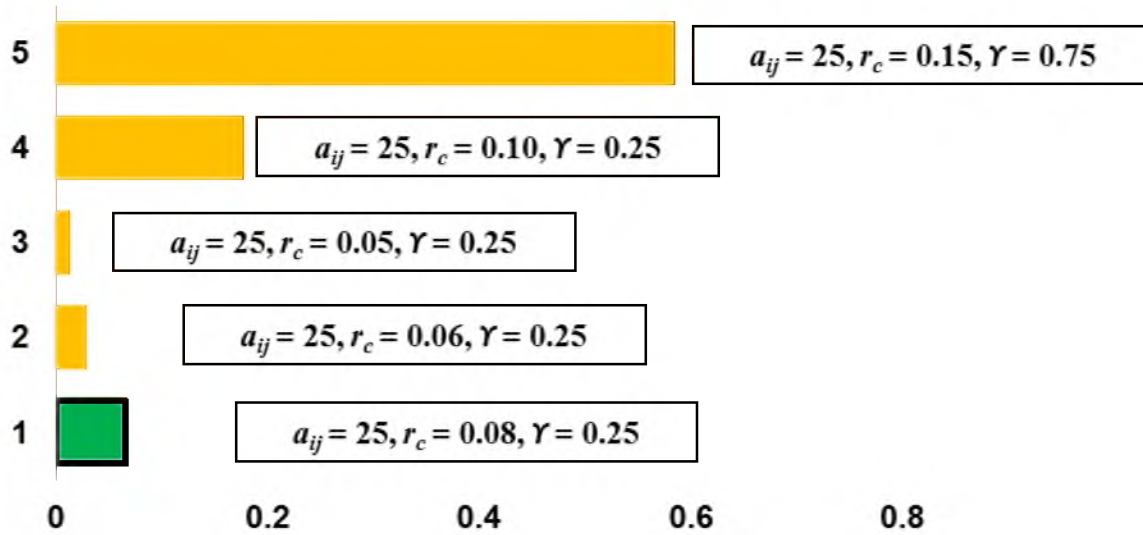
FIGURE 6.22 Calibration of DPD parameters to evaluate the diffusion coefficient; the y-axis represents the test run number whereas the x-axis represents the diffusion coefficient in DPD units

TABLE 6.1 Number of kerogens, water, and methane molecules used in the simulation

Flow	Diameter (nm)	Number of kerogen molecules	Number of water molecules	Number of methane molecules
Open pore	0.8	60	25	25
	5	60	250	250
Closed pore	0.8	100	25	25
	5	100	250	250

TABLE 6.2 Summary of initial and final simulation times

Pore configuration	Pore diameter (nm)	Temperature (K)	Initial (t_1) and final (t_2) simulation time (fs)
Open pore	0.8	300	$t_1 = 0$, $t_2 = 7370$
		325	$t_1 = 0$, $t_2 = 7370$
		340	$t_1 = 0$, $t_2 = 5965$
	5	300	$t_1 = 0$, $t_2 = 9563$
		325	$t_1 = 0$, $t_2 = 13822$
		340	$t_1 = 0$, $t_2 = 14898$
Closed pore	0.8	300	$t_1 = 0$, $t_2 = 14624$
		325	$t_1 = 0$, $t_2 = 7000$
		340	$t_1 = 0$, $t_2 = 14108$
	5	300	$t_1 = 0$, $t_2 = 1507$
		325	$t_1 = 0$, $t_2 = 14196$
		340	$t_1 = 0$, $t_2 = 3376$

TABLE 6.3 Diffusion coefficients in a 0.8-nm open pore

	Methane			Water		
	300 K	325 K	340 K	300 K	325 K	340 K
Diffusion coefficient (10^{-9}, m^2/s)	4.28	10	10.8	0.118	0.497	2.89
Standard deviation	2.61	2.16	3.05	0.30	0.43	0.74

TABLE 6.4 Diffusion coefficients in a 5-nm open pore

	Methane			Water		
	300 K	325 K	340 K	300 K	325 K	340 K
Diffusion coefficient (10^{-9}, m^2/s)	70.1	76.7	94.0	1.32	1.82	11.6
Standard deviation	1.68	2.66	2.71	0.11	0.15	0.35

TABLE 6.5 Diffusion coefficients in a 0.8-nm closed pore

	Methane			Water		
	300 K	325 K	340 K	300 K	325 K	340 K
Diffusion coefficient (10^{-9}, m^2/s)	36.3	33.8	57.1	4.67	5.78	6.70
Standard deviation	2.24	1.43	2.97	0.36	0.33	0.38

TABLE 6.6 Diffusion coefficient in a 5-nm closed pore

	Methane			Water		
	300 K	325 K	340 K	300 K	325 K	340 K
Diffusion coefficient (10^{-9}, m^2/s)	66	38.8	65.3	19.2	10.8	22.4
Standard deviation	1.64	3.08	2.60	0.48	0.93	0.90

CHAPTER 7

CONCLUSION

Motivated by the challenge of the inadequate understanding of the pore-scale multiphase fluid transport, which affects the hydrocarbon recovery rates and economic development of shale reservoirs, a molecular dynamics simulation-based framework is used to model, simulate, and characterize the pore-scale multiphase fluid transport in nanometer and subnanometer pores found in organic and inorganic shale matrices. Besides, various aspects of shale reservoirs such as subnanometer scale features in kerogen were uncovered while fulfilling the primary objective of the present research.

First, it is found that the pores found in organic and inorganic matrices deviates from the ideal cylindrical shape and have more irregular size and shapes as a consequence of the atomic arrangement of the underlying functional groups, which occurred during the geo-thermo-chemical transformation of organic and inorganic matrices.

Next, it is observed that the general-purpose DREIDING force provides a better alternative among the simple force fields and the tailored force fields to simulate the complex kerogen structure irrespective of the thermal maturity, the total organic content, and the elemental composition of the kerogen. Although the DREIDING force field underpredicts the kerogen densities when compared with the experimental and simulation studies from the literature, it provides a better approximation of the structural (pair distribution function) and physical properties (density) of kerogen — when there is no or

very little experimental data available.

Also, the structural characterization analysis of kerogen matrix showed the existence of significant numbers of the subnanometer size pores. The subnanometer size pores are one of the crucial factors that determine the reservoir porosity (reservoir quality) and may act as a nano-reservoir that holds a substantial amount of the displacement fluid and the displaced hydrocarbons, thus affecting the overall recovery rates.

The comparative analysis of the multiphase fluid flow (water as an displacement fluid and methane as an displaced phase) in subnanometer and nanometer pores suggests that the characterization of methane transport mechanisms (adsorption, absorption, and diffusion) in subnanometer pores is challenging due to the comparable size of the methane molecule and subnanometer pore. As a result, a strong pore-surface interaction exists that results in a chaotic movements (chaotic mean square displacements) of water and methane molecules and frequent collisions of these molecules with the pore wall. On the other hand, the behavior of water and methane changes with an increase in the pore diameter, which is confirmed with the analysis of deterministic mean square displacement of the water and methane molecules.

Furthermore, it was observed that the migration of the displacement fluid (water) and the displaced hydrocarbons (methane) are negligible in the absence of the force applied to water molecules, which shows the typical characteristic of shale reservoirs. Subsequently, a noticeable displacement of water molecules is observed with increases in the force applied to water molecules; thus showing that there exists a threshold force that needs to overcome the strong pore surface-fluid interactions, and to have noticeable displacements of injected reservoir fluid. However, the force applied to water molecules

that expedite the recovery process are high and may be beyond the practical limits, and also may change the phase of the fluids confined in nanopores.

Further, the water molecules near the pore surface tend to remain on the pore surface even under the application of a very high force, thus suggesting the possible water retention mechanism in the shale reservoirs. Also, the methane number density exhibits a preferential distribution of methane molecules in kerogen nanopores.

Finally, the dissipative particle dynamics (DPD) simulation approach along with the graphics processing units (GPU) technique show the potential of molecular dynamics (MD) simulations to simulate a complex and slow evolving transport process in shale reservoirs for longer length and time scales. The results obtained with the current research are valuable for future research in many aspects and useful to

- build the more complex shale nanopore structures, and simulate and characterize the transport mechanism of a variety of injection fluids
- study the phase behavior of the hydrocarbons confined in the shale organic/inorganic matrices
- optimize current production practices, and potentially develop new production methods aimed towards enhancing the hydrocarbon recovery rates from shales reservoirs

In conclusion, the present research enables the development of molecular models of nanopores found in organic and inorganic matrices, the simulation of complex pore-scale fluid transport in matrices, and the extension of the capabilities of MD simulations to model a slow transport processes for longer length and time scales, which will enhance our predictive capability of hydrocarbon recovery from unconventional reservoirs.

REFERENCES

Abramoff, M.D., Magalhães, P.J., and Ram, S.J. 2004. Image processing with ImageJ. *Biophotonics Int.*, 11(7): 36-42.

Ahmad, M., and Haghighi, M. 2012. Mineralogy and Petrophysical Evaluation of Roseneath and Murteree Shale Formations, Cooper Basin, Australia Using QEMSCAN and CT Scanning. *SPE Asia Pacific Oil and Gas Conference and Exhibition*, Perth, Australia, October 22-24. Society of Petroleum Engineers.

Anderson, B.J., Tester, J.W., Borghi, G.P., and Trout, B.L. 2005. Properties of inhibitors of methane hydrate formation via molecular dynamics simulations. *J. Am. Chem. Soc.*, 127(50): 17852-17862.

Baron, R., de Vries, A.H., Hünenberger, P.H., and van Gunsteren, W.F. 2006. Comparison of atomic-level and coarse-grained models for liquid hydrocarbons from molecular dynamics configurational entropy estimates. *J. Phys. Chem. B*, 110(16): 8464-8473.

Behar, F., and Vandenbroucke, M. 1987. Chemical modelling of kerogens. *Org. Geochem.*, 11(1): 15-24.

Bernard, S., Horsfield, B., Schulz, H.-M., Schreiber, A., Wirth, R., Vu, T.T.A., Perssen, F., Könitzer, S., Volk, H., and Sherwood, N. 2010. Multi-scale detection of organic and inorganic signatures provides insights into gas shale properties and evolution. *Chem. Erde*, 70: 119-133.

Budd, P.M., McKeown, N.B., and Fritsch, D. 2005. Free volume and intrinsic microporosity in polymers. *J. Mater. Chem.*, 15(20): 1977-1986.

Carlson, G. 1992. Computer simulation of the molecular structure of bituminous coal. *Energy Fuels*, 6(6): 771-778.

Chalmers, G.R., Bustin, R.M., and Power, I.M. 2012. Characterization of gas shale pore systems by porosimetry, pycnometry, surface area, and field emission scanning electron microscopy/transmission electron microscopy image analyses: Examples from the Barnett, Woodford, Haynesville, Marcellus, and Doig units. *AAPG Bull.*, 96(6): 1099-1119.

Chareonsuppanimit, P., Mohammad, S.A., Robinson, R.L., and Gasem, K.A. 2012. High-

pressure adsorption of gases on shales: measurements and modeling. *Int. J. Coal Geol.*, 95: 34-46.

Chen, X., Cao, G., Han, A., Punyamurtula, V.K., Liu, L., Culligan, P.J., Kim, T., and Qiao,Y. 2008. Nanoscale fluid transport: size and rate effects. *Nano Lett.*, 8(9): 2988-2992.

Chun-Yang, Y., and Mohanad, E.-H. 2009. Simulation of liquid argon flow along a nanochannel: effect of applied force. *Chin. J. Chem. Eng.*, 17(5): 734-738.

Civan, F. 2010. A review of approaches for describing gas transfer through extremely tight porous media. *Porous Media and Its Applications Ifsn Science, Engineering, and Industry: 3rd International Conference*, Montecatini, Italy, June 20-25. Melville, New York, AIP Publishing, pp. 53-58.

Clarkson, C., Jensen, J., and Chipperfield, S. 2012. Unconventional gas reservoir evaluation: What do we have to consider? *J. Nat. Gas Sci. Eng.*, 8: 9-33.

Clarkson, C.R., Solano, N., Bustin, R., Bustin, A., Chalmers, G., He, L., Melnichenko, Y.B., Radliński, A., and Blach, T.P. 2013. Pore structure characterization of North American shale gas reservoirs using USANS/SANS, gas adsorption, and mercury intrusion. *Fuel*, 103: 606-616.

Collell, J., Galliero, G., Gouth, F., Montel, F., Pujol, M., Ungerer, P., and Yiannourakou, M. 2014. Molecular simulation and modelisation of methane/ethane mixtures adsorption onto a microporous molecular model of kerogen under typical reservoir conditions. *Microporous and Mesoporous Mater.*, 197: 194-203.

Curtis, M.E., Ambrose, R.J., Sondergeld, C.H., and Rai, C.S. 2011. Investigation of the relationship between organic porosity and thermal maturity in the Marcellus Shale. *North American Unconventional Gas Conference and Exhibition*, The Woodlands, Texas, June 14-16. Society of Petroleum Engineers.

Docherty, H., Galindo, A., Vega, C., and Sanz, E. 2006. A potential model for methane in water describing correctly the solubility of the gas and the properties of the methane hydrate. *J. Chem. Phys.*, 125(7): 074510.

Dow, W.G. 1977. Kerogen studies and geological interpretations. *J. Geochem. Explor.*, 7: 79-99.

Facelli, J.C.P., R. J., Pimienta, I. S., Badu, S., and Orendt, A. M. 2011. Atomistic Modeling of Oil Shale Kerogens and Asphaltenes along with Their Interactions with the Inorganic Mineral Matrix. University of Utah: Salt Lake City, UT.

Falk, K., Coasne, B., Pellenq, R., Ulm, F.J., and Bocquet, L. 2015. Subcontinuum mass transport of condensed hydrocarbons in nanoporous media. *Nat. Commun.*, 6.

Firincioglu, T., Ozkan, E., and Ozgen, C. 2012. Thermodynamics of multiphase flow in unconventional liquids-rich reservoirs. *SPE Annual Technical Conference and Exhibition*, San Antonio, October 8-10. Society of Petroleum Engineers.

Firouzi, M., and Wilcox, J. 2012. Molecular modeling of carbon dioxide transport and storage in porous carbon-based materials. *Microporous and Mesoporous Mater.*, 158: 195-203.

Gasteiger, J., and Marsili, M. 1980. Iterative partial equalization of orbital electronegativity—a rapid access to atomic charges. *Tetrahedron*, 36(22): 3219-3228.

Ghoufi, A., and Malfreyt, P. 2011. Mesoscale modeling of the water liquid-vapor interface: A surface tension calculation. *Phys. Rev. E*, 83(5): 051601.

Gohlke, H., and Thorpe, M. 2006. A natural coarse graining for simulating large biomolecular motion. *Biophys. J.*, 91(6): 2115-2120.

Groot, R.D., and Warren, P.B. 1997. Dissipative particle dynamics: Bridging the gap between atomistic and mesoscopic simulation. *J. Chem. Phys.*, 107(11): 4423.

Haile, J. 1993. Molecular dynamics simulation: Elementary methods. *Computers in Physics*, 7(6): 625-625.

Hanasaki, I., and Nakatani, A. 2006. Water flow through carbon nanotube junctions as molecular convergent nozzles. *Nanotechnol.*, 17(11): 2794.

Hao, L., and Cheng, P. 2010. Pore-scale simulations on relative permeabilities of porous media by lattice Boltzmann method. *Int. J. Heat Mass Transfer*, 53(9): 1908-1913.

Holditch, S., Perry, K., and Lee, J. 2007. Unconventional Gas Reservoirs—Tight Gas, Coal Seams, and Shales, *Working Document of the National Petroleum Council on Global Oil and Gas Study*. National Petroleum Council.

Hou, Q., Li, M., Zhou, Y., Cui, J., Cui, Z., and Wang, J. 2013. Molecular dynamics simulations with many-body potentials on multiple GPUs—The implementation, package and performance. *Comput. Phys. Commun.*, 184(9): 2091-2101.

Hu, H., Li, X., Fang, Z., Wei, N., and Li, Q. 2010. Small-molecule gas sorption and diffusion in coal: Molecular simulation. *Energy*, 35(7): 2939-2944.

Hu, Y., Devegowda, D., Striolo, A., Phan, A., Ho, T.A., Civan, F., and Sigal, R. 2015. The dynamics of hydraulic fracture water confined in nano-pores in shale reservoirs. *J. Unconvent. Oil Gas Resour.*, 9: 31-39.

Huang, C., Li, C., Choi, P.Y., Nandakumar, K., and Kostiuk, L.W. 2010. Effect of cut-off

distance used in molecular dynamics simulations on fluid properties. *Mol. Simul.*, 36(11): 856-864.

Huang, C., Nandakumar, K., Choi, P.Y., and Kostiuk, L.W. 2006. Molecular dynamics simulation of a pressure-driven liquid transport process in a cylindrical nanopore using two self-adjusting plates. *J. Chem. Phys.*, 124(23): 234701.

Hui, X., and Chao, L. 2012. Molecular dynamics simulations of gas flow in nanochannel with a Janus interface. *AIP Adv.*, 2(4): 042126.

Humphrey, W., Dalke, A., and Schulten, K. 1996. VMD: visual molecular dynamics. *J. Mol. Graphics*, 14(1): 33-38.

Izvekov, S., Violi, A., and Voth, G.A. 2005. Systematic coarse-graining of nanoparticle interactions in molecular dynamics simulation. *J. Phys. Chem. B*, 109(36): 17019-17024.

Janecek, J., and Netz, R.R. 2007. Interfacial water at hydrophobic and hydrophilic surfaces: Depletion versus adsorption. *Langmuir*, 23(16): 8417-8429.

Javadpour, F., Fisher, D., and Unsworth, M. 2007. Nanoscale gas flow in shale gas sediments. *J. Can. Pet. Technol.*, 46(10):55-61

Jiménez, A., Iglesias, M.J., Laggoun-Défarge, F. and Suarez-Ruiz, I. 1998. Study of physical and chemical properties of vitrinites. Inferences on depositional and coalification controls. *Chem. Geol.*, 150(3): 197-221.

Jusufi, A., DeVane, R.H., Shinoda, W., and Klein, M.L. 2011. Nanoscale carbon particles and the stability of lipid bilayers. *Soft Matter*, 7(3): 1139-1146.

King, George Everette. "Thirty years of gas shale fracturing: what have we learned?." In *SPE Annual Technical Conference and Exhibition*, Florence, Italy, September 19-22. Society of Petroleum Engineers, 2010.

Kuila, U. and Prasad, M. 2013. Specific surface area and pore-size distribution in clays and shales. *Geophys. Prospect.*, 61(2): 341-362.

Levine, B.G., LeBard, D.N., DeVane, R., Shinoda, W., Kohlmeyer, A., and Klein, M.L. 2011. Micellization studied by gpu-accelerated coarse-grained molecular dynamics. *J. Chem. Theory Comput.*, 7(12): 4135-4145.

Liu, M., Meakin, P., and Huang, H. 2007. Dissipative particle dynamics simulation of multiphase fluid flow in microchannels and microchannel networks. *Phys. Fluids*, 19(3): 033302.

Liu, X., Zhan, J.-H., Lai, D., Liu, X., Zhang, Z., and Xu, G. 2015. Initial Pyrolysis

Mechanism of Oil Shale Kerogen with Reactive Molecular Dynamics Simulation. *Energy Fuels*, 29 (5): 2987-2997.

Loucks, R.G., Reed, R.M., Ruppel, S.C., and Hammes, U. 2012. Spectrum of pore types and networks in mudrocks and a descriptive classification for matrix-related mudrock pores. *AAPG Bull.*, 96(6): 1071-1098.

Loucks, R.G., Reed, R.M., Ruppel, S.C., and Jarvie, D.M. 2009. Morphology, genesis, and distribution of nanometer-scale pores in siliceous mudstones of the Mississippian Barnett Shale. *J. Sediment. Res.*, 79(12): 848-861.

Ma, Y.Z., and Holditch, S. 2015. Unconventional Oil and Gas Resources Handbook: Evaluation and Development. Waltham, Massuchuates, *Elsevier Science*.

Mark, P., and Nilsson, L. 2001. Structure and dynamics of the TIP3P, SPC, and SPC/E water models at 298 K. *J. Phys. Chem. A*, 105(43): 9954-9960.

Markutsya, S., Devarajan, A., Baluyut, J.Y., Windus, T.L., Gordon, M.S., and Lamm, M.H. 2013. Evaluation of coarse-grained mapping schemes for polysaccharide chains in cellulose. *J. Chem. Phys.*, 138(21): 214108.

Mayo, S.L., Olafson, B.D., and Goddard, W.A. 1990. DREIDING: a generic force field for molecular simulations. *J. Phys. Chem.*, 94(26): 8897-8909.

McCaughan, J., Iglauer, S., and Bresme, F. 2013. Molecular dynamics simulation of water/CO 2-quartz interfacial properties: Application to subsurface gas injection. *Energy Procedia*, 37: 5387-5402.

McKeown, N.B. and Budd, P.M. 2010. Exploitation of intrinsic microporosity in polymer-based materials. *Macromolecules*, 43(12): 5163-5176.

Morse, H.S. 2014. Practical Parallel Computing. Cambridge, *Academic Press Proffesional*.

Nakamura, K., Murata, S., and Nomura, M. 1993. CAMD study of coal model molecules. 1. Estimation of physical density of coal model molecules. *Energy Fuels*, 7(3): 347-350.

Nelson, P.H. 2009. Pore-throat sizes in sandstones, tight sandstones, and shales. *AAPG Bull.*, 93(3): 329-340.

Okiongbo, K.S., Aplin, A.C., and Larter, S.R. 2005. Changes in type II kerogen density as a function of maturity: Evidence from the Kimmeridge Clay Formation. *Energy Fuels*, 19(6): 2495-2499.

Orendt, A.M., Pimienta, I.S., Badu, S.R., Solum, M.S., Pugmire, R.J., Facelli, J.C., Locke, D.R., Chapman, K.W., Chupas, P.J., and Winans, R.E. 2013. Three-dimensional

structure of the Siskin Green River oil shale kerogen model: A comparison between calculated and observed properties. *Energy Fuels*, 27(2): 702-710.

Petkov, V., Ren, Y., Kabekkodu, S., and Murphy, D. 2013. Atomic pair distribution functions analysis of disordered low-Z materials. *Phys. Chem. Chem. Phys.*, 15(22): 8544-8554.

Pettersen, E.F., Goddard, T.D., Huang, C.C., Couch, G.S., Greenblatt, D.M., Meng, E.C., and Ferrin, T.E. 2004. UCSF Chimera—a visualization system for exploratory research and analysis. *J. Comput. Chem.*, 25(13): 1605-1612.

Plimpton, S. 1995. Fast parallel algorithms for short-range molecular dynamics. *J. Comput. Phys.*, 117(1): 1-19.

Pohl, P.I., and Heffelfinger, G.S. 1999. Massively parallel molecular dynamics simulation of gas permeation across porous silica membranes. *J. Membr. Sci.*, 155(1): 1-7.

Reed, S.K., and Westacott, R.E. 2008. The interface between water and a hydrophobic gas. *Phys. Chem. Chem. Phys.*, 10(31): 4614-4622.

Riniker, S., and van Gunsteren, W.F. 2011. A simple, efficient polarizable coarse-grained water model for molecular dynamics simulations. *J. Chem. Phys.*, 134(8): 084110.

Roychaudhuri, B., Tsotsis, T.T., and Jessen, K. 2013. An experimental investigation of spontaneous imbibition in gas shales. *J. Pet. Sci. Eng.*, 111: 87-97.

Siskin, M., Scouten, C., Rose, K., Aczel, T., Colgrove, S., and Pabst Jr, R. 1995. Detailed structural characterization of the organic material in Rundle Ramsay Crossing and Green River oil shales, Composition, geochemistry and conversion of oil shales. *Springer*, pp. 143-158.

Sokhan, V.P., Nicholson, D., and Quirke, N. 2002. Fluid flow in nanopores: Accurate boundary conditions for carbon nanotubes. *J. Chem. Phys.*, 117(18): 8531-8539.

Stankiewicz, B.A., Kruge, M.A., Crelling, J.C., and Salmon, G.L. 1994. Density Gradient Centrifugation: Application to the Separation of Macerals of Type I, II, and III Sedimentary Organic Matter. *Energy Fuels*, 8(6): 1513-1521.

Stukan, M.R., Ligneul, P., and Boek, E.S. 2012. Molecular dynamics simulation of spontaneous imbibition in nanopores and recovery of asphaltenic crude oils using surfactants for EOR applications. *Oil Gas Sci. Tech.–Revue d'IFP Energies nouvelles*, 67(5): 737-742.

Takahashi, S., and Kovscek, A.R. 2010. Spontaneous countercurrent imbibition and forced displacement characteristics of low-permeability, siliceous shale rocks. *J. Pet. Sci. Eng.*, 71(1): 47-55.

Teklu, T.W., Alharthy, N., Kazemi, H., Yin, X., Graves, R.M., and AlSumaiti, A.M. 2014. Phase behavior and minimum miscibility pressure in nanopores. *SPE Reservoir Eval. Eng.*, 17(03): 396-403.

Ungerer, P., Collell, J., and Yiannourakou, M. 2014. Molecular modeling of the volumetric and thermodynamic properties of kerogen: influence of organic type and maturity. *Energy Fuels*, 29(1): 91-105.

Ungerer, P., Collell, J., and Yiannourakou, M. 2015. Molecular Modeling of the Volumetric and Thermodynamic Properties of Kerogen: Influence of Organic Type and Maturity. *Energy Fuels*, 29(1): 91-105.

Ungerer, P., Tavitian, B., and Boutin, A. 2005. Applications of Molecular Simulation in the Oil and Gas Industry: Monte Carlo Methods. Editions Technip.

Van Krevelen, D. 1984. Organic geochemistry—old and new. *Org. Geochem.*, 6: 1-10.

Wang, F.P., and Reed, R.M. 2009. Pore networks and fluid flow in gas shales. *SPE Annual Technical Conference and Exhibition*, New Orleans, Louisiana, October 4-7. Society of Petroleum Engineers.

Wang, J., Zhu, Y., Zhou, J., and Lu, X.-H. 2004. Diameter and helicity effects on static properties of water molecules confined in carbon nanotubes. *Phys. Chem. Chem. Phys.*, 6(4): 829-835.

Wolf, W. 2010. High-Performance Embedded Computing: Architectures, Applications, and Methodologies. Elsevier Science.

Wu, C., and Xu, W. 2006. Atomistic molecular modelling of crosslinked epoxy resin. *Polymer*, 47(16): 6004-6009.

Xu, B., Wang, B., Park, T., Qiao, Y., Zhou, Q., and Chen, X. 2012. Temperature dependence of fluid transport in nanopores. *J. Chem. Phys.*, 136(18): 184701.

Yan, B., Alfi, M., Wang, Y., and Killough, J.E. 2013. A new approach for the simulation of fluid flow in unconventional reservoirs through multiple permeability modeling. *SPE Annual Technical Conference and Exhibition*, New Orleans, Louisiana, September 30-October 2. Society of Petroleum Engineers.

Young, D. 2004. Computational Chemistry: A Practical Guide for Applying Techniques to Real World Problems. Wiley.

Zielkiewicz, J. 2005. Structural properties of water: Comparison of the SPC, SPCE, TIP4P, and TIP5P models of water. *J. Chem. Phys.*, 123(10): 104501.